THE GROWTH OF INTERMETALLIC PHASES ON IRON GALVANIZED IN AN ALUMINUM-BEARING ZINC BATH AT 450°C

THE GROWTH OF INTERMETALLIC PHASES ON IRON GALVANIZED IN AN ALUMINUM-BEARING ZINC BATH AT 450°C

by

M. Úředníček, Dipl. Ing.

A Thesis

Submitted to the School of Graduate Studies

in Partial Fulfilment of the Requirements

for the Degree

Master of Engineering

McMaster University

September, 1972

MASTER OF ENGINEERING
(Metallurgy and Materials Science)

McMASTER UNIVERSITY
Hamilton, Ontario

TITLE: The Growth of Intermetallic Phases on Iron Galvanized in an Aluminum-Bearing Zinc Bath at 450°C.

AUTHOR: Miroslav Úředníček (Dipl. Ing., Technical University. Liberec, Czechoslovakia)

SUPERVISOR: Dr. J. S. Kirkaldy

NUMBER OF PAGES: xiii, 168

ABSTRACT

This thesis is concerned with determination of the nature and growth characteristics of the intermediate phases formed on iron galvanized in Al-bearing Zn at 450°C. Long time equilibrium experiments have been carried out to explain the nature of intermetallic phases and their equilibria in the system Fe-Zn-Al at 450°C using electron probe microanalysis and metallographic techniques.

The growth characteristics of intermediate phases formed on iron galvanized in Al-bearing Zn at 450°C have been investigated by metallography and low angle X-ray diffraction. It has been confirmed that the inhibiting layer is composed of Zn-bearing Fe_2Al_5 and $FeAl_3$. While the $FeAl_2$ phase was erratically detected, we did not detect the presence of FeAl. X-ray diffraction data for $FeAl_2$, so far missing from the ASTM X-Ray Data File, have been recorded. A correlation of our results and that of other workers with our newly investigated and proposed ternary isotherm at 450°C using an analysis via diffusion paths on the isotherm has produced a convincing rationalization of the inhibiting effect and the catastrophic interface instabilities which develop preferentially in stagnant baths after long times and with the higher bath Fe contents.

ACKNOWLEDGMENTS

The author wishes to express his gratitude to Professor J.S. Kirkaldy for suggesting the topic of research, and for his encouragement and help during the course of this project.

Thanks are also due to Mr. H. Heumayer for technical assistance and to the author's wife for help with processing the electron microprobe data.

The surface diffraction analysis would not be possible without the assistance given by the staff of the Research Center of the Steel Company of Canada, which is especially appreciated.

The Special High Grade Zinc was supplied through the good offices of Mr. H. Guttman of Cominco Ltd. The high purity aluminum was provided by Alcan Research and Development.

The financial support of McMaster University in the form of a graduate fellowship is gratefully acknowledged.

TABLE OF CONTENTS

LIST OF TABLES

LIST OF ILLUSTRATIONS*

* The illustrations have been placed at the end of the thesis.

CHAPTER I

INTRODUCTION

It has been known for many years that aluminum of 0.1 - 0.3 wt.% in galvanizing baths inhibits the iron-zinc alloy layer growth. However, such additions were not used in early years since the aluminum reacted with the flux blanket on the bath causing hard particle inclusions in the coating. The use of aluminum additions was forced upon technology by the need for ductile, non-flaking coatings which are resistant to subsequent deformation associated with fabrication. In this new technology the growth of undesirable brittle iron-zinc layers at the steel-zinc interface is minimized through additions of 0.1 to 0.3 wt.% aluminum to the zinc bath and the previously associated inclusions are eliminated by modifications to the bath flux.

It has been qualitatively established that this inhibiting action is due to formation of aluminum-rich alloy layers. The purpose of this study was to more precisely establish the nature and growth characteristics of this alloy layer as a function of time, aluminum content and iron content of the zinc bath. We suppose that this type of information will provide a useful insight into the practical problems of controlling and minimizing the growth of the brittle iron-zinc layers at the iron-zinc interface.

The problem has been approached from two directions. Firstly, we have undertaken to obtain quantitative constitutional data for the

zinc-iron-aluminum system at 450°C, this temperature being characteristic for the galvanizing process. This part of the study was based on equilibration experiments and electron probe microanalysis. In the second part of the program the character and growth of intermetallic phases on galvanized specimens has been elucidated using a surface X-ray diffraction method, metallographic observation and electron probe microanalysis.

CHAPTER II

REVIEW OF PREVIOUS WORK

This chapter summarizes previous work on the phase diagrams for the binaries and ternaries of the Fe-Zn-Al system and on the formation of intermetallic phases at the iron-zinc interface in pure or aluminum-alloyed zinc baths.

2.1 The Iron-Zinc Binary System

The nature of the equilibria in the iron-zinc system can be regarded as well established. In contrast to the phase diagram reported by Hansen and Anderko[1] (Figure 1) recent research[2-5] reveals that the temperature of the gamma (γ)/alpha (α) transformation in the iron phase is first slightly lowered and then raised with increasing zinc content. The iron-γ field is accordingly almost enclosed by the α-iron phase (Figure 2).

Iron and zinc form four intermetallic compounds with varying homogeneity ranges. The Γ phase (Fe_3Zn_{10}) has a cubic crystal structure with zinc contents extending between 72 and 79 wt.%. The δ_1 phase ($FeZn_{10}$), with a hexagonal structure, has a composition lying between 88.5 and 93.0 wt.% Zn. The δ_1 phase undergoes a transformation $\delta_1 \rightarrow \delta$ in the temperature range 620° - 640°C. The δ phase probably has

the hexagonal structure as well[1].

The ξ phase is monoclinic with the narrow homogeneity range of 93.8 - 94.0 wt.% Zn. The three iron-rich compounds (Γ, δ and δ_1) form readily on cooling the appropriate alloys, while the formation of low temperature ξ phase is usually suppressed. This is the reason why the phase boundaries for the ξ phase were only established after discovery of this phase in metallographic studies of galvanized coatings[15]. The sluggish transformation rate is also associated with the fact that in the temperature range 530° - 500°C the transformation does not originate at the surface of the δ_1 crystals as would be expected in a peritectic reaction. Horstmann[6] has observed ξ phase crystallizing directly from iron-rich melts as δ_1 phase slowly dissolves. He noted that about 30° uncercooling was required to initiate a reaction which produced localized ξ phase in contact with the δ_1, and even higher undercoolings to produce an ξ phase which entirely enclosed the δ_1 phase.

2.2 The Iron-Aluminum Binary System

The iron-aluminum phase diagram, as reported by Hanson[1], is reproduced in Figure 3. Earlier uncertainties with respect to the disorder → order transformation have been resolved by Warlimont[6]. As shown in Figure 4 the peritectic reaction,

$$\text{melt} + \alpha \rightarrow \alpha_2$$

takes place between 17 and 21 wt.% Al, at 1440°C. The two-phase field

between α and α_2 (FeAl) terminates, according to Warlimont, at 540°C by the eutectoid reaction

$$\alpha_2 \text{ (FeAl)} \rightarrow \alpha + \alpha_1 \text{ (Fe}_3\text{Al)}$$

The consolute point for this phase was found to be at the co-ordinate 550°C and 15.2 wt.% Al. The Fe_3Al structure is of the BiF_3 type and the FeAl structure is isotypic with the CsCl structure.

The most important characteristic of this system in the high-Al region (34 - 100 wt.% Al) is the existence of three intermetallic phases. The phase $FeAl_2$ (ξ) was shown to be formed by the peritectoid reaction

$$\xi + \text{Fe}_2\text{Al}_5 \text{ (η)} \rightarrow \text{FeAl}_2 \text{ (ξ)}$$

at 1158°C which is only about 7°C below the ξ + η eutectic. The structure of the ξ phase was suggested by Osava[8] to be rhombohedral but Bradley and Taylor[9] claim that the structure is more complicated. The phase Fe_2Al_5(η) is stable within the range 53 to 56 wt.% Al having the orthorhombic structure.

There remains some uncertainty about the higher aluminum concentration limit of the $FeAl_3$ phase field. Nonetheless, the formula $FeAl_3$ is retained in our discussion for conciseness. The structure of this phase was found to be monoclinic.

2.3 The Aluminum - Zinc Binary System

The diagram of this system is presented in Figure 5. Recent investigations[1] established the peritectic reaction

$$L + (Al) \rightleftarrows \beta$$

The β is cubic. The near continuity of the parameters of β with (Al) is indicative of some sort of ordered structure based on (Al). Since (Al) and β are very nearly alike crystallographically, they cannot be distinguished metallographically.

Short range-order in 12 - 50 at.% Zn alloys from 340 to 380°C was observed. The solid-state immiscibility gap with boundary shown exhibits a maximum at 351.5°C and 39.5 at.% Zn.

2.4 The Iron-Zinc-Aluminum Ternary System

A knowledge of this ternary system (or at the very least the 450°C isotherm) was considered to be essential to the understanding of an aluminum affect on a formation of Zn-Fe alloy layers in galvanized coatings. When this work was begun only limited data of this kind was available.

The phase equilibria in the Zn-rich corner of the Zn-Fe-Al system containing up to 20 wt.% Fe and Al was investigated by Rennhack [10]. His partial isotherm established at 450°C by metallographic observation and X-ray diffraction is shown in Figure 6. Similar partial isotherms

were established at 600°C and at room temperature. The results of this important work may be summarized as follows:

(a) A four-phase invariant reaction:

$$L + FeAl_2 \rightleftharpoons FeZn_7 + Fe_2Al_5$$

was found to occur at about 592°C.

(b) The solubility of aluminum in $FeZn_{13}$ was found to be about 0.2 pct at 450°C. Unlike $FeZn_7$, this phase does not equilibrate with the FeAl compound phases.

(c) No ternary intermediate phases were found to occur within the temperature and composition ranges explored. That is to say, no X-ray lines were observed which did not correspond to binary compounds listed in the ASTM X-ray Powder Data File.

Cameron and Ormay[29] constructed a tentative 450°C isotherm of the Fe-Zn-Al system (see Figures 7 and 8). In their proposition all binary intermediate phases were assumed to bear only a few percent of a third element. The Zn-rich corner of the isotherm was based on metallographic observations of galvanized coatings, and a solubility of Fe in Zn was proposed to decrease with increasing aluminum content. A region of a ternary intermetallic compound was based on Hughes'[24] results.

The recent diagram of Köster and Gödecke[62], which corresponds most closely to our own observations, is discussed in detail in Chapter 6.

2.5 Galvanizing Reactions Between Iron and Zinc

During the reaction between iron and solid or molten zinc, compact alloy layers are formed in accordance with the phase order specified by the equilibrium diagram up to temperatures of about 490°C.

The layers include a thin Γ layer adjoining the iron, followed by a thicker layer of the δ_1 and ξ phases. Although the phase diagram predicts this sequence of the alloy layers for temperatures up to 530°C no ξ phase has been observed in galvanized coatings at temperatures above 500°C. The alloy layer consists of a thin Γ and a thicker δ_1 layer, a sequence of phases which persists up to 620°C.

In the temperature range between 620° and 640°C only two phases, Γ and δ_1, have thus far been identified despite the fact that layers of Γ, δ_1 and δ are predicted by the phase diagram. This sequence of two phases remains unchanged up to 672°C. As expected, between 672°C and 782°C, the only layer is Γ.

No iron-zinc alloy or intermetallic compound exists at temperatures above 782°C. At such high temperatures the iron is directly dissolved until the iron-rich melt becomes saturated. It is reported[16] that alpha-iron crystals are then precipitated in the melt. The latter, upon cooling, react with the melt and are converted into iron-zinc compounds. As the iron dissolves in the zinc, the latter also penetrates into the iron through diffusion, resulting in a diffusion layer of zinc-

rich alpha-solid solution. Cameron [11] found that even at temperatures below 782°C a layer of Zn-rich alpha solution is formed beneath the iron-zinc layers of the coating. This finding was later confirmed by Caloni et al [12,13] and by Horstmann et al [14].

While the nature of the phases formed in the galvanized coatings is well-established, there are many different interpretations of the formation sequence and the growth control mechanism for intermetallic phases. Cameron's investigation [15] on the sequence of alloy layer formation at 350°C shows that the ξ layer forms first. The δ_1 layer and the Γ layer only form in that order underneath the ξ layer some time after the latter has attained substantial thickness. Most observations indicate that this is also the sequence of formation at temperatures above the melting point of zinc. After a very short immersion time in the melt the alloy layer on an iron specimen consists almost entirely of small ξ crystals. With longer periods, a δ_1 layer is formed which grows rapidly once it appears, and the Γ layer follows later.

It has been established experimentally [16] that the kinetics of the attack on iron by zinc obeys two different time laws. Up to approximately 490°C and again between 520° and 740°C, the overall rate of growth of the alloy layers as determined by iron weight loss, follows a parabolic law, whereas the relationship is linear for the intermediate temperature range (490 - 520°C). However, opinions differ widely as regards the rate-law for individual alloy layers. Rate laws may be expressed generally by

$$d = c \cdot t^m$$

where d is the layer thickness, t the immersion time, c the rate constant, and m the growth rate exponent. Within the temperature range of overall parabolic attack the growth rate exponent has been found to vary between 0.13 to 0.5 for the Γ layer, between 0.5 to 0.64 for the δ_1 layer, and between 0.15 to 0.5 for the ζ layer.

During the reaction between iron and zinc the boundaries between the various phases migrate according to the laws of diffusion and mass conservation. The phase boundaries between the alpha-solid solution and the Γ layer and between the Γ and δ_1 layers shift towards the iron whereas the other phase boundaries move towards the zinc[16]. This implies that the Γ layer is continuously formed at the iron boundary and dissociated in contact with the δ_1 layer. Similarly, the ζ phase forms continuously where it contacts the zinc but is dissociated into δ_1 where it borders this growing phase.

2.6 The Effect of Aluminum Additions to the Zinc Bath on the Growth of Alloy Layers on Iron

In the previous chapter, it was understood that the reaction was taking place between iron and zinc with negligible amounts of impurities. The problem of layer growth becomes much more complicated if alloying elements are added either to the iron or to the zinc bath. From references (17-21) we conclude that the silicon (Si) and carbon (C) contents of the steel intensify substantially the parabolic zinc attack and at the same time greatly reduce the lower limit of the temperature range in which linear attack occurs. Likewise, higher phosphorus (P)

should be avoided in galvanizing grades of steel although the P contents of up to 0.08 wt.% usually present in commercial steels are only of minor consequence. Manganese (Mn) impurities in the quantities usually present in commercial steels, are of no significance.

The rate of zinc attack in the parabolic range can be beneficially altered by selective alloying of zinc baths of conventional composition. The most consistently effective additions in this respect are found to be 0.1 - 0.5 wt.% of vanadium, chromium, nickel, manganese, silicon and/or aluminum. This present contribution is concerned entirely with the latter very effective addition.

As pointed out earlier the growth of the brittle iron-zinc alloy layer at the steel-zinc interface can be effectively controlled by adding about 0.10 to 0.30 % aluminum to the zinc bath. Current efforts to determine the mechanism by which aluminum inhibits iron-zinc alloy layer growth have led to the conclusion that a barrier of aluminum-rich alloy layer forms at the steel-zinc interface. In an extensive work Bablik[22,23] has examined a wide range of temperatures and aluminum contents, mainly under conditions of iron saturation.

In galvanizing tests, dipping for a minute is regarded as a short time. A static specimen is usual. Bablik noted that aluminum delayed the onset of the fast reaction between liquid zinc and solid iron for short immersion times but that once the reaction started, the iron attack was greater than that in a bath without aluminum. A thin layer of $FeAl_3$ was considered to be responsible for inhibiting the iron-zinc alloy growth.

Hughes[24,25] summarized the literature on Al-controlled inhibition prior to 1950. In his own experimental work, four types of materials were galvanized: armco iron, commercial low-carbon cold reduced steel sheet of rimming quality steel containing 0.10 wt.% carbon, killed steel but containing only traces of silicon and steel containing 0.22 wt.% carbon and 0.10 wt.% silicon. Times of immersion ranged from 5 to 60 seconds. The temperatures used varied from 430°C to 490°C and aluminum additions from 0.05 to 3 wt.%. The bath was prepared from pure zinc.

For the bath containing 1.5 wt.% Al a ternary alloy formed at the iron-zinc interface was identified by chemical analysis. X-ray examination of this layer revealed that it generated powder lines of $FeAl_3$. The following conclusions were drawn:

(a) The ternary iron-zinc-aluminum layer at the steel interface inhibits the growth of iron-zinc alloy layers.

(b) A secondary alloying process which occurs under the "ternary" alloy causes the latter to break away and form loose crystals in the coating. The occurrence of this secondary alloying is erratic and more information is needed about it.

(c) The presence of silicon in steel enhances the stabilizing effect of aluminum.

(d) The aluminum level necessary to limit the iron-zinc alloy layer growth is increased in rough proportion to bath temperature and immersion time.

Haughton[26] drew attention to the role of dissolved iron in conjunction with the aluminum in the bath. His steels contained only trace amounts of tramp elements. The aluminum contents of the baths were 0, 0.05, 0.10 and 0.20 wt.% aluminum. For each of these four aluminum contents the iron in the bath was varied progressively from zero up to saturation (about 0.03 % at 450°C). The temperature of the zinc bath was maintained at 450°C throughout. Dipping times of 1 minute and 5 minutes were used. To discriminate between the effect of local iron enrichment and the general iron content of the bath two parallel sets of experiments were carried out - one with samples suspended in the bath without movement and the other with samples agitated with the object of dispersing local iron enrichment. The weight loss of the iron substrate of the specimens was determined, along with metallographic observations. X-ray examination of samples scraped from specimens stripped of their zinc revealed the presence of the phase Fe_2Al_5 provided the aluminum level was above 0.1 wt.% in the bath. From the above observations under the stated conditions the following conclusions were offered:

(a) Variations of the iron content of the bath containing only zinc and iron has no observable effect upon the metallographic structure of the coating or upon the rate of attack on the steel in the bath.

(b) The addition of 0.05 wt.% of aluminum to zinc containing various amounts of iron has very little effect upon the metallographic structure of the coating or upon the rate of attack on steel in the bath.

(c) The addition of 0.1 wt.% of aluminum to the zinc profoundly modifies the structure of the coating and the rate of attack. With baths low in iron the normal alloy layers are absent except for occasional layer growths. Instead, a very thin layer, probably Fe_2Al_5, is formed on the steel surface which largely blanks off the attack on the steel. As the iron content of the bath rises, however, there is an increasing tendency towards local attack with growth of heavy, rather loose, alloy layers. Thus, for a bath saturated with iron and containing > 0.1 wt.% Al, weight loss is even higher than when aluminum is not present in the bath.

(d) The addition of 0.2 wt.% of aluminum to the bath gives similar results, but the protective film formed is thicker and the formation of local areas of heavy attack is less frequent. Consequently, the weight of steel lost is lower, and even with a bath saturated in iron, the attack is largely blanked off.

(e) The whole picture suggests a very unstable state, where a slight change in conditions (e.g., in iron content of the bath, or surface condition of the steel) may completely reverse the direction of the inhibiting effect of aluminum additions to the bath.

Horstmann[27] established the minimum aluminum content necessary for inhibition as a function of temperature. Material used was armco iron and a steel with very low amount of all elements other than carbon. The zinc bath contained 0.10, 0.20, 0.30 and 0.50 wt.% of aluminum, being

always freshly prepared, apparently with no purposely added iron. The temperatures of the zinc baths ranged from 440°C to 500°C and times of immersion ranged from 5 sec. to 5 hours. The effect of agitation was examined as well. The weight loss analysis along with metallographic and surface X-ray examinations allowed Horstmann to draw the following conclusions:

(a) For higher amounts of aluminum (~ 0.5 wt.%) a distinctive gray layer firmly adhering to the iron at the iron-zinc interface was observed if the examination occurred during the period of the inhibition. Below this layer scattered crystals of a lighter colour were noticed. The X-ray analysis of this sample (see Table I) revealed the presence of Fe_2Al_5, which was considered to be the continuous gray layer. The unidentified lines (see last column of Table I) were ascribed to an unknown ternary Fe-Zn-Al compound and identified with light gray crystals underlying the continuous layer of the Fe_2Al_5.

(b) For the specimen prepared at the same aluminum content but examined after the inhibiting effect had ceased the X-ray analysis (see Table II) revealed the presence of Fe_2Al_5 and FeAl. The unidentified lines (see last column of Table II) differed from those in the previous case and were thus ascribed to another ternary Fe-Zn-Al.phase.

(c) It was proposed that access of the zinc bath to the iron is prevented by a protective layer of Fe_2Al_5 which initially forms on the iron

TABLE I

The Results of X-Ray Analysis of Stripped Specimen Prepared in Zinc with 0.5 wt.% Al, at 440°C, 75 min, after Horstmann[27]

Gefundene Linien		Linien des Fe			Ausdeutung Linien des Zn			Linien des Al_5Fe_2		Ungedeutete Linien	
d in A	Intensität	d in A	Indices	Intensität	d in A	Indices	Intensität	d in A	Intensität	d in A	Intensität
7.12	1									7.12	1
4.91	0.5							4.90	11		
3.81	4							3.86	24		
3.53	1									3.53	1
3.20	8							3.20			
2.75	7							q		2.75	7
2.47	2				2.46	(002)	25				
2.45	1.5									2.45	1.5
2.41	1.5									2.41	0.5
2.39	0.5							2.39	10		
2.33	6				2.30	(100)	20			2.33	6
2.31	2.5										
2.28	1.5									2.28	1.5
2.24	1									2.24	1
2.23	2									2.23	2
2.11	30							2.11	100	2.11	20
2.09	9				2.08	(101)	100				
2.06	10							2.05	110		
2.03	4	2.03	(110)	100							
1.94	13							1.94	10	1.94	10
1.90	1							1.90	8		

TABLE II

The Results of X-ray Analysis of a Stripped Specimen Prepared in a Zinc Bath with 0.5 wt.% Al; at 480°C, 15 min, after Horstmann[27]

Gefundene Linien		Linien des Zn			Ausdeutung Linien des Al_5Fe_2		Linien des FeAl			Ungedeutete Linien	
d in A	Intensität	d in A	Indices	Intensität	d in A	Intensität	d in A	Indices	Intensität	d in A	Intensität
3.79	5									3.79	5
3.21	3.5				3.20	40					
2.91	5.5						2.89	(100)	12		
2.58	0.5									2.58	0.5
2.36	1.5				2.39	10					
2.35	1.5									2.35	1.5
2.29	0.5	2.30	(100)	20						2.29	
2.26	2.5									2.26	2.5
2.18	2									2.18	2
2.166	2									2.166	2
2.148	1.5									2.148	1.5
2.122	8									2.122	8
2.110	5				2.11	100					
2.075	8	2.08	(101)	100						2.075	
2.055	36				2.05	100	2.04	(110)	100		
1.938	1.5				1.94	10					
1.895	2.5				1.90	8					

surface. This Fe_2Al_5 layer later reacts with the bath and transforms into other Fe-Al and Fe-Zn-Al compounds, a situation leading to increased iron attack and alloy layer growth.

In a later study[28] Horstmann expanded on this explanation, listing type of steel, surface condition, and strip temperature in entering a continuous galvanizing bath as factors affecting the growth of the inhibiting layer.

Cameron and Ormay[29], again using steel low in all alloying elements, covered the temperature range 440 - 450°C for aluminum contents between 0 and 10 wt.% for times from five seconds to two hours, with and without agitation. The zinc bath used was characterized by the authors as iron dross-saturated.

The problem of the aluminum effect was for the first time considered in terms of the ternary Fe-Zn-Al equilibrium diagram, a tentative section of which was constructed (see Figures 7 and 8). The phases Fe_2Al_5 and an aluminum-bearing δ_1 ($FeZn_7$) were identified by X-ray diffraction. In this connection it was noted that the aluminum-bearing δ_1 had X-ray lines similar to those of the ternary compound ostensibly identified by Horstmann at 480°C.

Finally, they claim to have identified aluminum-bearing ζ and δ_1 phases as well as the previously unidentified ternary compound[26] using electron probe microanalysis. On the basis of this work, Horstmann's proposal for protective layer evolution was amplified.

Most recently, Borzillo and Hahn[30] examined the growth of the inhibiting aluminum-rich alloy layer on coatings developed in a pure zinc bath containing 0.20 to 0.30 wt.% of aluminum with varying iron levels. The specimens were cold-rolled annealed steel sheet with very

low contents of tramp elements. Immersion temperatures for each bath composition were 430°C, 450°C and 470°C. Immersion times ranged from 20 to 320 seconds. The growth rate of the aluminum-rich alloy layer was determined gravimetrically. The inhibiting layer was further examined with optical and electron microscopes and was also analyzed with the electron microprobe and by surface X-ray diffraction. Their conclusions can be summarized as follows:

(a) The inhibiting aluminum-rich alloy layer was found to grow parabolically as a function of bath temperature, immersion time and the aluminum: iron ratio of the bath. Growth rates were positively monotonic with the Al/Fe ratio of the bath.

(b) A detailed picture of the growth and phase changes in the aluminum-rich alloy layer was proposed. During a brief initial period of immersion (up to 20 sec), characterized by a straight-line interface, a stable low-diffusivity layer of Fe_2Al_5 forming on the surface of the steel inhibits the iron-zinc alloy layer growth. With longer times the zinc bath reacts with the Fe_2Al_5 layer and isolated blue-gray nodules, characteristic of a supposed ternary phase, begin to appear in this layer. As the nodules grow, the thin protective layer of Fe_2Al_5 is being consumed. Although the cause of initial nucleation of the ternary phase is not made clear, the growth of this phase is supposed to be favoured by high iron contents within the bath. With even longer immersion times, the nodules of the supposed ternary phase continue to grow and coalesce. At this stage the Fe_2Al_5

layer is completely consumed or penetrated, a consequence which directly exposes the steel base to the zinc bath, resulting in the localized and accelerated growth of iron-zinc phases.

CHAPTER III

THEORY

The problems of the inhibiting action of aluminum requires a discussion of the mass transfer from the solid to liquid metal as well as the diffusive growth of intermediate phases. The concept of a diffusion path on a ternary isotherm will be found useful in the discussion of instabilities observed which lead to the breakdown of inhibition. It should be recognized from the start that galvanizing is essentially an isothermal solidification process.

3.1 The Motion of Planar Phase Interfaces in Multicomponent Multiphase Systems

In the absence of surface reaction control, which is unlikely in metal-metal interactions, we can regard galvanizing as a multiphase counter-diffusion process. The problem of linear interdiffusion of two different multicomponent phases in the form of diffusion couples, with or without the appearance of intermediate phases in the diffusion zone, has been analyzed by Kirkaldy[31].

The general system of one-dimensional diffusion equations for multicomponent diffusion in a substitutional solution are:

$$J_i = - \sum_{k=1}^{n-1} D_{ik} \frac{\partial C_k}{\partial x} \qquad (3.1)$$

and

$$\frac{\partial C_i}{\partial t} = \sum_{k=1}^{n-1} \frac{\partial}{\partial x} \left[D_{ik} \frac{\partial C_k}{\partial x} \right] \tag{3.2}$$

These have the parametric solutions:

$$C_i = C_i(\lambda), \quad \lambda = x/\sqrt{t} \tag{3.3}$$

provided the initial and boundary conditions can be expressed in terms of λ. This is, in fact, the case for we can summarize them simply by:

$$C_i \ (+\infty) = C_{i1} \tag{3.4}$$

and

$$C_i \ (-\infty) = C_{iN} \tag{3.5}$$

These parametric solutions were shown to exist in linear multiphase systems provided that local equilibrium is approached at all interfaces, irrespective of the number of phases which appear in the diffusion zone of the couple. Any diffusion measurement that confirms equation (3.3) demonstrates uniquely that very close to interfacial equilibrium or metastable equilibrium is maintained throughout the diffusion period.

The only preconditions to be imposed on the terminal alloys in this description are that they be homogeneous solid solutions, that diffusion be structure-independent, and that the constitution allows diffusion to proceed from them without any compositions appearing in the

zone which imply a failure of the planar interface assumption (e.g., two-phase mixtures).

Now if the penetration curve for an n-component alloy involving a total of N phases is considered, then each continuous region of the penetration curve can be described by the solution of the ordinary equations:

$$-\frac{\lambda}{2}\frac{dC_i}{d\lambda} = \sum_{k=1}^{n-1}\frac{d}{d\lambda}\left[D_{ik}\frac{dC_k}{d\lambda}\right] \tag{3.6}$$

which fits the appropriate phase boundary compositions. In general, the D_{ik} are functions of all the concentrations, but in order to obtain an analytic solution they are assumed to be an appropriate average value for each phase.

The co-ordinates of the interface, ξ, are determined simultaneously with the interface concentrations by application of interface continuity relations of the form:

$$(C_{i21} - C_{i12})\,\xi_{21} / 2\sqrt{t} = J_{i12} - J_{i21} \tag{3.7}$$

and the equilibrium conditions. In this evaluation there are $2(N-1)n$ interface concentrations plus $(N-1)$ phase boundary co-ordinates as unknowns and these are uniquely determined by the $(n-1)(N-1)$ independent relations of type (3.7), the $n(N-1)$ equilibrium free energy relations of the form:

$$\mu_{i1}\,(C_{112}, C_{212}, \cdots C_{n-1,12}) = \mu_{i2}\,(C_{121}, C_{221}, \cdots C_{n-1,21}) \tag{3.8}$$

and the 2(N-1) concentration balances of the form:

$$\sum_{i=1}^{n} C_{i12} = 1 \tag{3.9}$$

The required solutions then take the form:

$$C_i = d_{i0} + \sum_{k=1}^{n-1} d_{ik} \int_{\lambda}^{\xi_{\ell j}} \exp\left[-\lambda^2/4u_k\right] d\lambda \tag{3.10}$$

subject to the indicial equations

$$u_k = \sum_{j=1}^{n-1} \frac{d_{jk}}{d_{ik}} D_{ij} \tag{3.11}$$

and the appropriate phase boundary values.

In the evaluation of the coefficients the integrals can be normalized by letting:

$$a_{ik} = d_{ik} \Big/ \int_{\xi_{\ell+1, j+1}}^{\xi_{\ell j}} \exp\left[-\lambda^2/4u_k\right] d\lambda \tag{3.12}$$

where d_{ik} are functions of the boundary C's and the D's as determined equation (3.11). The complete numerical calculation involves as well the solution of the simultaneous non-linear set of equations (3.7) with the phase diagram equivalent of sets (3.8) and (3.9).

In testing the validity of this phenomenological description it is sufficient to demonstrate experimentally that equation (3.3) is

valid, or that approximate equilibrium is maintained throughout the diffusion process.

3.2 Isothermal Solidification into a Binary Liquid

As a special case of the foregoing general analysis, we may consider motion of a planar interface in a binary solid-liquid system. For this case the surface reaction is assumed to be fast enough to maintain the local equilibrium condition, so that the concentration at the interface is given by the phase diagram. The concentration distribution in the solid and liquid (considered as semi-infinite media) is given by the solution of Fick's Second Law:

$$D_L \frac{\partial^2 C}{\partial x^2} = \frac{\partial C}{\partial t} \quad , x < Z \tag{3.13}$$

$$D_S \frac{\partial^2 C}{\partial x^2} = \frac{\partial C}{\partial t} \quad , x > Z \tag{3.14}$$

The mathematical analysis follows that given by Wagner[32]. The initial and boundary conditions are illustrated in Figures 9(a) and 9(b). The continuity of mass flow at the solid-liquid interface is then given by:

$$D_L \left(\frac{\partial C}{\partial x} \right)_{Z^-,t} = D_S \left(\frac{\partial C}{\partial x} \right)_{Z^+,t} + z(C_S - C_L) \tag{3.15}$$

The value of x at the interface is denoted by Z and is a function of time. The diffusion coefficients are assumed to be independent of concentration. With these assumptions the displacement, Z, of the solid-liquid interface is given by :

$$Z = 2\gamma \sqrt{D_L . t} \tag{3.16}$$

A particular solution of (3.13) and (3.1) which satisfies the boundary conditions at $\pm \infty$ and the initial conditions is given by:

$$C = C_o + A \left[1 + \text{erf } (x/2\sqrt{D_L t})\right], \quad x \lesssim Z \tag{3.17}$$

$$C = C_l + B \left[1 - \text{erf } (x/2\sqrt{D_S t})\right], \quad x \gtrsim Z \tag{3.18}$$

The boundary conditions at the interface x = Z, given in Figure 9(b), can be satisfied by combining equations (3.15), (3.16) and (3.7), (3.18). The constants A and B can be eliminated by use of boundary conditions at x = Z and equations (3.17), (3.18). The result is a transcendental equation relating γ with the composition parameters of the system. In the case that D_S is much smaller than D_L the expression for γ can be greatly simplified to:

$$\Gamma(\gamma) = \sqrt{\pi}\,\gamma \,(\exp \gamma^2)\,[1 + \text{erf}\gamma] = \frac{C_L - C_o}{C_l - C_L} \tag{3.19}$$

3.3 Representation of Diffusion Paths on the Isotherm

The above analysis of the motion of planar phase interfaces for multicomponent multiphase systems assumes as a prior stability condition that all interfaces remain flat throughout diffusion and for this to be so we invoked the requirement that no compositions should appear which imply a failure of this planar interface assumption. As we well know, irregular and non-planar morphologies are often observed during the growth of oxide scales on alloys and in isothermal phase transformations in multicomponent metallic systems[33,34,35,36], including galvanizing. Such morphologies reflect isothermal diffusion instabilities that can arise in multiphase diffusion due to the additional degree of freedom in the composition if the third element is added. It is apparent at this point that when the above planar analysis leads to results that are inconsistent with the prior caveat against irregular and non-planar morphologies, then that analysis must be a successful predictor of such instabilities.

All isothermal ternary diffusion profiles with parabolic kinetics can be mapped onto the isotherm. Through elimination of the λ-co-ordinate four schematic diffusion paths are plotted in Figure 10. Path ab is stable implying as it does the formation of a planar interface between a terminal solid solution and an intermediate phase A_nC_m. Paths cd and ef, on the contrary, cross the tie-lines in two phase regions and thus imply the existence of supersaturation in the terminal solid solution diffusion zone. This is a consequence of $D_{11} >> D_{22}$, a condition most commonly leading to diffusion instability. Such unstable

paths, calculated on the basis of ternary diffusion theory and the assumption of stable planar interfaces have been designated as "virtual paths"[34]. The relief of the predicted supersaturation leads to serrated interfaces and internal precipitation, i.e., to multiphase zones along the path.

The theory of kinetic interface instabilities was introduced by Wagner[37] and this has been extended into a general theory of ternary interface instability by Coates and Kirkaldy[38] and by Coates[39]. The latter theories, however, focus on marginal instability so are of little help in the treatment of the catastrophic instability which arises from the high virtual supersaturations indicated in Figure 10. Kirkaldy[40] has recently treated the catastrophic case of internal oxidation or sulphidation by methods which may ultimately point to a description of the much more complicated morphological instabilities which occur during galvanizing.

3.4 Some Qualitative Factors Controlling Stability of Interfaces

The foregoing analysis of instabilities is strictly applicable to solid infinite or semi-infinite diffusion couples for which the number of intermediate phases is usually defined from time zero. Under such conditions the diffusion path is also uniquely defined by the initial composition differences of all the elements. In contrast, in the galvanizing process, the diffusion couple consists of solid iron and liquid zinc in an initial condition whereby the intermediate phases must be established through a series of consecutive nucleation steps, the order being determined by the relative strain and interfacial free energy magnitudes of those metastable configurations which are thermodynamically

possible. The sequential nucleation of more stable intermetallic phase relationships must lead, after characteristic relaxation times, to discontinuous modifications of the diffusion paths.

This discontinuous character may be further abetted by depletion of the liquid in minor components. This depletion effect will be particularly pronounced if the nucleated intermetallic phases are rich in a component which can be supplied only from the liquid part of the couple (as in the case of an aluminum-bearing zinc bath), resulting in changes in the interfacial concentrations at the solid-liquid interface. Such changes can be particularly important locally if the metastable diffusion paths are morphologically unstable as described in Section 3.3.

Furthermore, the depletion of elements near the interface in the liquid may be dispersed by agitation allowing the initial activity of minor components in the bulk liquid to be maintained at a higher level at the solid-liquid interface than determined by parabolic kinetics.

The relevance of the above general comments are explored in Section 6.3 for galvanizing reactions in the ternary system Fe-Zn-Al.

CHAPTER IV

EXPERIMENTAL METHOD

This chapter describes the experimental determination of the equilibrium data for the Fe-Zn-Al system and the hot dipping experiments. The first section is concerned with preparation of materials while the later sections describe the experimental design, equipment and particular procedures utilized.

4.1 Preparation of Materials

4.1.1 Iron Sheets

The sheets for the dipping experiments were prepared from Armco iron to minimize the effect of alloying elements and impurities on the growth characteristics of alloy layers. For all specimens used the following standard procedure was adopted: A piece of Armco iron ($\sim$ 100 gm) was remelted in pure argon. The buttons obtained were annealed at a temperature of 1000^{o}C for 96 hours in a hydrogen flow and cold-rolled afterwards to an average thickness of 0.3 mm. These sheets were then cut into specimens of 25 mm by 50 mm and again annealed at a temperature of 1000^{o}C for 96 hours in a hydrogen flow. The chemical analysis of the sheet specimens is given in Table III. The sheet specimens were then prepared for galvanizing using a procedure described in Section 4.2.3.

TABLE III

Analysis of the Iron Sheets
(percent by weight)

C	Si	Mn	P	S
0.01	<0.01	0.034	0.003	0.004

TABLE IV

Analysis of Basis Materials
(percent by weight)

	Zn	Fe	Pb	Cd	Cu
Special High Grade Zinc	99.9975	0.001	0.0012	0.0001	0.0002
	Al	Fe	Si	Mg	Cu
Superpurity Aluminum	99.993	0.001	0.002	0.002	0.002

4.1.2 Zinc Baths for the Dipping Experiments

In Chapter III it was shown that both the aluminum and iron contents of the zinc bath have an important effect on the formation and growth of intermediate phases during galvanizing. For the study of such effects five iron-saturated zinc baths with increasing aluminum contents were prepared. The basis metals were Armco iron sheet having the chemical composition given in Table III, a special high grade zinc supplied by Cominco Ltd., and super-purity aluminum supplied by Alcan Research and Development, Ltd. The analysis of these starting materials is given in Table IV.

A master alloy of 50 wt.% Al, 50 wt.% Zn was first prepared by induction melting, the appropriate portion of each material in a flow of argon. The alloy was then remelted for homogenization and cooled slowly.

For each bath an appropriate amount of Zn-Al master alloy and fine Armco chips were charged into a graphite crucible along with approximately 2,350 gm of special high grade zinc. The zinc was melted and maintained for adequate mixing at a temperature of 450°C for 48 hours. A sample of about 2 gm was then taken in a pyrex tube from the center of the bath and analysed chemically.

4.1.3 The Intermetallic Compounds of the System Iron-Aluminum

The binary compounds of this system were used for the equilibrium experiments and served also as standards for electron microprobe

analysis. The basis materials used for their preparation were the Armco iron and superpurity aluminum as described in the previous section. In all, four intermetallic compounds, FeAl, $FeAl_2$, Fe_2Al_5 and $FeAl_3$ were prepared. Approximately 90 to 100 grams of weighed base metals were placed into the melting chamber of a non-consumable arc furnace. A tungsten electrode was used for the melting operation, which was carried out under an atmosphere af argon. The reaction between molten aluminum and iron is exothermic so that fusion of the charges took only a few seconds. The buttons obtained for each compound was crushed and placed in a quartz tube. The tube was then alternately evacuated and purged with argon four times and then sealed. All compounds prepared by this procedure were then homogenized under the conditions given in Table V.

All annealed compounds were analyzed chemically. As can be seen from Table VI all compounds lie well within the homogeneity range as given by the binary phase diagram. The metallographic examination showed no secondary phases present in any of the compounds.

4.1.4 The Intermetallic Compounds of the System Iron-Zinc

The δ_1 and ξ compounds of the iron-zinc system were prepared to serve primarily as standards for electron probe microanalysis. In preparing these compounds the procedure proposed by Köster[42] was followed. Armco iron sheets were cut into thin strips. After weighing out the desired amounts of iron and zinc for the ξ-phase, the mixture of total weight 10 g, was packed in a quartz tube and sealed under vacuum. The ampoule was slowly heated up to 450°C and maintained at

TABLE V

Annealing Conditions for Iron-Aluminum Intermetallic Compounds

Compound	Annealing Conditions	
	Temperature °C	Time (hours)
FeAl	1000	170
$FeAl_2$	1000	170
Fe_2Al_5	1000	170
$FeAl_3$	650	170

TABLE VI

Chemical Analysis of Iron-Aluminum Intermetallic Compounds (percent by weight)

Compound	Iron Content		Aluminum Content	
	Phase Diagram	Actual	Phase Diagram	Actual
FeAl	67.43	66.57	32.57	33.24
$FeAl_2$	51.0 - 51.5	51.19	48.5 - 49.0	49.99
Fe_2Al_5	44.0 - 47.0	45.12	53.0 - 56.0	55.55
$FeAl_3$	39.0 - 42.0	41.84	58.0 - 61.0	57.58

this temperature for 6 hours. Then the temperature was raised to 600°C. Tilting the tube continually for mixing, the temperature was slowly increased to 850°C. Holding time at this temperature was 70 hours. During slow cooling down to 700°C the sample was again tilted for better mixing of the melt, and then left in the horizontal position to avoid bursting of the ampoule as a consequence of the volume increase of the δ_1-phase. After reaching 400°C the sample was left at this temperature for 72 hours, and then cooled to room temperature. The same procedure was adopted for the preparation of δ_1-phase.

The compounds obtained were homogeneous. However, both of them exhibited excessive porosity which was considered to be unacceptable. Accordingly, the following powder metallurgical method of preparation was adopted. Iron powder of purity 99.95 wt.% and zinc powder of purity 99.99 wt.% were used as basis materials. Appropriate amounts of each metal powder was weighed to give a total weight of 6 grams. The samples were then mechanically mixed for eight hours. For each alloy three pellets weighing 1 gram were prepared by pressing the mixtures in an 8.7 mm (11/32") diam. die at a pressure of 5500 psi for 5 minutes. The pellets obtained were pre-sintered in a hydrogen atmosphere at a temperature of 500°C for 2 hours. The pellets were subsequently placed in quartz tubes, evacuated five times and alternately purged with argon, sealed in vacuum and sintered for 18 days at 500°C. After sintering the samples were quenched by breaking the capsules under ice water. The ζ and δ_1 compounds prepared were compact, and metallographic observations did not reveal the presence of second phases. Chemical analysis of the two phases is given in Table VII.

TABLE VII

Chemical Analysis of Iron-Zinc
Intermetallic Compounds
(Percent by weight)

Compound	Iron Content	Zinc Content
ζ	6.03	93.97 (by difference)
δ_1	9.04	90.96 (by difference)

4.1.5 The Intermetallic Compounds of the Ternary System Iron-Zinc-Aluminum

Prepared ternary compounds in this system were to be utilized as standards for electronprobe microanalysis in the proposed equilibrium experiments. This task of preparation was complicated by the fact that, as discussed in Chapter II, very limited data were available on the ternary system Fe-Zn-Al. We recall that examination of galvanized coatings had established the presence of Fe_2Al_5 along with an unknown ternary compound. Constitutional work[10], on the other hand, seemed to deny the existence of a unique ternary phase. Our own preliminary work[43] with compounds FeAl and Fe_2Al_5 equilibrated in zinc had on the other hand, indicated the presence of an unknown ternary phase.

We proceeded on the basis of a proposed ternary isotherm at 450°C like that in Figure 7, and prepared a set of ternary alloys consisting of powder mixtures of various pure metal powders. These ternary alloys were fabricated using the powder metallurgy technique described above. For example, starting at the middle of the homogeneity range of Fe_2Al_5 ternary alloys with increasing Zn content and approximately constant iron content (i.e., directed towards the postulated unknown ternary phase) were prepared. Similarly, alloys originating from the δ_1-phase were prepared having increasing amounts of aluminum at constant iron content. Metallographic observations and X-ray analysis were then applied to identify the presence of various phases.

Gebhardt[44], in attempting to prepare ternary alloys of the Fe-Zn-Al system, experienced enormous dilatation of samples with iron contents above 10 wt.%, irrespective of the method of preparation. This

substantial increase in volume resulted in a complete disintegration of solid compounds into powder. To circumvent this problem the following procedure was adopted. As basis materials aluminum powder 99.98 wt.% (325 mesh), iron powder 99.95 wt.% (325 mesh) and zinc powder 99.99 wt.% (200 mesh) were used. The preparation was carried out in the same way as described in the previous section for ξ and δ_1-phases except that after presintering, at which point samples were partially disintegrated due to the large volume increase, the pellets were re-pulverized, compressed at the stated conditions and sintered in evacuated quartz tubes at 500°C for 18 days. The resulting sintered pellets were satisfactorily stable and compact.

The nominal compositions of the prepared alloys are given in Table VIII along with the results of chemical analysis of the sintered alloys.

The metallographic examination of alloy number 1 did not reveal the presence of any other phase than the expected δ_1. In alloy number 2 a very small amount of phase other than δ_1, probably Fe_2Al_5, was detected. X-ray analysis of these alloys matched the three lines listed for the δ_1-phase in the ASTM X-Ray Data File. Surprisingly, metallographic examination of alloys number 3, 4 and 5 did not reveal the presence of phases other than Fe_2Al_5 (presumably with dissolved zinc). The X-ray powder analysis yielded d-spacings which were in good agreement with those reported for Fe_2Al_5 in the ASTM X-Ray Data File[45]. Alloy No. 6 exhibited substantial amounts of a second phase, which other tests (see below) identify as δ_1.

On the basis of X-ray and metallographic analysis the alloys numbered 1 and 5 were selected as standards for microprobe analysis.

TABLE VIII

Nominal Composition and Chemical Analysis of Ternary Compounds

Alloy Number	Nominal Composition			Chemical Analysis		
	Fe	Zn*	Al	Fe	Zn*	Al
1	9.00	89.00	2.00	8.94	89.10	1.96
2	9.00	87.00	4.00	8.74	87.33	3.93
3	44.00	3.00	53.00	44.08		53.20
4	43.00	8.00	49.00	43.11		48.72
5	43.00	12.00	45.00	42.82		44.60
6	43.00	16.00	41.00	42.70		41.43

* Zn by difference

4.2 Experimental Apparatus and Procedures

The investigation of the mechanism whereby aluminum inhibits iron-zinc alloy layer growth was directed experimentally in two main directions. First, through long-time equilibrium experiments, basic data on the Fe-Zn-Al isotherm at 450°C was obtained. These results were then correlated with those obtained by metallographic, X-ray and electron probe microanalysis of galvanized samples.

4.2.1 Determination of the Liquidus in the Zinc-Rich Corner of the Ternary System Iron-Zinc-Aluminum

As pointed out in Chapter II the iron content of an aluminum bearing zinc bath has a significant bearing on the inhibiting effect of aluminum. To assist in the control of this variable a precise determination of the liquidus line was attempted for the range of aluminum contents used in the subsequent dipping experiments.

Edmunds[46] has reported a value of 0.029 wt.% for the solubility of iron in pure zinc at a temperature of 450°C. We have used a similar methodology to determine the solubility of iron in zinc containing 0.21 wt.% of aluminum at 450°C. The apparatus used for this experiment is shown in Figure 11. A graphite crucible, of the dimensions shown, protected by a steel shell, was placed in an electric resistance furnace. The stirring paddle could be exchanged for a sampling tube as explained later. The temperature of the bath was controlled by a chromel-alumel thermocouple which was calibrated using the melting point of the special high grade zinc (99.9975 wt.%). The

thermocouple was protected by a pyrex tube. The furnace itself operated with a controlling accuracy of $\pm$ 1°C, a control stability of 0.5° or better, a control sensitivity of 1 microvolt or 0.1°C and a long term stability of $\pm$ 30 microvolts or 3/4°C over a one week period.

Prior to the experiment the crucible was charged with zinc, heated to 450°C and the top covered with insulation. After 5 days the variations of temperature along the vertical axis of the crucible were measured. There was a uniform gradient in temperature between the bottom and the top of the zinc bath and the maximum difference was 1.5°C. The slight error due to this difference was essentially eliminated by measuring the temperature of the bath during an actual experiment at the central, half-height point.

For the experiment the crucible was charged with 1930 grams of special high grade zinc. After melting at 445°C the desired amount of aluminum was introduced through the Zn-Al master alloy. Very fine strips of Armco iron were then introduced in amounts approximately twice that needed to saturate pure zinc at 450°C. After 24 hours, the stirrer was engaged for 3 hours, during which operation the temperature slightly increased due to the mechanical work exerted on the bath. When the stirring was stopped, the controller setting was adjusted to keep the melt at the maximum temperature attained during agitation, the stirring paddle was removed, the melt skimmed and the evacuated sampling tube introduced into the bath. The top opening of the furnace was then closed with asbestos plates and glass wool. Next the temperature controller was adjusted to 450°C and the actual temperature was monitored continuously throughout the remainder of the experiments.

Equilibrium was therefore approached via an undersaturated liquid solution. Solid constituents which precipitated from the melt could settle or rise, depending on their density relative to the melt density. Because Fe and liquid Zn have close to the same density, the time required for this separation, which was essential for valid melt sampling, was from 2 to 4 weeks. Our criterion for separation was that the results for chemical analysis taken one week apart had to differ by no more than the estimated experimental error.

Using the same bath, the temperature was then raised to 460°C, left for 24 hours, stirred, insulated and the temperature adjusted again to 450°C. By the same sampling procedure as above, the point on the liquidus line was therefore approached from a supersaturated melt.

Maximum variations of temperature during the equilibration-period were observed to be $\pm$ 1.6°C. The overall error involved in the temperature measurement was evaluated as a combination of the following supposedly random elements: the error involved in calibration $\pm$ 0.5°C, the error in reading the temperature $\pm$ 0.1°C and the error due to controlling accuracy $\pm$ 1°C. Thus, the resulting overall error was considered to be $\pm$ 1.4°C.

The procedure described was first tested on the binary solution Zn-Fe, and having obtained a result in agreement with the accepted value[46], one further point on the liquidus line in the ternary was measured.

4.2.2 Equilibrium Experiments Between Fe_nAl_m Binary Compounds and Zinc at 450°C

To amplify our knowledge of the isotherm of the Fe-Zn-Al system at 450°C eight different equilibrium samples were set up. Every binary compound (FeAl, $FeAl_2$, Fe_2Al_5, $FeAl_3$) was equilibrated with pure zinc and with zinc containing 1.71 wt.% aluminum.

For every sample a small piece of compound (∿ 5g) was immersed in a small (∿ 20 g) zinc or aluminum-bearing zinc bath, respectively. During this procedure proper wetting of the compound by the zinc bath was assured. The sample was then cooled in water, transferred to the pyrex tube (10 mms dia.) evacuated 5 times and purged with argon and finally sealed under vacuum. The prepared capsules were positioned in a graphite holder and placed in the resistance furnace used for a previous experiment, heated to 450°C and maintained at this temperature for 800 hours. The adjusted temperature was simultaneously controlled using the previously calibrated chromel-alumel thermocouple. The maximum deviations in temperature detected during the experiment were $\pm$ 1°C.

All samples for this experiment are listed in Table IX. After 800 hours all samples were quenched in ice water, sectioned and examined metallographically and analyzed by electron probe microanalysis.

TABLE IX

Samples for Equilibrium Experiments

Sample No.	
1	FeAl equilibrated with pure Zn*
2	$FeAl_2$ equilibrated with pure Zn
3	Fe_2Al_5 equilibrated with pure Zn
4	$FeAl_3$ equilibrated with pure Zn
5	FeAl equilibrated with Zn (Al)**
6	$FeAl_2$ equilibrated with Zn(Al)
7	Fe_2Al_5 equilibrated with Zn(Al)
8	$FeAl_3$ equilibrated with Zn(Al)

* Special High Grade Zinc (99.9975 wt.%)

** Special High Grade Zinc containing 1.71 wt.% of aluminum

4.2.3 Hot Dipping Experiments

The hot dipping experiments were aimed at gathering information about the effect of aluminum, immersion time and agitation on the growth characteristics of alloy layers on iron galvanized in an aluminum-bearing zinc bath saturated with iron. The immersion times and aluminum contents in the bath ranged from 10 sec. to 30 min. and from 0.11 to 1.10 wt.%, respectively. This wide range of experimental conditions was selected with the purpose of obtaining the widest possible variations in alloy layer development to abet subsequent metallographic, X-ray and microprobe analysis.

All experimental work was carried out with 25 x 50 mm samples of Armco iron 0.3 mm thick and prepared as described in Section 4.1.1.

Five different zinc baths, prepared via the procedure described in Section 4.1.2, were melted in commercial graphite crucibles. The crucibles, situated within a steel shell, were placed in an electric pot furnace. The temperature of the zinc bath was measured with the calibrated chromel-alumel thermocouple protected by a pyrex tube, and immersed directly in the metal. The temperature was controlled to $\pm$ 2.5°C. A slotted insulating cover was used for longer immersion times (30 mins.).

An analysis of each bath was performed just prior to the dipping and after the short time dipping (10 sec, 1 min, 3 min, 10 min) was completed long-time tests (30 mins) were carried out in the baths used initially for the short period tests. For these, only the initial

chemical composition was recorded, which was of course identical to the chemical analysis after the short time dipping experiments. The iron and aluminum contents of baths used in the dipping experiments are recorded in Table X. These demonstrate that the bath compositions are not significantly altered by immersing small iron samples.

For each bath two sets of samples were produced. The first set consisted of 5 samples immersed for 10 sec, 1 min, 3 min, 10 min and 30 min without agitation. The other set was produced with samples in the presence of agitation. To maintain the initial conditions for the two sets as nearly identical as possible the shorter time dippings (10 sec, 1 min, 3 min, 10 min) were performed alternatly with and without agitation in the same bath. This bath was then divided into three smaller baths, serving to produce 30 minutes samples for both static and agitated conditions.

The agitation involved an average vertical oscillation of 0.5 in. amplitude twice per second. Prior to Zn dipping all samples were degreased in hot tetrachloride, dipped for 5 min. in hot 1:1 HCl, rinsed in water and dipped in a hot (70°C) solution of zinc ammonium chloride (300 g/l) for 3 minutes. They were then dried above a hot plate (∿ 3 min) and immersed in a freshly skimmed bath. The oxide film on the surface of the bath was skimmed again just before removing the sample. Every sample was quenched in water within two seconds of leaving the bath. After quenching, the samples were dried, marked and a strip was cut for micro-examination leaving the remaining part for X-ray analysis.

TABLE X

Iron and Aluminum Contents of Zinc Baths
Used in Dipping Experiments
(percent by weight)

	Prior to Dipping		After Dipping	
	Fe	Al	Fe	Al
Bath I	0.020	0.120	0.021	0.110
Bath II	0.026	0.153	0.027	0.150
Bath III	0.032	0.220	0.032	0.215
Bath IV	0.034	0.320	0.035	0.310
Bath V	0.077	1.100	0.080	1.050

The sections obtained were mounted, ground on emery paper and polished on Selvyt cloth impregnated with diamond powder suspended in kerosene. Extensive experimentation confirmed that the etching procedure proposed by Haughton[26] would yield satisfactory results. With minor modifications for several samples, the following etching procedure was adopted. The specimens were hand swabbed for about 5 seconds on a piece of Selvyt cloth moistened with amyl alcohol containing 3 drops of nitric acid in 50 ml. of alcohol. This removed any diamond particles entrapped on the surface and gave a very light etch. After this preliminary treatment the specimens were etched with Rowland's No. 5 etching reagent (0.075 g of picric acid, 18 ml of ethyl alcohol and 60 ml of water). This etchant very often led to staining. To remove the stains, the etching was followed by a brief swabbing on Selvyt cloth moistened with 2 percent nitric acid in amyl alcohol. Two percent nitric acid in amyl alcohol, giving a very light etch, was also used for etching the equilibrated samples.

4.3 X-ray Diffraction Analysis

The primary purpose of the X-ray analysis was to identify extremely thin alloy layers formed at the iron-zinc interface during galvanizing. The diffractometer is an ideal instrument for this purpose, particularly for direct examination of sheet material, because of the very shallow penetration of X-rays into most metals. Accordingly, surface diffraction analysis was applied to all samples produced from each bath at immersion times of 10 sec, 1 min, 3 min, 10 min, 30 min. For

comparison, using the same experimental conditions, diffraction patterns were obtained for the binary compounds $FeAl_2$, Fe_2Al_5 and $FeAl_3$. Our initial intention to obtain by the same method diffraction patterns from prepared ternary phases could not be realized due to an insufficient supply of these samples. Thus, for the latter intermetallic phases, diffraction analysis had to be achieved by the Debye-Scherer powder method, as described in Section 4.1.5.

To utilize fully the advantages offered by the surface analysis method the experimental conditions must be carefully chosen in advance since absorption effects can cause a significant distortion of the information obtained.

4.3.1 Theoretical Analysis of the Reflection Method

In analysing very thin surface deposits it is mandatory to select the experimental conditions yielding a depth of X-ray penetration comparable to the thickness of the deposits.

Let us first examine the total X-ray intensity diffracted by a flat specimen[47]. Referring to Figure 13, let us assume that the incident beam of intensity I_o (ergs/cm^2/sec), is 1 cm square in cross section, and is incident on the plate at an angle α. Consider now the energy diffracted from this beam by a layer of length ℓ and thickness dx located at depth x below the surface. Since the incident beam undergoes absorption by the specimen over the path length AB, the energy E incident per second on the layer considered is:

$$I = I_o e^{-\mu(AB)} \text{ (ergs/sec)} \tag{4.1}$$

where μ is the linear absorption coefficient of the material.
If now, a is the volume fraction of the specimen (containing crystalline particles) having the correct orientation for diffraction of the incident beam, and b is the fraction of the incident energy which is diffracted by unit volume, then the energy diffracted by the layer considered is:

$$a \cdot b \cdot \ell_e I_o e^{-\mu(AB)} dx \tag{4.2}$$

Now, this diffracted energy is also decreased by absorption by a factor of $e^{-\mu(BC)}$. Thus the energy flux per second in the diffracted beam outside the specimen is given by.

$$d I_D = a\, b\, \ell\, I_o \exp(-\mu(AB+BC)\, dx \tag{4.3}$$

Since

$$\ell = \frac{l}{\sin\alpha}, \quad AB = \frac{x}{\sin\alpha}, \quad BC = \frac{x}{\sin\beta}$$

and $\alpha = \beta = \theta$ for the diffractometer, then equation (4.3) yields:

$$dI_D = \frac{I_o\, ab}{\sin\theta}\, e^{-2\mu x/\sin\theta}\, dx \tag{4.4}$$

The total diffracted intensity is then obtained by integrating over an infinitely thick specimen:

$$I_D = \int_{x=0}^{x=\infty} dID = \frac{I_o ab}{2\mu} \qquad (4.5)$$

Here, I_o, b, μ are constant for all reflections (i.e., independent of θ) and a may be regarded to a good approximation as constant as well.

Thus, we may conclude that a flat specimen making equal angles with the incident and diffracted beams, not only produces focusing but makes the absorption factor $1/2\mu$ independent of θ. This lack of dependence of diffracted intensity on θ is due to a balancing of two opposing effects. At θ small, a large irradiated area and small penetration depth are combined, whereas at θ large, a small irradiated area is penetrated to a greater depth.

Having estimated the total diffracted intensity, we must pose a question: to what depth in the specimen does the information obtained relate? The total integrated intensity is given in terms of constants a, b, I_o (equation 4.5). However, these constants cancel if the intensity diffracted by the layer considered is expressed as a function of the total integrated intensity diffracted by a specimen of infinite thickness. Then for the diffractometer ($\alpha = \beta = \theta$):

$$G_x = \int_{x=0}^{x=x} dI_D \Big/ \int_{x=0}^{x=\infty} dI_D = (1-e^{-2\mu x/\sin\theta}) \qquad (4.6)$$

This expression allows one to calculate the fraction G_x of the total

diffracted intensity which is contributed by a surface layer of depth x. If we now arbitrarily decide that a contribution from this surface layer of, let us say, 90% of the total is sufficient, so that the contribution from the material below that layer can be ignored, then x is defined as the effective depth of penetration. Thus we know that the information recorded on the diffraction pattern (or more accurately, 90% of the information) refers to the layer of the depth x, and not to the material below it.

Equation (4.6) shows that the effective depth of penetration decreases as θ decreases and therefore varies from one diffraction line to another. For ease of calculation we may write:

$$\frac{2\mu x}{\sin\theta} = \ln\left(\frac{1}{1-G_x}\right) = K_x \qquad (4.7)$$

and

$$x = \frac{K_x \sin\theta}{2\mu} \qquad (4.8)$$

Values of K_x corresponding to various assumed values of G_x are readily calculated and are given as follows:

G_x	0.50	0.75	0.90	0.95	0.99	0.999
K_x	0.69	1.39	2.30	3.00	4.61	6.91

Thus the depth of penetration at constant K_x can in principle be decreased by working at low angles θ with radiation that is highly absorbed.

4.3.2 The X-ray Diffractometer

A diffractometer directly records X-ray intensities diffracted by a powder or solid specimen. The usual design of instrument (Figure 13) uses a planar specimen in a reflecting position. The specimen is set with its surface on the diffractometer rotation axis so that the surface normal bisects the angle between the incident X-ray beam and the beam diffracted to the detector. To maintain this parafocussing geometry the specimen is geared to rotate at one half the angular velocity of the detector. The centers of the source and the detector slit are set equidistant from the spectrometer rotation axis. The specimen surface is then tangent to a circle, passing through the source and detector centers.

For exact focussing the specimen would have to have a curvature in the equatorial plane. But the curvature is approximated by the tangent surface of the specimen, and the diffracted beam is concentrated in a small angular range about the focus.

Beam divergence normal to the equatorial plane is limited by use of Soller slits placed in the incident and diffracted beams. These are parallel sheets of metal foil narrowly separated and set parallel to the equatorial plane.

The angular divergence of the incident and diffracted beams in the equatorial plane is limited by the divergence and receiving slits, respectively. The permitted diffracted-beam divergence is generally greater than the incident-beam divergence, so that the diffracting volume of the specimen is controlled by the divergence of the incident beam. The angular width subtended by the focal spot at the specimen affects the diffraction line width, particularly at low θ values. The pulse

output of the detector is registered by a scaling unit, and in most instruments a ratemeter and chart recorder record the intensity variation, which can be measured with the detector, in a fixed position or by 2θ scan at a selected angular velocity.

Instrumental aberrations may produce displacement or broadening of the diffraction lines. The effect of most instrumental aberrations is to displace the scattering distribution without appreciable broadening. The displacement of the diffraction line due to instrumental aberrations in the equatorial plane has been derived by Wilson[49] as:

$$\phi_H = -\phi_S\,(1-r_S/R_o) - 2(r_e/R_o)\cos\theta + (\phi^2/\sigma)\cot\theta + X\cot\theta \qquad (4.9)$$

where ϕ_S is the angle between the incident axis ($2\theta = 0$) and the ray from the source center to the rotation axis, ϕ is the angular divergence of the incident beam, r_e is the displacement of the specimen surface plane from the rotation axis, R_o is the diffractometer radius, r_S is the displacement of the source center from the focussing circle in the incident direction, and X is a parameter due to cross products of instrumental aberrations.

Thus the zero alignment error:

$$\phi_S' = \phi_S\,(1-r_S/R_o) \qquad (4.10)$$

and the eccentricity error

$$2(r_e/R_o)\cos\theta \qquad (4.11)$$

are of the first order and are the principal sources of error in diffraction measurement.

The broadening of the diffraction lines is primarily due to the source intensity distribution.

4.3.3 Selection of Experimental Conditions for X-Ray Analysis

In selecting the experimental conditions for X-ray analysis, minimal peak shift was judged to be a governing criterion. This was in principle attainable via limitation of the depth of penetration as well as selection of appropriate instrumental parameters.

The relatively large unit cells of iron-aluminum compounds and the very closely spaced lines of their diffraction patterns (ASTM X-Ray Powder Data File and Horstmann[27]), call for the use of X-ray radiation with relatively longer wavelengths to gain well-separated diffraction lines. Such a desirable choice of wavelength may not be acceptable due to other requirements.

Referring to equation (4.8):

$$x = \frac{K_x \sin\theta}{2\mu}$$

we see that a small depth of penetration x, and consequently a small peak shift, can be attained only by working at small angles θ with radiation which is highly absorbed by the layer being examined. To estimate the approximate depth of penetration for the X-radiation available (Fe and Cu tubes) the average composition of the protective layer was tentatively assumed to be 37 at.% Fe, 60 at.% Al, 3 at.% Zn. Then assuming that 75% of the information recorded on a diffraction pattern pertains to this layer (i.e., $G_x = 0.75$, $K_x = 1.39$), the effective depth of penetration x was calculated for CuK_α and FeK_α radiations. Results of this calculation are shown as a function of angle θ in Table XI.

Thus, in view of the fact that thickness of the inhibiting layer was estimated by Borzillo and Hahn[30] to be of the order of one micron, the CuK_α radiation was selected and the angle θ was varied within a range 5 - 25 degrees (2θ, 10 to 50 degrees). By selection of this radiation and range of angles, the peak shift was minimized, but at the expense of line spacing and peak-to-background ratio. To correct for this latter shortfall in conditions the medium defining slit (1°) and medium detector (receiving) slit (0.035° or 0.1 mm) and a low scanning velocity ($1/2^\circ$/min) were selected. The above parameters then determined the time constant RC through the following relations[50]:

$$\text{time width of slit} = 60(\nu/\omega)[\text{sec}] \qquad (4.12)$$

where ν - detector slit width in degrees

ω - scanning velocity in degrees per minute

$$RC \leq 1/2 \text{ time width of slit} \qquad (4.13)$$

TABLE XI

Approximate Effective Depths of Penetration
For CuK_α and FeK_α Radiation

Angle θ (deg.)	Effective depth of penetration (microns)	
	CuK_α radiation λ=1.542 Å	FeK_α radiation λ=1.937 Å
5	0.581	1.568
10	1.16	3.12
20	2.29	6.15
30	3.35	9.00

For our parameters the time width of slit was 4.2 sec. Thus we selected the time constant RC = 1 sec, which assured satisfactory resolution and prevented the shift of peaks in the scanning direction from increasing the line asymmetry and lowering the peak intensities.

The X-ray analysis was performed on a Norelco type diffractometer at the Research Laboratories of the Steel Company of Canada.

The X-ray analysis was applied to all samples produced under agitation because they all exhibited sufficiently thick inhibiting layers. The samples were 30 mm long and 25 mm wide. Prior to X-ray examination the area of every specimen was measured. The zinc overlay was removed in a 5% sulfuric acid solution with 2g/l of sodium arsenite. The residual arsenic film was then removed by a flash immersion in cold concentrated nitric acid and rinsed in water. The specimens were weighed to the nearest 0.002 mg on a microbalance. After X-ray analysis, the aluminum-rich alloy layer was stripped off in a hot solution of 20% sodium hydroxide. The residual film was then removed by a flash immersion in cold concentrated hydrochloric acid. The specimens were again weighed on the microbalance.

The powder samples were prepared by grinding the compounds to 325 mesh and the powder obtained was mechanically mixed for 2 hours. In preparing the samples for the diffractometer the powder was firmly pressed into the holder to secure a stable flat surface, thus minimizing a peak shift due to poor surface but at the expense of a possible relative intensity change due to preferred orientation of crystals in the powder compact.

4.4 Electron Probe Microanalysis

In electron probe microanalysis the concentration of a given element A in a sample can in principle be deduced from a comparison between the intensity I_A of an important characteristic line of element A emitted by the sample under given conditions of electron bombardment and the intensity I(A) of the same characteristic radiation when emitted by the pure element A under the same electron bombardment conditions. In practice, three different corrections must be made to the measured raw intensities. These account for atomic number differences, for mass absorption, and for fluorescence effects.

There are two methods of dealing with the raw data. One is to interpolate the experimental data for the unknown between that determined for adjacent known alloy standards. This procedure is excellent for binary systems but is often inconvenient for ternary systems because of the large number of alloy standards required. The second method is to theoretically correct the measured intensities on the basis of intensity data obtained for the pure components of the ternary system.

We shall not deal here with detailed correction calculations, since these have been treated in great depth by many authors[51,57]. Our attention will be directed solely toward the problems arising from an application of electron probe microanalysis to the intermetallic phases of the ternary system Fe-Zn-Al.

Caloni and Ferrari[58] and Palmer and Thresh[59] have reported iron profiles for the phases formed on commercial galvanized coatings. The latter authors have reported measurements for Ni, Ti, Mn and V as well.

The elements involved in these examinations, being reasonably close in the periodic table, were amenable to application of standard correction procedures. Cameron and Ormay[29] through microanalysis have recorded the presence of a ternary compound in aluminum-bearing coatings. Their results, however, were not corrected and the percentages do not add to 100%. These investigators found the iron content of the binary phases formed on iron to be in a good accord with values given by the equilibrium diagram.

In our work we have chosen to concentrate on the phases formed in equilibrium samples. The phases expected were either iron-aluminum-rich, with smaller additions of zinc, or iron-zinc-rich with smaller additions of aluminum.

Philibert[60], in examining Fe-Al binary alloys (up to 10 wt.% Al) by microanalysis found good agreement between the results obtained and chemical analysis at an acceleration voltage E_o = 10 keV. For E_o > 13 keV the correction calculation becomes meaningless due to the excessive absorption of characteristic aluminum radiation by Fe.

Our extensive preliminary measurements carried out at low acceleration voltages (10, 11, 12 keV) on Fe-Al, Fe-Zn binary standards and Fe-Zn-Al ternary standards showed great discrepancies between the chemical analysis and the conventional corrected microprobe results. We concluded that it was impractical to measure aluminum contents in our ternary alloys, even with low acceleration voltages, since the zinc is even more absorbant than the iron. Furthermore, the resulting low intensities associated with low voltages and the high absorption of Zn radiation by iron lead to poor statistics on the zinc readings. Our experimental procedure was therefore designed to select an optimal acceleration voltage with respect to the iron and zinc determination which would enable measurement of their

content to an accuracy sufficient to allow an aluminum determination by difference. As part of this procedure all prepared binary phases (Fe-Al, Fe-Zn) and the two significant ternary phases were examined by electronprobe microanalysis at the accelerating voltages 14, 16, 18, 20 and 22 keV. In all these measurements the pure elements were used as standards. The raw data were first corrected for background and instrumental dead time, then the atomic number, absorption and fluorescence corrections were applied to the raw intensities to yield the composition in weight percent. For all correction calculations the relationships and data given in reference (61) were adopted. The calculations were carried out by computor using the iterative program available at McMaster University.

The measured compositions obtained were then compared with the results of chemical analysis and the acceleration voltage giving the best results for Fe and Zn was selected for examination of the equilibrium samples. The aluminum content was then obtained by difference. The results of these preliminary measurements are given in Appendix A. As can be seen from the summary given in Table XII, an acceleration voltage of 18 keV yielded results closest to the actual composition of the examined phases. This voltage was therefore selected as the base for further analysis. It is particularly gratifying that the 18 keV optimization gives an excellent correlation between the chemical and microprobe results over a very wide dispersion of binary phases at the boundaries of the ternary system. This gives us strong confidence that the conventional correction methodology for the 18 keV condition is also a very good interpolation formula for points within the isotherm. We anticipate, from the errors in column 18keV Table XII, that the experimental measurements quoted in the following will

TABLE XII

Summary of Preliminary Microanalysis Results
(* Values Obtained by a Difference)

Compound	Chemical Analysis (wt.%)	Accelerating Voltage (keV)				
		14	16	18	20	22
FeAl	Fe - 66.57 Al - 33.24	67.78 32.22*	67.80 32.20*	65.90(-1.0%) 34.10*(+2.5%)	64.20 35.80*	65.10 34.90*
$FeAl_2$	Fe - 51.19 Al - 49.99	53.60 46.40*	52.10 47.90*	50.20(+0.0% 49.80*(+0.02%)	49.00 51.00*	46.70 53.30*
Fe_2Al_5	Fe - 45.12 Al - 55.55	48.25 51.75*	51.75*	47.10(+5%) 52.90*(-4.5%)	49.00 51.00*	44.50 55.50*
$FeAl_3$	Fe - 41.84 Al - 57.58	42.00 58.00*	42.40 57.60*	41.70(-0.35%) 58.30*(+1.20%)	43.70 56.30*	40.50 59.50*
Zeta Phase	Fe - 5.99 Zn - 94.01		6.40 93.50	6.30(+5.0%) 93.50(-5.0%)	6.50 93.50	6.20 94.20
Delta$_1$ phase	Fe - 8.92 Zn - 91.08		9.65 91.40	9.30(+4.0%) 88.50(-2.8%)	10.10 91.00	9.80 92.70
Ternary phase (2)	Fe - 8.60 Al - 3.93 An - 87.47		8.20 2.80* 89.00	8.20(-4.5%) 4.00*(+1.8%) 87.90(+0.5%)	8.60 0.10* 91.30	8.40 0.60* 91.00
Ternary phase (5)	Fe - 42.82 Al - 44.60 Zn - 12.58			41.87(-2.3%) 45.68*(+2.2%) 12.45(-1.0%)		

be to an accuracy of better than 5% of the amounts of the two major constituents present and to 5% of the zinc (but not the Al) present when it is the minor constituent.

The Acton-Cameca electron probe microanalyser used for this study allowed us to monitor all three elements at once. Prior to microanalysis the specimens were prepared metallographically and coated in an evaporator with a carbon film of about 50 Å thick to assure good electrical contact between all samples and the grounding electrode.

CHAPTER V

EXPERIMENTAL RESULTS

The results of the experiments described in the previous chapter are presented in this section.

5.1 Equilibrium Experiments

The equilibration experiments were carried out to provide data on the 450°C isotherm of the Fe-Zn-Al system. The results of our experiment to determine solubility points on the liquidus curve in the zinc-rich corner of the ternary isotherm are summarized in Table XIII.

The results for the binary system are in good agreement with currently reported solubility data at 450°C[46]. This fact permitted us to regard the data obtained for the ternary system as reliable and that a new point on the liquidus curve has been established at the co-ordinate

Fe	Al
0.030 wt.% ± 0.0005	0.21 wt.% ± 0.005

We hereafter take the solubility curve to be approximated by a line connecting the experimental points for the entire required range of aluminum content in the zinc baths used in the galvanizing studies. In the second part of the equilibrium experiments the Fe-Al binary compounds were equilibrated with pure zinc or aluminum-bearing zinc, respec-

TABLE XIII

The Results of the Liquidus Line Experiments

	Time of Experiment	Fe(wt.%)		Time of Experiment	Fe(wt.%)	Al(wt.%)
Binary			Ternary			
Approached from $T < 450^{o}C$	21 days 30 days	0.0285 0.0288	Approached from $T < 450^{o}C$	15 days 22 days	0.029 0.029	0.21 0.21
Binary			Ternary			
Approached from $T > 450^{o}C$	20 days 29 days	0.0295 0.0292	Approached from $T > 450^{o}C$	18 days 26 days	0.030 0.031	0.21 0.22

tively, at 450°C for 800 hrs. After quenching, the samples were sectioned and prepared for metallographic observation. (Etching agent - 5 drops of HNO_3 in 50 ml of amyl alcohol). Prior to microanalysis the etching was removed.

Equilibrium Between FeAl and Zn

A typical microstructure of this test sample is shown in Figure 14. Near the original Fe-Al-Zn interface there is a continuous layer of a phase (later identified as zinc-bearing Fe_2Al_5) having a slightly lighter shade than FeAl phase at the bottom. Moving upward we find a three-phase region consisting of large columnar grains of δ_1 phase (see below) containing a fine dispersion of zinc-bearing Fe_2Al_5 and white liquid zinc streams. Out of the metallographic field at the top this three-phase region merges into the single liquid zinc phase.

All the phases present were analysed with the electron microprobe. In all these measurements the electron probe spot was always located within 5 to 10 microns of the phase interfaces. No attempt was made to measure concentration gradients within any one phase. All microanalysis data and results pertaining to these experiments are given in Appendix B. The results obtained for the above sample are presented in Table B.I.

Equilibrium Between FeAl and Zn(Al)

The microstructure of this specimen was the same as the previous one near the FeAl terminus. However, the fine dispersion of the blue-grey phase (Fe_2Al_5) extended through the large columnar phase (δ_1) into the liquid zinc matrix surrounding the immersed sample as indicated in Figure 15. At the outside interface of the large grains the three-phase equilibrium could be most easily identified. As can be seen this three-phase equilibrium is formed between the white zinc, the grey large-grained phase and the small grains of blue-grey phase. The microanalysis data and the results are given in Table B.2.

Equilibrium of $FeAl_2$ with Zn

The microstructure of this specimen consisted basically of a three-phase equilibrium throughout, as shown in Figure 16. Within the zinc matrix (white) there are regularly shaped grey grains (δ_1) along with a dark phase (Fe_2Al_5) quite frequently forming triple-points of precise three-phase equilibrium. The small particles of the dark phase are also to be found within the grains of the grey phase. In the microanalysis each phase was examined in two phase contact as well as at triple point equilibrium. The results obtained are presented in Table B.3.

Equilibrium of $FeAl_2$ with Zn(Al)

The microstructure of this sample, in contrast to the previous one and although strongly attacked by the zinc, still contained remnants of the original $FeAl_2$ phase. The general microstructure consisted of the dark grey phase imbedded in a matrix of liquid zinc, as shown in Figure 17. The data and results of the microanalysis are given in Table B.4.

Equilibrium Between Fe_2Al_5 and Zn

The microstructure of this specimen was relatively simple, as illustrated in Figure 18. The original Fe_2Al_5 phase was in equilibrium with zinc as well as with large grains of the grey phase. The latter phase also equilibrates with zinc. In Figure 18 a three-phase equilibrium can be clearly identified between the described phases. This triple point was analysed by the electron microprobe and the results obtained are given in Table B.5.

Equilibrium Between Fe_2Al_5 and Zn(Al)

A typical feature of the microstructure of this specimen was that all remnants of the original Fe_2Al_5 phase had disappeared. The Fe_2Al_5 phase was apparently rapidly attacked by the aluminum-bearing zinc and the microstructure was formed exclusively of irregular grains of dark phase embedded in a zinc matrix. Figure 19 shows a typical microstructure of

this specimen. The blue-grey phase was analysed with the electron probe with results given in Table B.6.

Equilibrium Between $FeAl_3$ and Zn

The interface of this specimen was heavily damaged due to the extreme brittleness of $FeAl_3$ so no consistent metallographic examination of this specimen was possible. However at a few spots where the interface seems to have been maintained, a distinguishable two-phase zone separated by two single phase zones was apparent. No microanalysis could be carried out.

Equilibrium Between $FeAl_3$ and Zn(Al)

The interface of this specimen was less subject to cracking than in the previous case which allowed significant observations of the $FeAl_3$ attack by zinc. This attack resulted in the formation of a two-phase zone separating two single-phase zones as indicated in Figure 20. Microanalysis was carried out on the blue-grey phase at its interface with zinc. The results are given in Table B.7.

5.2 Metallographic Examination of Galvanized Specimens

The objective of the galvanizing experiments was as stated before, to generate the widest possible variations in the development of

intermetallic phases at the iron-zinc interface. The metallographic examination aimed to detect the sequence in the development of observable intermetallic phases. This information was to be compared with X-ray analysis, particularly useful at early stages of the growth process, and microanalysis of ternary compounds which reach a satisfactory thickness at the latest stages of the process (i.e., longer times, higher aluminum contents).

To illustrate the relationship between aluminum content and growth characteristics of the intermetallic phases, their metallographic development will be discussed for each given time of immersion as a function of the aluminum content of the zinc bath.* (All metallographic observations were carried out at a magnification of 1140X).

(a) Immersion Time 10 Sec.

Bath 1: The major part of the interface between iron and zinc is formed by an even line without any intermediate phase apparent. At a few spots there are very small regions with a phase penetrating slightly below the interface. This phase has a grey, spongy appearance. Small nuclei of another phase were observed within this phase, and growing from the iron interface. At several spots along the unattacked interface very small crystals of regular shape were observed growing from the iron.

The agitated sample exhibited the same character. However,

* See Table X

the appearance of small crystals formed along the unattacked interface was more frequent. In general they were difficult to detect because they are coloured nearly the same shade as iron.

Bath II: The major part of the interface was found to be even and without any intermediate phases present. The regions of attack on the iron by a spongy grey phase having a burst-like shape were less frequent than for the previous bath. The number of regular crystals was again found to be very limited. Some of them appeared to be separated from the iron, without any attack below them.

The stirred sample exhibited the same basic characteristics, but the outbursts of spongy grey phase were less frequent than in the bath without stirring. The tendency of the regular crystals to flake off was more pronounced and some appeared to float in the Zn overlay.

Bath III: The entire interface was found to have an even appearence with no intermediate phases apparent, and no outbursts of the spongy grey phase. At several spots the line of the interface was observed to be slightly uneven and here again regular crystals growing directly from the iron were identified. The agitated sample had the same features, but the regular crystals were again more often separated from the interface while remaining closely attached to the interface. The detached crystals were easier to identify because of this light blue-grey shade.

Bath IV: The situation was identical with the sample from the previous bath for both the static and agitated specimen.

Bath V: These samples exhibited the same structure as those from the previous bath. The line of the interface was apparent with a few small regular crystals growing from the iron.

(b) Immersion Time 1 Minute

Bath I: The interface had a more uneven appearance but no attack was observed along the major part of the interface. The outbursts of spongy grey phase were more pronounced and they contained another darker phase within. The nuclei of this phase had a darker shade and grew from the interface with iron. The agitated sample exhibited the same principal features as the static one.

Bath II: The structure was very similar to that in the previous sample. The outbursts of spongy grey phase were less extensive than for Bath I. The regions of growth of regular crystals were more extensive with better developed crystals than in Bath I. The stirred sample possessed the same structure but the outbursts of spongy grey phase were less frequent than for the bath without stirring.

All the characteristics of intermetallic phase development thus far described can be observed in Figure 21. Going from the right side

we can see an uneven interface due apparently to the growth of a phase region of regular crystals (1), followed by a region of attack by a spongy grey phase (2) penetrating below the unattacked interface. At the interface of this phase with iron the nucleus of another phase growing from iron (3) is observed. The original even interface follows with a few regular crystals nearly separated but still closely attached to the original interface. The section ends on the left with an outburst of a spongy phase.

Bath III: The interface again had an even appearance. No outbursts of grey spongy phase were detected. The regions of growth of the blue-grey phase were still limited in number but when present were larger and more easily detectable, often being detached from the interface. The agitated sample exhibited similar characteristics. However, the regions of the blue-grey phase were found to be more extensive.

Bath IV: The static as well as agitated sample exhibited the same features as the samples of Bath III.

Bath V: The characteristic feature of both samples, as compared to those from Bath IV, was the appearance of the interface. A continuous uneven layer having a clear blue-grey shade covered nearly the entire interface.

(c) Immersion Time 3 Minutes

Bath I: The structure exhibited the same basic features as that produced by an immersion time of 1 minute in Bath I. However, the grey spongy phase formed a continuous layer covering the interface nearly completely. The regions with blue-grey phase crystals were very limited in occurrence as were regions of the interface without any intermediate phases present. The agitated sample exhibited the same features as the static sample, but the regions with no attack were more extensive.

Bath II: This sample had a similar structure as that from Bath I, but the outbursts of grey spongy phase were less extensive and clearly exhibited a layer of another phase growing from the iron interface. Regions with the blue-grey phase were more extensive than for Bath I. The crystals were better developed, showing a strong tendency to peel off the iron.

The same situation as for the static sample existed, but the blue-grey crystals growing from the iron interface had a more pronounced blue appearance and were thus more readily distinguishable from the iron.

These latter structures are illustrated in Figure 22. Going from the right there is the even unattacked interface between iron and zinc with several small blue-grey crystals growing from iron (I). This region

is followed by an outburst of the grey spongy phase (2) penetrating into the iron and exhibiting a layer of another darker phase (3), formed at the interface with iron.

Bath III: The major part of the interface had an even appearance without any intermediate phase and no attack apparent. At several spots the growth of a blue-grey phase was detected having a very uneven thickness. At some of these spots the nuclei of a dark grey phase were observed. This phase, in contrast to that in Figure 22, did not exhibit any nuclei of another phase at the iron interface. It was always found to be formed adjacent to the layer of the blue-grey phase. The agitated sample had the same basic features as the static one but with less frequent occurrence of nuclei of the dark grey phase. The regions of growth of the blue-grey phase were found to be more extensive than for the static sample, apparently at the expense of interface regions without any observable intermediate phase. This stage is illustrated in Figure 23. Towards the right the even line of the original interface is followed by an outburst of blue-grey phase and then by a nucleus of a compact grey phase penetrating into the iron.

Bath IV: There was no grey attacking phase detected within this sample. The amount of even interface without observable intermediate phases was still quite extensive, but the regions of the blue-grey layer were more frequent than for Bath III. This layer was

of highly variable thickness extending deeper into the iron when growth towards the zinc occurred. The agitated sample had nearly the entire interface covered by an uneven layer of blue-grey phase with few remnants of the original even interface. Figure 24 illustrates the characteristic difference between an unattacked interface and an interface with a growing blue-grey phase (I).

Bath V: The compact layer of blue-grey phase formed along the entire interface. Also, regions of detached blue-grey crystals accompany the extensive growth of this layer. The agitated sample exhibited identical characteristics.

(d) Immersion Time 10 Minutes

Bath I: The entire interface of this sample was covered with a grey spongy phase of varying thickness. Extensive regions of this phase were of excessive thickness and had very unstable interfaces with both the zinc and the mother phase layer at the iron interface. Small regions of the interface were covered with a very thin grey phase, usually accompanied by regular crystals on the top. The agitated sample exhibited a similar structure. However, at several locations regions without any attack were maintained.

Bath II: The static and agitated samples of this bath exhibited the same structural features as the static and agitated samples, respec-

tively, produced from Bath I.

Bath III: This sample developed a thick continuous layer of dark-grey phase along the entire interface. No other phase was detected within this phase along the iron interface. Blue-grey phase particles were observed being attacked at the unstable interface of this phase with the zinc.

The agitated sample, on the other hand, still exhibited extensive regions of the blue-grey phase layer. However, there were also frequent regions of dark grey single phase. This phase apparently grew at the expense of the blue-grey phase, actually separating this layer from iron as illustrated at Points (I) in Figures 25 and 26.

Bath IV: The entire interface of this sample was covered with a rather loose layer of the blue-grey phase. Frequently, this layer spontaneously peeled off (see Figure 27) perhaps via the volume expansion associated with the undergrowth of the dark grey phase (as previously illustrated in Figure 26). At the regions where the peeling took place a formation of the dark grey phase (I) penetrating into iron was sometimes detected at the freshly formed interface. The agitated sample exhibited only a continuous layer of blue-grey phase which had spontaneously peeled off. The number of grey phase nuclei was much reduced as compared to the static sample.

Bath V: This sample exhibited only a layer of the blue-grey phase. The layer was mainly even and compact but at several locations excessive growth towards the zinc was detected. The latter feature is illustrated in Figure 28. The agitated specimen had the same structure as the static one.

(e) Immersion Time 30 Minutes

The phases produced for this time in Baths I, II, and III exhibited the characteristic features of Figure 29. Along the entire interface a continuous layer of grey phase was observed near the base metal with crystals of another phase lying above it (I). The former phase lying between the crystals (I) exhibited an unstable interface when in contact with zinc. This feature is illustrated in Figure 30 and shows the top part of the structure (as indicated by dashed line in Figure 29).

Bath IV: The major part of the interface was covered by a moderately thick grey phase. However, there were still regions with only the layer of blue-grey phase present, which occasionally flaked away. The agitated sample had the interface covered mainly with a continuous layer of the blue-grey phase. However, frequent outbursts of dark grey phase were readily observable, as illustrated in Figure 31.

Bath V: Both samples from this bath exhibited only the continuous layer of the blue-grey phase having a loose appearance throughout. No other phase was detected.

The detailed metallographic examination of galvanized samples described above enabled us to observe the nucleation and growth of a thus-far unidentified blue-grey intermetallic phase. At early stages of the process this layer was not thick enough to permit utilization of electron probe microanalysis, but with increasing aluminum contents and time, its growth finally yielded a sufficient thickness, as demonstrated at location (2) in Figure 27. The microanalysis of the blue-grey intermetallic phase corresponding to Figure 27 yielded the results given in Table XIV.

Along with the metallography this result served to uniquely identify the blue-grey phase as zinc-bearing Fe_2Al_5 as discussed in Section 6. The dark-grey phase and the grey spongy phase, which often appeared, were metallographically identified as δ_1 and ξ phases, as discussed in Section 6.

5.3 X-Ray Diffraction Analysis of Galvanized Samples

Since the galvanized samples produced with agitation generally exhibited thicker and more evenly developed regions or layers of the blue-grey intermetallic phase, all these samples were subjected to diffraction analysis. For comparison, diffraction patterns were obtained for three powdered binary phases using identical test conditions as described in Section 4.3.3. All the results of the diffraction analysis are given in Appendix C, Table C.1 to C.27.

TABLE XIV

Microanalysis Data and Results for Blue-Grey Intermetallic Phase Shown in Figure 27

	Raw Intensity of Pure Elements (counts/sec)		
	Al	Fe	Zn
Initial	15893	32790	10178
Final	15571	32496	9874

Phase Examined	Raw Intensity (counts/sec)			Composition (wt.%)		
	Al	Fe	Zn	Al	Fe	Zn
Blue-grey intermetallic phase	1184	13483	1369	19.61	42.16	14.67
	1200	13274	1357	19.73	41.38	14.54
	1191	13198	1253	19.68	41.26	13.61
	1173	13352	1190	19.55	41.82	13.09
	1214	13471	1312	19.82	42.12	14.15
Av.				44.25*	41.75	14.00

* Al content obtained by difference

CHAPTER VI

DISCUSSION

The experimental results will be discussed mainly from the point-of-view of the inhibiting mechanism causing variations in the growth kinetics of the intermediate phases on iron in aluminum-bearing zinc baths at 450°C. First, the results of the constitutional experiments will be related to the X-ray analysis and metallographic observations of galvanized specimens to provide a base for discussion of the inhibiting mechanism.

6.1 Constitutional Experiments

The constitutional experiments were undertaken to gain basic data pertaining to the 450°C isotherm of the Fe-Zn-Al system.

6.1.1 The Liquidus Line in the Zinc-Rich Corner

Recognition of the effect of iron in the bath on inhibiting action has developed gradually. Bablit[22,23] investigated the inhibiting effect of aluminum covering a wide range of temperatures and aluminum contents, mainly under conditions of iron saturation defined by dross formation. Hughes[24] examined the effect of aluminum additions up to 1.5 percent by weight at various temperatures. The zinc baths were prepared from pure zinc without further specification of iron content. Haughton[26] first drew attention to the role of iron in conjunction with

the aluminum additions to the zinc bath. It was demonstrated that an increasing amount of iron in an aluminum-bearing zinc bath favours more rapid growth rates of the inhibiting layer. Horstmann[27,28] and Cameron[29] also considered the effect of iron in their investigations. However, their iron-saturated bath was defined either from the iron-zinc binary diagram or through dross-saturation. Borzillo and Hahn[30], in examining growth of the inhibiting aluminum-rich alloy layer, worked with low and medium iron contents referring again to the solubility in iron-zinc binary systems. The inhibiting aluminum-rich alloy layer was found to grow parabolically with immersion time, the rate of its growth being affected by temperature and the aluminum:iron ratio of the bath. At temperatures of 450°C and 470°C. higher ratios favoured slower growth rates of this layer.

In the present work we undertook to produce the galvanized samples in a zinc bath saturated with iron. This condition, besides approaching closely to the practical situation, also eliminates the iron content as a free variable. At the same time, a relatively thick aluminum-rich alloy layer, more suitable for subsequent analysis, is formed. The saturation conditions are defined by the ternary phase diagram.

Cameron and Ormay[24] in their proposal of a tentative Fe-Zn-Al isotherm at 450°C suggested that increasing the aluminum content decreases the iron solubility in zinc, as illustrated in Figure 8. To verify this proposition the experiments of Section 4.2.1 were adopted, and the methodology was checked first on the binary Fe-Zn system. This yielded the saturation concentration of iron in zinc as 0.029 wt.%, in good agreement with published data. A second point on the ternary liquidus line was determined as an average from two long time experiments wherein the

equilibrium point was approached from below and above saturation. The two results obtained (Table XIII) show good consistancy, suggesting the average point on the liquidus line to be a reliable one. This point has the co-ordinate 0.030 ± 0.0005 wt.% at 0.21 ± 0.005 wt.% Al.

The result indicates that, contrary to the claim of Cameron and Ormay, the iron solubility in zinc at 450°C is constant, or slightly increasing with increasing aluminum content. For subsequent preparation of zinc baths we approximated the iron solubility curve by a straight line whose slope is defined by the two measured points.

Figure 32 shows our modification of the zinc corner of the 450°C isotherm of the Fe-Zn-Al system. The limiting tie-lines for the ζ phase are drawn to agree with Cameron and Ormay's point at 0.07 wt.% Al on the iron solubility line. The corresponding point for the δ_1 phase has been displaced towards 0.11 wt.% Al as suggested by our own results. Referring to our linearized iron solubility we may conclude that the zinc Bath I to IV used in the dipping experiments (see Table X) were by design very close to iron saturation. For Bath V we failed to achieve a controlled saturation point so we must designate it, with other authors, as dross-saturated.

6.1.2 Constitutional Experiments on the Interactions of Fe_nAl_m Binary Compounds and Zinc at 450°C

The metallographic examination and electron probe microanalysis of samples containing phase equilibria between Fe_nAl_m compounds and liquid zinc have established some important constitutional relations on the 450°C

isotherm of the Fe-Zn-Al system. As previously indicated electron probe microanalysis of these samples presented a problem due to the excessive absorption of the aluminum characteristic radiation. Nonetheless, preliminary tests at different acceleration voltages summarized in Table XII enabled us to select that acceleration voltage (18 keV) which yielded theoretically corrected compositions close to the chemical compositions of the prepared compounds.

Referring to Table XII we see that for the iron content there was an error of $\pm$ 5 percent of the amount present. The upper and lower limits of the error are associated with the iron content of the binary phase Fe_2Al_5 and the aluminum bearing δ_1 phase, respectively. The results obtained for the binary phases ξ and δ_1 were also accompanied by errors approaching 5%.

The measurements on phases FeAl, $FeAl_2$, $FeAl_3$ and zinc bearing Fe_2Al_5 yielded results within a standard experimental error $\pm$ 2.2 percent. From these observations we have estimated that for the analysis of ternary unknowns the accuracy will be better than 5% of the amounts of the two major constituents present and 5% of the Zn present when it is the minor constituent. When Al is the minor constituent its error will obviously be much higher. The microstructure formed in the sample Fe-Al-Zn, as illustrated in Figure 14, identifies two phase equilibria between the phase pairs FeAl-Fe_2Al_5, Fe_2Al_5-δ_1 and δ_1-Zn, and three phase equilibria between the triplets FeAl-Fe_2Al_5-δ_1 and Fe_2Al_5-δ_1-Zn. The dispersion in the latter cases were such as to prevent microprobe analysis of appropriate triple points. However, it is clear from the micrograph that the two two-phase pairs FeAl-Fe_2Al_5 and Fe_2Al_5-δ_1 must rather closely define the first of the

three-phase triangles. The results of electron probe microanalysis given in Table B.1 as compared with the compositions of the prepared standards permitted us to identify the phases present as specified above.

The microstructure of the sample FeAl-Zn(Al) exhibited the same types of two-phase equilibrium as the previous sample. In addition, a measureable three-phase equilibrium was obtained as illustrated in Figure 15. The results of microprobe analysis of a corresponding triple point (Table B.2) provide data on the three-phase triangle between Zn, aluminum-bearing δ_1 and zinc-bearing Fe_2Al_5 phases. The composition in the zinc corner was not determined since the adopted method did not yield reliable results for such low concentrations of iron and aluminum.

The three-phase equilibrium between the above-mentioned phases was also constituted in the samples $FeAl_2$-Zn and Fe_2Al_5-Zn, as illustrated in Figures 16 and 18, respectively. (For the microprobe results see Tables B.3 and B.5).

The heat treatment of the sample $FeAl_2$-Zn led to complete transformation of the original $FeAl_2$ to the three phase mixture (see Figure 16), whereas remnants of the $FeAl_2$ phase were detected in the structure of the sample $FeAl_2$-Zn(Al), and the major part of the structure here consisted of a dark grey phase (Fe_2Al_5) having some regular and some irregular shapes in two-phase equilibrium with Zn, as shown in Figure 17. The composition of these two Fe_2Al_5 morphologies at the interface with zinc were different, suggesting that they correspond to different tie-lines in the same two-phase field. The zinc, in particular, was found to vary from 4.90 wt.% to 11.53 wt.% (see Table B.4), indicating

as well that long range equilibrium was not attained in the sample. The foregoing observations on the FeAl and $FeAl_2$ samples make quite clear that the latter compound is not stable in contact with zinc and that when immersed it rapidly undergoes a transformation via the zinc-bearing Fe_2Al_5 phase.

A similar strong attack was observed for the sample Fe_2Al_5-Zn(Al). There the conglomerates of blue-grey phase formed (Figure 19) were identified as zinc-bearing Fe_2Al_5 phase (see Table B.6). Thus the strong attack can be attributed solely to solution of zinc in the original binary Fe_2Al_5 phase.

Neither sample for the $FeAl_3$ binary compound yielded conclusive results because of a heavily damaged interface between the compound and zinc. However, several regions of sound interface in the sample $FeAl_3$-Zn(Al) were observed and indicated that the attack of zinc on this compound is very much slower than in a case of the Fe_2Al_5 phase. The limited attack takes place through formation of a narrow liquid-penetrated layer (see Figure 20) at the interface. This layer was identified (Table B.7) as zinc-bearing $FeAl_3$ phase.

The phase relations, based on the foregoing metallographic examinations can be summarized as follows. The phases Fe_2Al_5 and $FeAl_3$ equilibrate with zinc at 450°C by dissolving 14 wt.% and 7wt.% of zinc, respectively. The zinc-bearing Fe_2Al_5 phase forms a three-phase equilibrium with zinc-bearing FeAl and an aluminum-bearing δ_1 phase. The zinc-bearing FeAl phase also forms a two-phase equilibrium with the aluminum-bearing δ_1 phase. The rapid attack of zinc on the $FeAl_2$ phase suggests that the stability range of this phase is confined to very low zinc values.

The quantitative data presented in Tables B.1 to B.7 are conveniently summarized in Table XV for application to a construction of the Fe-Zn-Al isotherm at 450°C, as shown in Figure 33.

The iron-rich corner of the diagram along with the region near the $FeAl_2$ phase has only a qualitative character since it is constructed from limiting binary systems, and omits the complications which arise from the order-disorder reaction in the Fe-rich phase[6]. The principle tie-lines of the two phase regions and the three phase equilibrium between the zinc-bearing Fe_2Al_5 phase, aluminum-bearing δ_1 phase and zinc have been established quantitatively. This part of the isotherm will be found later to be of a crucial importance in relation to the inhibiting action of aluminum in the zinc bath.

Our results finally remove all uncertainties connected with the existence of the ternary compound identified originally by Hughes[24,25]. We see that this supposed compound located in Cameron and Ormay's isotherm of Figure 7 is actually an extension into the isotherm of the binary Fe_2Al_5 phase, the latter dissolving up to 14 wt.% of zinc. Similarly, the $FeAl_3$ phase extends to a depth of approximately 7 wt.% of zinc.

Having established the significant tie-lines and points for the aluminum-bearing δ_1 phase, (Table XV and Figure 33) we have adopted Cameron and Ormay's proposal for the zinc-rich corner with the following modifications (see Figure 32). As we demonstrated experimentally in Section 5.1, the binary iron solubility 0.029 wt.% increases slightly with increasing aluminum content of the zinc. The corner of the three phase triange ζ-δ_1-Zn is retained as being at 0.07 wt.% Al[29]. The corner of a three-phase triangle, zinc-bearing Fe_2Al_5-δ_1-Zn, has been displaced

TABLE XV

Compilation of Electron Microprobe Data
for the 450°C Isotherm of the Fe-Zn-Al System

Type of Tie-Lines	Measured on Sample	Composition (wt.%)		
		Al	Fe	Zn
Three-phase equilibrium between Fe_2Al_5 (A), δ_1(E) and FeAl (G)	FeAl-Zn		43.09	12.80
			8.23	88.15
		18.89*	69.07	12.04
	FeAl-ZnAl		42.27	13.66
			42.32	13.68
			8.47	88.31
Av.				
Zn-bearing Fe_2Al_5(A)		43.73*	42.89±1%	13.38±1%
Al-bearing δ_1(E)		3.42*	8.35±1%	88.23±1%
Zn-bearing FeAl(G)		18.89*	69.07±2%	12.04±2%
Two-phase equilibrium between Fe_2Al_5 and Zinc	FeAl-Zn(Al)		40.28	13.87
	$FeAl_2$-Zn		40.10	12.43
	Fe_2Al_5-Zn(Al)		40.52	12.14
Av.				
Zn-bearing Fe_2Al_5(C)		46.09*	40.30±2.5%	12.81±1%
Three-phase equilibrium between Fe_2Al_5(B) δ_1(F) and zinc	FeAl-Zn(Al)		41.25	14.51
			8.32	87.79
			Unreliable results	
	$FeAl_2$-Zn		41.50	13.85
			8.55	89.17
			Unreliable results	
	Fe_2Al_5-Zn		41.95	13.95
			7.47	89.45
			Unreliable results	
Av.				
Zn-bearing Fe_2Al_5(B)		44.34*	41.56±2.5%	14.10±1%
Al-bearing δ_1(F)		2.92*	8.28±0.5%	88.80±2%
			Unreliable results	

Table XV (continued)

Type of Tie-Line	Measured on Sample	Composition (wt.%)		
		Al	Fe	Zn
Two-phase equilibrium between $FeAl_3$(D) and zinc	$FeAl_3$-Zn(Al)	43.98*	39.44±2%	6.58±1%

* Al content obtained by difference.

to 0.11 wt.% Al as suggested by our X-ray analysis of galvanized specimens (see Section 6.2 below). The upper limiting tie-line of the two-phase region Fe_2Al_5-Zn remains uncertain but the existence of an equilibrium between Fe_2Al_5 and Zn (1.71 wt.% Al) shows clearly that the 1.70 wt.% Al value is a lower limit for this set of tie-lines. The limiting tie-line of the two-phase field in contact with $FeAl_3$ can be inferred from the Zn-Al binary diagram and takes the value 16 wt.% Al.

The 400°C and 500°C Fe-Zn-Al isotherms recently published by Köster and Gödecke[62] are in qualitative agreement with our results at 450°C, with a single exception. We did not, in contrast to their observations, identify an isolated δ phase field above the δ_1 phase field near the zinc corner of the diagram, although our δ_1 field (Figure 33) actually includes the area attributed by those authors to δ.

6.2 X-ray Analysis and Metallographic Examination

The metallographic observations of the galvanized samples revealed the presence of phases previously described by Bablik[22,23], Hughes[24], Haughton[26], Horstmann[27,28], Cameron and Ormay[29] and Borzillo and Hahn[30]. Thus the iron-zinc compounds could be readily identified by referring to the previous investigations and to the constitutional data gained in the present work.

The microstructure developed in iron-saturated, aluminum-bearing zinc baths exhibited the following types of structures:

(a) Outbursts of a grey spongy phase containing a second phase which nucleates at the iron interface, as illustrated in Figures 21 and 22. The phase at the iron interface (3) nucleated within a short time and grew rapidly in thickness along the the original phase (2). This latter phase was formed only in baths containing 0.11 and 0.15 wt.% Al. The nucleation and growth was suppressed by higher aluminum contents and agitation, the time of immersion having the inverse affect. This structure was identified as aluminum-bearing ξ with an occluded aluminum-bearing δ_1 phase at the iron interface.

(b) A grey phase having a compact appearance when nucleated (1) (Figures 23 and 25) and contacting at later stages a very thin layer of another phase which has nucleated at the iron interface (1) (Figure 26). While the former phase, following nucleation, grew with time, the latter maintained an essentially fixed thickness, being hardly detectable. The phase (1) (Figures 23 and 25) was detected at the higher aluminum contents (0.22% and 0.32%) and its nucleation and growth was retarded by even higher aluminum contents and agitation. Long immersion times facilitated nucleation of this phase. Once nucleated, this phase grew rapidly toward the iron and the zinc, simultaneously extending sideways along the iron-zinc interface. These characteristics help us to identify the bulk grey phase as aluminum-bearing δ_1-phase with Γ being formed at the iron interface.

(c) The structure formed at early times as an optically unobservable film*

---

* In a subsidiary experiment not reported here we have succeeded in stripping and identifying this early stage film and found it to have thickness of $\sim$ 0.25 micron.

at the iron-zinc interface drew most of our attention. Increasing the aluminum content, agitation and dipping time favoured further growth of this structure, firstly by formation of overall semi-detached crystals at the interface (I) (Figures 21 and 22), and which with higher aluminum contents and longer dipping times tended to grow and form outbursts (2) (Figures 23 and 25) or rough continuous layers of measurable thickness (I) (Figure 24). The latter mode was favoured by higher aluminum contents in the bath leading with the highest values to formation of a thick layer which later broke away from iron (Figure 27).

Characteristic of this structure was the difficulty of distinguishing it metallographically from the base metal since there was no apparent interface between the structure and iron. The phase grew predominantly towards the zinc, exhibiting a discernible penetration of the iron only below pronounced outbursts.

The electron probe microanalysis carried out on a well-developed aluminum-rich alloy layer, shown in Figure 27, identified that the bulk of this phase consists of the zinc bearing Fe_2Al_5 phase. We wish to emphasize, however, that this result, presented in Table XIV, should be considered with some reservations. The surface diffraction experiments clearly indicated the presence in the structure of other iron-aluminum phases.

The results of X-ray analysis of the intermetallic phases formed on samples galvanized in aluminum-bearing zinc by other authors provides very valuable information, but are by no means systematic, thus often leading to controversial conclusions. Hughes[25], in analysing chemically the intermetallic layer formed in a zinc bath containing 15% Al, disclosed its

ternary character. He also postulated that the aluminum in this layer was present as the $FeAl_3$ phase. Haughton[26], using the X-ray powder method, identified the inhibiting layer formed on specimens galvanized in zinc baths containing 0.10 wt.% Al as the Fe_2Al_5 phase. Horstmann[27] identified the presence of the phases Fe_2Al_5 and FeAl on samples prepared in a 0.5% Al-zinc bath, using a surface diffraction method. In addition a number of unidentified lines were recorded by Horstmann and these were ascribed to two unknown ternary compounds. Cameron and Ormay[29] identified Fe_2Al_5 in the surface layer without referring to the aluminum content of the bath. Finally, Borzillo and Hahn[30], using surface X-ray analysis on specimens prepared in 0.2 and 0.3 wt.% Al zinc baths, identified the Fe_2Al_5 phase along with some unidentified lines which were supposed to be due to a particulate ternary blue-grey phase.

From all the available data it was evident that to arrive at conclusive results systematic X-ray analysis would have to be undertaken. Thus, a surface diffraction study was carried out on samples prepared under carefully defined conditions for the formation and growth of the inhibiting alloy layer.

In the following paragraphs we present a critical discussion of the basic X-ray data on which our study must be based. A number of unidentified lines have previously appeared in published work and the possibility that some of them are due to the phase $FeAl_2$ cannot be excluded. The crystallographic data for this phase are not in the ASTM X-ray Diffraction Data File. Our d-spacings for $FeAl_2$ and their intensities, as given in Table C.1, support the proposal of Bradley and Taylor[91] that the diffraction pattern of this phase is too complicated to be attributed to the simple rhombohedral structure proposed by Osawa[8]. The presence

of lines with d-spacings 2.050 and 2.11 Å in our $FeAl_2$ diffraction pattern needs discussion since both also represent principal lines for the Fe_2Al_5 phase. It cannot be decided for sure at this time whether these two lines pertain to the actual pattern of $FeAl_2$ or result from a small amount of Fe_2Al_5 contamination.

The d-spacings obtained in our examination of phase Fe_2Al_5 (Table C.2) are, in most cases, identical with those reported in the ASTM X-ray Data File. It should be noted that the line given in the ASTM File by the d-spacing 3.86 Å was found by us to be displaced to a higher angle of reflection (d = 3.809 Å). A similar displacement, but lower in absolute value, was detected for the line given in the ASTM File for d-spacing 2.39 Å. (Our recorded value = d = 2.364 Å). Horstmann[27] also reported Fe_2Al_5 phase lines with d-spacings 3.81 Å and 2.36 Å so the ASTM Data File is obviously in error. The extra line at d = 2.102 Å apparently indicates that traces of $FeAl_2$ phase were present in the Fe_2Al_5 plane.

The diffraction pattern obtained for the $FeAl_3$ phase as presented in Table C.3 exhibits very good agreement with that reported in the ASTM X-ray Data File. We note, however, that four reflections, having d-spacings 2.23, 2.08, 1.98 and 1.93 Å, are missing from our pattern. The relative intensities of the majority of recorded reflections are different. This effect was expected as a consequence of the adopted mounting method for powdered specimens, leading to preferred orientations. The d-spacings 4.90, 3.82, 3.20, 2.05 and 1.94 Å could clearly be identified as those for the Fe_2Al_5 phase, indicating traces of this phase to be present in the $FeAl_3$ standard.

The data obtained from surface diffraction analysis of galvanized specimens as given in Tables C.4 to C.27, were analysed and rearranged to show more transparently the effect of the aluminum content of the bath and immersion time on structural changes of the inhibiting alloy layer. The measured reflections could, in most cases, be positively identified through corresponding d-spacings given in the ASTM X-ray Data File or obtained in the present study. A strong preferred orientation, generally developed during growth of the inhibiting alloy layer, prevented us from drawing any meaningful conclusions from a comparison of relative intensities of diffraction lines.

The analysed results of the surface diffraction studies are presented in Tables XVI to XX in a self-explanatory manner. We shall focus our attention on overall trends in the development of an inhibiting layer, emphasizing the points for further debate.

Table XVI demonstrates that even at low aluminum contents in Bath I (0.11 wt.% Al) the interfacial nuclei of phases Fe_2Al_5 and $FeAl_3$ had developed within 10 sec. With increasing time the intensity of these phase lines slightly increased. For times of 10 minutes very strong lines of $FeAl_3$ were recorded along with very strong lines of zinc. On this sample the stripping process was intentionally stopped before the dissolving reaction ceased. Thus the traces of a zinc overlay were left on the interface. Even if a definite conclusion cannot be drawn from this single instance, the substantially increased intensities of $FeAl_3$ diffraction lines suggest that the zinc overlay stripping solution also lightly etches the aluminum alloy layer. This interrupted stripping was not adopted for other specimens since it would in general introduce

TABLE XVI

Summary of Analysed Surface Diffraction Data for Samples Produced in Bath I

Compound or Element	d	I/I_o	10 sec		1 min		3 min		10 min		30 min	
			d	I	d	I	d	I	d	I	d	I
Zn	2.47	53							2.47	700		
	2.308	40							2.306	568		
	2.091	100							2.090	7700		
	1.687	28							1.685	410		
Fe	2.026	100	2.025	73	2.024	35	2.024	30				
Fe_2Al_5	3.86	24			3.812	24						
	3.20	40	3.187	18	3.204	69	3.195	32				
$FeAl_3$	2.23	40					2.198	30	2.196	140		
	2.16	10	2.167	15					2.155	100		
	2.12	40			2.129	27	2.135	178	2.133	550		
$FeAl_2$	3.828	19			3.799	24						
	2.742	12							2.74	21		
	2.176	28							2.76	28		
Unidentified			6.33	40								

I (counts/sec)
o
d (A)

diffraction lines of iron-zinc compounds making the interpretation of the diffraction patterns obtained less conclusive. It should be also noted that for the 1 minute and 10 minute samples lines of $FeAl_2$ phase were also recorded.

Some uncertainty is attached to the lines with spacing 3.799 (attributed to $FeAl_2$) and 2.196 Å (attributed to $FeAl_3$) since the listed spacings (Table XVI) are 3.828 and 2.23 Å, respectively.

Increased aluminum content in Bath II (0.15 wt.% Al) produced an inhibiting layer represented (for 10 sec. immersion time) by a very thin film at the iron-zinc interface. As indicated in Table XVII, this layer apparently consists of the phases Fe_2Al_5 and $FeAl_3$. With increasing time of immersion this film was observed to grow slowly, forming irregular interfaces with a semi-detached blue grey crystal of Fe_2Al_5. Table XVII shows that during this development the inhibiting layer maintains its structure. The number and intensity of diffraction lines have increased reaching a maximum at 3 minutes. The results for longer immersion times suggest that the amount of aluminum-rich phase decreases due to their transformation into iron-zinc rich compounds in general agreement with the metallographic observations. All the detected diffraction lines had d-spacings in excellent agreement with those reported in the ASTM X-ray Data File or obtained in the present study. It should be noted finally that several lines that could not be assigned to known compounds have been recorded as well.

We must recall that the microstructure of samples galvanized in Bath III (0.22 wt.% Al) for 10 seconds was formed mainly as a thin film with small blue-grey crystals growing irregularly from the iron inter-

TABLE XVII

Summary of Analysed Surface Diffraction Data for Samples Produced in Bath II

Compound or Element	d	I/I_o	10 sec		1 min		3 min		10 min		30 min	
			d	I	d	I	d	I	d	I	d	I
Fe_2Al_5	3.86	24	3.809	13	3.812	14	3.80	55	3.809	11		
	3.20	40	3.201	30	3.198	20	3.199	62				
	1.94	10			1.945	14						
	1.90	8					1.898	10	1.890	12		
Fe	2.026	100	2.024	91	2.026	25	2.023	13				
$FeAl_3$	3.95	40			3.97	30	3.972	40	3.97	42		
	3.68	60	3.689	16								
	2.23	40									2.213	10
	2.12	40			2.127	24	2.126	70				
	2.09	100										
	2.08	40					2.074	25				
	2.06	40			2.064	20	2.062	30				
$FeAl_2$												
Unidentified			6.389	21	3.175	20	6.334	28				
			6.245	25	6.393	33	6.206	18				
			5.768	21								

I (counts/sec)
 o
d(A)

face. The results of the surface diffraction analysis (see Table XVIII) indicate again that the inhibiting alloy layer at this stage consists of phases Fe_2Al_5 and $FeAl_3$. With increasing immersion times, the blue-grey crystals were more frequent, finally forming identifiable outbursts. Correspondingly the number and intensity of diffraction lines of both phases have increased, their maxima being reached at 3 minutes (i.e., at the stage when the blue-grey phase crystals begin to form outbursts and the δ_1 phase starts to nucleate, as shown in Figure 23).

Samples produced with immersion times over 3 minutes clearly suggest a diminishing amount of both phases, apparently as a result of their transformation to the δ_1 phase. For the 30 minute samples, one line of $FeAl_2$ phase was recorded. We also note that three unidentified lines were detected.

In Table XVIII assignment of the lines with d-spacings 3.327 and 2.068 Å to the $FeAl_3$ phase might be considered as objectionable. Indeed, both these diffraction lines could very well belong to the $FeAl_2$ phase, since this phase exhibits a relatively weak reflection with a spacing d = 3.321 Å and a stronger one having d = 2.066 Å. However, the latter line has occurred prominently in most samples, thus suggesting that it belongs to the $FeAl_3$ compound. The d=3.321 Å line does not lend itself to a similar explicit conclusion since it was recorded in the one instance only.

The galvanized samples prepared in Bath IV (0.32 wt.% Al) exhibited very similar microstructural features to those produced in the Bath III. However, small differences in diffraction patterns for these samples are to be noted.

Referring to Table XIX we note first that only the lines of

TABLE XVIII

Summary of Analysed Surface Diffraction Data for Samples Produced in Bath III

Compound or Element	d	I/I_o	10 sec		1 min		3 min		10 min		30 min	
			d	I	d	I	d	I	d	I	d	I
Fe_2Al_5	4.90	11			4.92	15	4.927	14				
	3.86	24	3.801	19	3.806	23	3.814	135	3.809	10	3.812	30
	3.20	40	3.20	27	3.20	52	3.207	122	3.20	42		
	2.11	100			2.116	12	2.116	138	2.109	97		
	2.05	100							2.059	41		
	1.94	10					1.942	55	1.94	25		
Fe	2.026	100	2.027	90	2.026	14	2.027	30			2.022	30
$FeAl_3$	3.54	60										
	3.33	20	3.327	13								
	2.12	40			2.13	45	2.13	202	2.126	45		
	2.09	100										
	2.08	40					2.075	95				
	2.06	40	2.068	24	2.066	22	2.065	188				
	1.93	40					1.928	28			1.926	21
$FeAl_2$	3.568	61									3.567	12
Unidentified					5.277	10			6.193	10	6.197	33

I (counts/sec)

d(A)

TABLE XIX

Summary of Analysed Surface Diffraction Data for Samples Produced in Bath IV

Compound or Element	d	I/I_o	10 sec		1 min		3 min		10 min		30 min	
			d	I	d	I	d	I	d	I	d	I
Fe_2Al_5	4.90	11							4.902	11		
	3.86	24			3.806	17	3.817	82	3.801	78		
	3.20	40			3.207	22	3.209	170	3.201	84		
	2.11	100					2.115	375	2.113	230		
	2.05	100			2.059	22						
	1.94	10					1.942	112	1.942	70		
	1.90	8			1.902	20	1.908	23				
Fe	2.026	100	2.023	66	2.026	30	2.026	29			2.026	10
$FeAl_3$	3.95	40	3.937	20								
	2.36	10					2.366	18	2.36	28		
	2.23	40	2.205	20	2.198	15						
	2.12	40			2.129	13	2.127	210	2.126	140		
	2.09	100	2.093	15			2.091	35	2.092	24		
	2.08	40							2.072	80		
	2.06	40			2.067	25	2.066	194	2.065	105		
	2.02	100			2.020	22						
	1.98	20			1.983	19						
$FeAl_2$	2.742	12	2.738	13								
Unidentified			2.567	21					6.298	21		
									6.241	27		

I (counts/sec)

o

d (A)

the $FeAl_3$ and $FeAl_2$ phases were detected for the 10 second sample. The lines of the Fe_2Al_5 compound are missing. However, considering that very low intensities of diffraction lines have been recorded for the shortest immersion times in all cases, the expected faint lines of the Fe_2Al_5 phase might very well have been lost due to a small eccentricity error.

A more serious discrepancy is associated with the 30 minute sample. Despite the fact that the microstructure of this sample was formed of a mixture of iron-zinc and aluminum-rich compounds, no lines of the aluminum-rich phases were recorded. This might be attributed to two factors. The metallographically-viewed section may not have been representative of the average surface which was viewed by the X-rays, and again the eccentricity error might have led to a loss of weak diffraction lines.

The remaining samples displayed a similar tendency in structural changes of the growing inhibiting alloy layer. With prolonged immersion times, the inhibiting layer, consisting of increasing amounts of blue-grey phase, was identified again as being composed of Fe_2Al_5 and $FeAl_3$ phases. The inhibiting effect was sustained up to 10 minutes. At this stage, a relatively thick alloy layer tended to peel off promoting the nucleation of the δ_1 phase at an uncovered iron interface.

For all samples in bath IV only three unidentifiable diffraction lines were recorded.

The results of the surface diffraction of samples produced in Bath V (with the highest aluminum content of 1.10 wt.% Al) have supported the principal conclusions drawn from the foregoing analysis. Furthermore, in this case a more extensive set of diffraction lines for the $FeAl_2$ compound was detected, particularly for the 10 second and 3 minute

TABLE XX

Summary of Analysed Surface Diffraction Data for Samples Produced in Bath V

Compound or Element	d	I/I_o	10 sec		1 min		3 min		10 min		30 min	
			d	I	d	I	d	I	d	I	d	I
Fe_2Al_5	4.90	11			4.933	18						
	3.86	24	3.824	16	3.83	25	3.833	42	3.830	48	3.824	73
	3.20	40	3.20	48	3.210	102	3.215	121	3.213	106	3.210	115
	1.94	10	1.939	18	1.946	40	1.946	63	1.947	78	1.945	71
	1.90	8			1.902	10					1.904	20
Fe	2.026	100	2.026	42	2.029	6			2.027	5		
$FeAl_3$	3.95	40										
	3.68	60										
	3.54	60	3.553	60								
	2.16	10									2.162	12
	2.12	40	2.123	20	2.120	236	2.121	500	2.124	380	2.121	330
	2.09	100					2.095	190	2.095	18		
	2.06	40			2.066	119	2.069	130	2.069	162	2.068	250
	2.02	100					2.018	11				
$FeAl_2$	3.828	19			3.847	25						
	2.742	12					2.757	16				
	2.176	28	2.18	18			2.183	19	2.189	10		
	2.26	15	2.26	7			2.27	13				
Unidentified			6.236	10			6.236	10	3.155	10		
							4.248	12				
							4.031	22				
							2.495	18				

I (counts/sec)

d (Å)

samples. In addiition, another six diffraction lines could not be assigned to the known compounds.

Even though the foregoing results of the surface diffraction analysis are highly conclusive as regards the inhibiting layer constitution, there still remains the problem of the unassigned lines at d-spacings:

6.39, 6.33, 6.30, 6.24, 6.20, 5.76, 5.27, 4.25, 4.03, 3.17, 3.15, 2.56 and 2.50 Å

The rather erratic occurrence of the unidentifiable lines for different samples led us to the conjecture that these are due exclusively to a residual arsenic film. This film is left on every sample after stripping the zinc overlay and was supposed to be removed by flash immersion in cold concentrated nitric acid. Presumably, different samples were covered with varying amounts of arsenic film. Thus, sustaining the flash procedure for constant times would remove the films by different extents.

To verify this possible effect of the residual arsenic film on the diffraction patterns obtained, the aluminum-rich alloy layer was removed from two samples and these were subjected again to surface diffraction. Results of this supplementary X-ray analysis are given in Tables XXI and XXII. We note that by excluding the residual diffraction lines of $FeAl_3$ and $FeAl_2$, a number of additional lines are now observed. Comparing this data with the previously unidentified lines we conclude that the diffraction lines having d-spacings of 6.20, 4.25, 3.17 Å and possibly 6.24 and 3.15 Å are exclusively due to the arsenic film residuum.

TABLE XXI

The Diffraction Lines Obtained from the Residual Arsenic Film on the Sample Produced by 3 minutes Immersion in Bath V

d (Å)	5.539	4.468	4.332	4.264	3.17	2.812	2.82	2.235	2.025
I (counts /sec)	8	10	10	10	15	28	25	6	80

TABLE XXII

The Diffraction Lines Obtained from the Residual Arsenic Film on the Sample Produced by 10 minutes Immersion in Bath V

d(Å)	6.206	5.539	2.673	2.492	2.362	2.188	2.145	2.12	2.028
I (counts /sec)	15	15	10	12	10	18	20	10	45

More data is needed to draw definite conclusions in this respect since eight diffraction lines remain unassigned. However, taking into account the anticipated complexity of the arsenic film diffraction pattern, possible effects of sodium hydroxide on the structure of the film and a possible preferred orientation effect we may conclude that our brief experiment is a sufficient indication for present purposes. It focuses attention on an additional proven source of diffraction lines that has not been previously taken into account and further undermines the credibility of the conjectured ternary compound to which some of these lines had been previously assigned.

Summarizing, we may say that under the given experimental conditions, which are close to commercial practice, the inhibiting alloy layer formed on iron galvanized in an aluminum-bearing zinc bath has a dual structure, composed of zinc-bearing Fe_2Al_5 and $FeAl_3$ phases. The latter two phases form the bulk of the inhibiting layer but may occasionally be accompanied by the formation of particles of the $FeAl_2$ phase.

The phase FeAl, on the basis of its very low Fe-like diffusion coefficients, is not expected to attain a detectable thickness in times of 30 minutes, and our experiments bear this out. In any case, the kinetic properties of FeAl should be close enough to those of pure iron so that there is little point in distinguishing between these two phases in discussions of galvanizing. It was for this reason that we approximated Fe-FeAl as a single phase field in our ternary isotherm (Figure 33).

The unidentified diffraction lines from the surface layers most probably derive from an arsenic film residuum.

6.3 Explanation of the Aluminum Inhibiting Action

The X-ray analysis and electron microprobe data, along with the microscopic evidence developed in the present study, allow us to more clearly define the mechanism by which aluminum inhibits iron-zinc alloy layer growth on galvanized iron.

To introduce the argument the problem of nucleation of intermediate phases will be first discussed. The subsequent growth of the nucleated phases and the mechansim of their destabilization will then be discussed in relation to the concept of diffusion path on the isotherm of the Fe-Al-Zn system.

Consider a ternary solid-liquid diffusion couple at time zero such as the infinite couple formed at 450°C by iron in contact with iron-saturated zinc containing from 0.20 to 1.0 wt.% of aluminum. An intermediate phase will be nucleated at the interface provided that the overall free energy of the system is lowered by such a process and provided that the nucleation barrier is not too high. If the phase diagram defines the existence of such intermediate phases, as in the example considered, then the former free energy requirement will be automatically satisfied. However, the height of the free energy barrier associated with the formation of such intermediate phases depends on three terms: a negative volume component (which is the measure of the minimizing tendency) and positive surface and strain components which tend to counteract this. The strain component arises if the volume changes associated with the nucleation of the new phase are significant. Depending upon the relative magnitudes of these components, which depend on the supersaturation,

the fluctuations in the system may be sufficient to help the system overcome the barrier due to the last two terms and lead to the desired minimum associated with the volume term.

For the case of a ternary solid-liquid diffusion couple of the type considered the nucleation of a new phase may be expected to occur at the solid-liquid interface since the degree of supersaturation is greatest at this point and a portion of the necessary surface for nucleation of a new phase is already present. Furthermore, where the interface is supersaturated with respect to a number of phases, the one which appears first will be that for which the nucleation barrier is lowest. Thus, as expected theoretically, the nuclei of the initial inhibiting layer in galvanizing (which seems circumstantially to be Fe_2Al_5) is observed to be attached to the iron and growing towards the liquid part of the couple, and we may suppose therefore that Fe_2Al_5 has a lower nucleation barrier than at least five other possible initiating phases.

From nucleation theory we argue that the number of critical nuclei, n, present in a system is given by Burke[65] as

$$n = N \exp\left(-\frac{\Delta F}{kT}\right)$$

where N is the number of available nucleation sites and ΔF is the free energy barrier for formation of a critical nucleus (i.e., the nucleus which may lower its free energy by growing in size by an infinitesimal amount). This free energy of formation, as pointed out before, is composed of volume, strain and surface terms. A critical nucleus becomes a stable

one when it gains one or more atoms. Thus, if the jump process across the precipitate-matrix interface is governed by an activation energy, U, the frequency with which critical nuclei become stable is:

$$n_S \; p \; \gamma \; \exp\,(-U/kT)$$

where n_S is the number of atoms in the matrix at the surface of the critical nucleus, γ is the frequency of vibration of these atoms, and p is the probability that a vibration is in the direction of the nucleus times a factor which expresses the fact that attachment of atoms may occur preferentially at certain points on the surface. Under quasi-steady state conditions the nucleation rate, I, is then:

$$I = N \cdot n_S \cdot p \cdot \gamma \cdot \exp\left(-\frac{U+\Delta F}{kT}\right)$$

The most important factor in this expression is the free energy of formation of a critical nucleus. If the strain and surface terms are large compared to the volume component of the free energy, the nucleation rate will be slow and can in fact be negligible.

Once the stable nuclei of the intermediate phases are formed we may consider the problem of their growth. The inhibiting layer growth was found by Borzillo and Hahn[30] to conform to a parabolic law. The rate of its growth is therefore governed by the diffusion coefficients of the three elements in the intermediate phases. The general solution of this problem, given by Kirkaldy[31] would be difficult to apply. Furthermore, rapidly developing instabilities at the interface with zinc would ultimately

lead to more than two phases in equilibrium and the failure of the planar model. It is doubtful that there will ever be developed a tractable theory that can deal with the singularities (outbursts) observed. In any case, the required diffusion data for analysis are extremely scarce, even for the binary alloy systems involved. Bugakov[64] gives the diffusion coefficient of iron in binary Γ phase at 400°C as $D_{Fe} = 2.10^{-9}$ cm^2/sec. Ryabov et al.[65] obtained diffusion coefficients of iron at 1000°C in the phase $FeAl_2$ as $D_{Fe} = 8.10^{-11}$ cm^2/sec, the phase Fe_2Al_5 as $D_{Fe} = 3.10^{-9}$ cm^2/sec, and the phase $FeAl_3$ as $D_{Fe} = 2.10^{-10}$ cm^2/sec. No diffusion data is available for the ternary system discussed. However, observations of the extremely small rate of grwoth of the inhibiting alloy layers as compared to that of the iron zinc rich phases suggest that the diffusion coefficients for these two groups of phases differ by at least two orders of magnitude at temperatures of 450°C. Bearing all the above in mind, we may attempt to treat the problem of growth and diffusional instabilities of the inhibiting layers according to the concept of virtual diffusion paths in the isotherm as described in Section 3.3. It must be emphasized that such paths are only uniquely defined subsequent to nucleation of one or more intermediate phases (stable or metastable) and that subsequent nucleation of more stable intermediate combinations of phases will lead, after appropriate relaxation times, to a discontinuous modification of the diffusion paths. We start our discussion on the empirical basis that the initial phase nucleated is Fe_2Al_5 followed immediately by $FeAl_3$. This initial stage corresponds to the metastable diffusion path Fe I J K D' C", shown in Figure 34. The first part of the path, up to

point K, implies that the nucleated compounds are not saturated with zinc and that the diffusion coefficient of aluminum in the iron-rich phases Fe and Fe_2Al_5 are much higher than the coefficients for zinc in these phases.

The path IJ simply denotes a layer of zinc bearing Fe_2Al_5 phase. Its interface with the adjacent zinc bearing $FeAl_3$ phase is assumed to be planar for very short times, i.e., the path JK is shown as parallel to tie-lines in the two phase region. The path KD' implies a sharp increase in the diffusion rate of Zn relative to Al, and indeed that, due to ternary diffusion interactions, Al now diffuses down the Zn gradient and up its own gradient.

At this point, it should be stressed that if the zinc part of the couple were a solid, the composition gradients of all elements would be fixed, defining unambiguously the diffusion path. In a liquid, on the other hand, the concentration gradients can be dispersed by agitation, to allow the initial activity of a minor component in the bulk liquid to be maintained at a high level at the solid-liquid interface, thus favouring the stability of the Al-rich Fe-Al compounds. The interfacial concentration of the minor component may nonetheless be depressed due to diffusion depletion of the melt in the vicinity of morphological instabilities, thus destabilizing the Al-rich layers. All of this goes to say that there is no a priori way of fixing the Al content of the melt at the interface in the presence of agitation or of instability.

Let us assume, therefore, that the interfacial concentration of aluminum in the melt at the short times considered, due to a high Al content and/or agitation, is given by point C". This path, in the absence

of nucleation of other Fe-Al phases would be permanently stable, at least against intrusions of Fe-Zn-rich solid phases in the absence of mechanical instabilities (e.g., flaking).

If, as is more likely, the interface compositions evolve by depletion to those defined by line DHC then gross instabilities are to be expected next to the liquid since this path crosses both two and three-phase regions. The line DHC implies a local equilibrium surface involving three phases: Fe_2Al_5, $FeAl_3$ and zinc, in contact with a two-phase region Fe_2Al_5-liquid. This diffusion path appears to well-represent the situation for short times of immersion, as indicated in the right half of the Figure 22. This exhibits mainly a planar interface between $FeAl_3$ and zinc along with a very limited number of protruding small crystals of Fe_2Al_5.

Let us consider next a location of the interface where the assumed instability has become critical, i.e., the zinc-saturated $FeAl_3$ phase has been penetrated by a column of zinc-bearing Fe_2Al_5 phase, growing into the zinc. The aluminum required for the growth of this phase can be supplied from the zinc bath and from dissolution of the zinc-bearing $FeAl_3$ phase. The first of these transfer processes will result in a decrease in the amount of liquid zinc residing between the columns of Fe_2Al_5 phase, i.e., the point H will be displaced toward H'. Concommitantly, the aluminum concentration at the growing tips of the Fe_2Al_5 will decrease towards point C' and the corresponding decrease in the amount of $FeAl_3$ phase will result in a swing of the diffusion path towards the curve I L H'.

If the aluminum content in the bath is not maintained, further growth of the zinc bearing Fe_2Al_5 phase must continue until all the zinc-

bearing $FeAl_3$ phase is consumed. Correspondingly, the diffusion profile must swing towards path I F A. At this stage further columnar growth of the Fe_2Al_5 phase must receive its supply of Al from the bath only. A subsequent drop in the aluminum concentration in the liquid (say to point N) in contact with a zinc-saturated Fe_2Al_5 phase must be achieved via nucleation of the zinc-rich δ_1 phase which, according to the phase diagram, will rapidly penetrate through the thin Fe_2Al_5 layer. The corresponding diffusion path is then represented by points IFMN. Figure 23 demonstrates this eventuality. The nucleus of δ_1 phase formed exhibits a well-defined, nearly planar interface with the iron (which was previously in contact with the Fe_2Al_5) and a non-planar interface with zinc corresponding to the last segment of the diffusion path MN (entering from a three-phase region into a two-phase region at an angle to the tie-lines). Once the three-phase equilibrium is established, the system will tend to minimize its free energy further through the reaction:

$$\text{Zinc} + Fe_2Al_5(Zn) \rightarrow \delta_1$$

This stage is characterized by a very rapid sidewize growth of the δ_1 phase, encouraging the peeling of the zinc-bearing Fe_2Al_5 phase, which is ultimately dissolved during upward growth of the δ_1 phase.

At the point where the δ_1 phase is first formed the nucleation of Γ phase at the iron interface follows within a short time.

The corresponding diffusion path for this locale passes then through points FeOGN.

The foregoing argument implies that at higher aluminum contents in the bath both the amount of initially formed $FeAl_3$ phase and the general availability of aluminum from the zinc are greater. Consequently, the diffusion path IJDHC swings at slower rate towards the path IFA. In other words, displacement of points L and H towards E is decelerated, implying a slower development of ternary instabilities. During this evolutionary process the bulk of the inhibiting layer probably consists of a zinc-bearing Fe_2Al_5 phase with a thin fragmented overlay of $FeAl_3$.

Increased agitation acts in the same direction as increased Al in the bath by providing a steeper gradient of aluminum at the solid-liquid interface and therefore a faster supply of the element. Consequently, as observed, it provides a more even growth of the inhibiting layer.

The rate of growth and destabilization of the inhibiting layer was also found to be affected by iron content in the zinc bath. In accounting for the iron effect let us recall that the inhibiting layer was observed to grow predominantly towards the zinc, exhibiting at the same time a negligible penetration into the iron. This indicates that iron diffusion through the intermediate phases formed controls their growth rate. If the zinc bath is not saturated with iron the mass balance requires that a small amount of iron be transported through the intermediate phases into the zinc in addition to the iron required for formation of the advancing inhibiting phases, thus slowing down their growth and lengthening the time of onset of instability. In other words, at a given aluminum content the growth rate of the inhibiting layers increases and the time for destabilization decreases as the iron content of the bath is raised towards the saturation condition.

In summary, a regular sequence of the iron-zinc phases formed on a galvanized iron is inhibited in an aluminum-bearing zinc bath by the formation of metastable layers consisting of zinc-bearing Fe_2Al_5 and $FeAl_3$ phases. The incubation period for breakdown to a stable phase distribution is governed by the rate at which ternary diffusional instabilities are developed. Stirring and increasing aluminum content in the bath prolong the time of instability development whereas increasing iron content in the bath has the opposite effect.

SUMMARY

1. A number of important elements of the phase equilibrium in Fe-Zn-Al at 450°C have been recorded. These are summarized along with the data of other investigations in Figures 32 and 33, respectively.

2. The inhibiting layer formed on iron galvanized at 450°C in iron saturated zinc containing between 0.11 to 1.10 wt.% Al was identified by surface X-ray diffraction as being composed of zinc bearing Fe_2Al_5 and $FeAl_3$ phases.

3. The presence of the $FeAl_2$ phase in the inhibiting layer was recorded, even though with the erratic occurrence. The phase FeAl has not been detected by the technique utilised.

4. Electron probe microanalysis suggested that bulk of the inhibiting layer is formed by zinc bearing Fe_2Al_5 phase.

5. The X-ray diffraction data for $FeAl_2$ binary phase, so far missing in the ASTM X-Ray Data File, have been obtained in the range $5^\circ < \theta < 25^\circ$ using the diffractometer technique.

6. In the diffraction pattern of the phase Fe_2Al_5 listed in the ASTM X-Ray Data File a discrepancy has been recorded for line given by d-spacing 3.86 Å. Our own measurement yielded a value of 3.81 Å.

7. The mechanism by which the aluminum in the zinc bath inhibits the growth of the intermetallic phases on the galvanized iron has been proposed.

APPENDIX A

PRELIMINARY RESULTS OF THE ELECTRON PROBE MICROANALYSIS

TABLE A.I

Microanalysis Data and Results for Iron-Aluminum Binary Intermetallic Phases at the Acceleration Voltage E_o = 14 keV

	Raw Intensity from Pure Elements (counts/sec)	
	Aluminum	Iron
Initial	9,868	40,305
Final	9,528	40,512

Compound	Raw Intensity (counts/sec)		Composition (wt.%)	
	Al	Fe	Al	Fe
FeAl	554	26,502	12.40	67.58
	573	26,597	13.02	67.93
	562	26,571	12.62	67.80
$FeAl_2$	1,761	19,321	36.60	53.47
	1,725	19,965	35.91	53.79
	1,721	19,889	35.71	53.57
Fe_2Al_5	2,160	17,592	42.78	48.09
	2,063	17,592	40.54	47.98
	2,053	17,644	40.36	48.05
$FeAl_3$	2,436	15,051	44.46	41.44
	2,530	15,253	46.92	42.13
	2,616	15,249	48.83	42.23

TABLE A.2

Microanalysis Data and Results for Iron-Aluminum Binary Intermetallic Phases at the Acceleration Voltage E_o = 16 keV

	Raw Intensity from Pure Elements (counts/sec)	
	Aluminum	Iron
Initial	11,215	60,970
Final	11,171	60,802

Compound	Raw Intensity (counts/sec)		Composition (wt.%)	
	Al	Fe	Al	Fe
FeAl	551	40,321	12.29	67.71
	559	40,556	12.55	68.15
	560	40,402	12.53	67.89
$FeAl_2$	1,867	29,399	37.75	52.34
	1,817	29,268	36.41	51.99
	1,796	29,343	35.98	52.08
Fe_2Al_5	2,394	26,722	47.19	48.81
	2,338	26,761	45.95	48.38
	2,334	26,662	45.67	48.19
$FeAl_3$	2,954	22,961	54.29	42.16
	2,907	23,596	54.34	43.31
	2,901	23,248	53.59	42.64

TABLE A.3

Microanalysis Data and Results for Iron-Aluminum Binary Intermetallic Phases at the Acceleration Voltage E_o = 13 keV

	Raw Intensity from Pure Elements (counts/sec)	
	Aluminum	Iron
Initial	12,301	80,544
Final	12,310	79,526

Compound	Raw Intensity (counts/sec)		Composition (wt.%)	
	Al	Fe	Al	Fe
FeAl	388	52,769	8.49	66.09
	391	52,542	8.58	65.80
	381	52,674	8.31	65.93
$FeAl_2$	1,588	37,906	30.66	50.20
	1,567	38,036	30.27	50.32
	1,565	37,912	30.14	50.15
Fe_2Al_5	2,090	34,835	39.67	46.99
	2,045	35,032	38.82	47.18
	2,037	35,020	38.62	47.15
$FeAl_3$	2,747	30,327	49.39	41.68
	2,631	30,248	46.70	41.39
	2,608	30,662	46.72	41.95

TABLE A.4

Microanalysis Data and Results for Iron-Aluminum Binary Intermetallic Phases at the Acceleration Voltage E_o = 20 keV

	Raw Intensity from Pure Elements (counts/sec)	
	Aluminum	Iron
Initial	12,681	97,292
Final	13,142	99,649

Compound	Raw Intensity (counts/sec)		Composition (wt.%)	
	Al	Fe	Al	Fe
FeAl	108	62,994	2.36	63.66
	128	63,975	2.83	64.39
	127	63,475	2.80	64.28
$FeAl_2$	1,337	45,554	26.56	49.28
	1,300	45,305	25.56	48.89
	1,290	45,383	25.36	48.95
Fe_2Al_5	1,812	44,186	37.34	48.94
	1,748	44,321	35.82	48.99
	1,745	44,485	35.87	49.13
$FeAl_3$	2,082	39,970	40.28	44.56
	2,281	38,745	43.87	43.50
	2,274	38,941	43.91	43.72

TABLE A.5

Microanalysis Data and Results for Iron-Aluminum Binary Intermetallic Phases at the Acceleration Voltage E_o = 22 keV

	Raw Intensity from Pure Elements (counts/sec)	
	Aluminum	Iron
Initial	12,571	116,720
Final	12,393	113,414

Compound	Raw Intensity (counts/sec)		Composition (wt.%)	
	Al	Fe	Al	Fe
FeAl	0.0	78,473	0.0	65.31
	0.0	79,192	0.0	65.94
	0.0	78,010	0.0	64.90
$FeAl_2$	513	55,646	9.92	47.53
	483	54,727	9.14	46.60
	419	54,269	7.76	45.96
Fe_2Al_5	1,005	51,711	19.84	45.58
	902	50,564	17.11	44.20
	845	50,572	15.87	44.04
$FeAl_3$	1,070	46,510	19.29	40.91
	1,373	44,618	24.94	39.88
	1,376	46,413	25.96	41.59

TABLE A.6

Microanalysis Data and Results for Iron-Zinc and Iron-Zinc-Aluminum Intermetallic Phases at the Acceleration Voltage E_o = 16 keV

	Raw Intensity from Pure Elements (counts/sec)	
	Iron	Zinc
Initial	57,843	19,545
Final	56,898	19,169

Compound	Raw Intensity (counts/sec)		Composition (wt.%)	
	Fe	Zn	Fe	Zn
Phase zeta	4,285	18,028	6.77	93.09
	4,338	18,119	6.85	93.58
	4,323	18,063	6.83	93.28
	4,285	18,334	6.77	94.70
	4,048	18,198	6.39	93.93
Phase $delta_1$	6,072	17,615	9.64	91.33
	6,099	17,581	9.68	91.16
	6,184	17,614	9.82	91.35
	6,176	17,684	9.81	91.72
	6,145	17,644	9.76	91.50
Phase (2) ($delta_1$+4Al)	5,130	17,276	8.11	89.32
	5,267	17,729	8.34	91.74
	5,318	17,670	8.42	91.44
	5,053	17,324	7.99	89.56
	5,094	17,226	8.05	89.05

TABLE A.7

Microanalysis Data and Results for Iron-Zinc and Iron-Zinc-Aluminum Intermetallic Phases at the Acceleration Voltage E_o = 18 keV

	Raw Intensity from Pure Elements (counts/sec)	
	Iron	Zinc
Initial	81,515	29,110
Final	79,411	28,407

Compound	Raw Intensity (counts/sec)		Composition (wt.%)	
	Fe	Zn	Fe	Zn
Phase zeta	5,882	27,177	6.57	94.39
	5,827	26,781	6.50	92.97
	5,985	26,771	6.68	92.97
	5,472	26,994	6.10	93.65
	5,562	26,838	6.20	93.08
Phase $delta_1$	8,318	26,043	9.33	90.84
	8,363	25,557	9.38	89.11
	8,096	25,247	9.07	88.13
	8,416	25,103	9.43	87.50
	8,476	25,152	9.50	87.69
Phase (2) ($delta_1$+4Al)	7,291	25,387	8.15	88.29
	7,267	25,830	8.13	89.87
	7,486	25,890	8.38	90.13
	7,154	25,272	7.99	87.85
	7,155	24,985	7.98	86.83

TABLE A.8

Microanalysis Data and Results for Iron-Zinc and Iron-Zinc-Aluminum Intermetallic Phases at the Acceleration Voltage E_o = 20keV

	Raw Intensity from Pure Elements (counts/sec)	
	Iron	Zinc
Initial	97,510	38,782
Final	100,128	38,755

Compound	Raw Intensity (counts/sec)		Composition (wt.%)	
	Fe	Zn	Fe	Zn
Phase Zeta	6,902	35,708	6.43	93.26
	7,386	35,919	6.89	93.90
	7,312	35,600	6.82	93.02
	6,804	35,978	6.34	93.93
	6,424	35,851	5.98	93.51
Phase $delta_1$	10,689	34,562	10.04	90.91
	10,713	34,942	10.07	91.95
	10,809	34,792	10.16	91.56
	10,800	34,337	10.14	90.32
	11,000	33,995	10.33	89.43
Phase (2) ($delta_1$+4Al)	9,164	34,836	8.58	91.33
	9,082	34,953	8.50	91.63
	9,442	34,906	8.84	91.58
	9,097	34,400	8.50	90.14
	9,174	34,134	8.57	89.43

TABLE A.9

Microanalysis Data and Results for Iron-Zinc and Iron-Zinc-Aluminum Intermetallic Phases at the Acceleration Voltage E_o = 22 keV

	Raw Intensity from Pure Elements (counts/sec)	
	Iron	Zinc
Initial	109,148	46,699
Final	111,556	46,580

Compound	Raw Intensity (counts/sec)		Composition (wt.%)	
	Fe	Zn	Fe	Zn
Phase zeta	7,440	43,146	6.19	93.70
	7,803	43,577	6.51	94.76
	8,098	43,469	6.76	94.58
	7,392	43,343	6.15	94.13
	7,425	42,847	6.18	93.01
Phase $delta_1$	10,104	42,082	8.45	92.97
	11,242	41,901	9.43	92.81
	12,567	41,970	10.58	93.27
	12,375	41,808	10.41	92.85
	12,528	41,317	10.53	91.74
Phase (2) ($delta_1$+4Al)	9,866	41,628	8.24	91.87
	10,204	41,727	8.53	92.17
	9,771	40,945	8.14	90.27
	10,126	41,468	8.46	91.56
	10,263	40,649	8.56	89.70

TABLE A.10

Microanalysis Data and Results for Iron-Zinc-Aluminum Compound (number 5 in Table 8) at the Acceleration Voltage E_o = 18 keV

	Raw Intensity from Pure Elements (counts/sec)	
	Iron	Zinc
Initial	34,248	10,215
Final	33,986	10,138

Compound	Raw Intensity (counts/sec)		Composition (wt.%)	
	Fe	Zn	Fe	Zn
Phase 5	13,971 13,768 13,854	1,140 1,161 1,157	42.01 41.74 41.86	12.23 12.60 12.51

APPENDIX B

MICROANALYSIS DATA AND RESULTS FOR THE EQUILIBRIUM SPECIMENS

TABLE B.I

Microanalysis Data and Results for the Equilibrium Specimen FeAl-Zn

	Raw Intensity of Pure Elements (counts/sec)		
	Al	Fe	Zn
Initial	14,546	47,549	12,513
Final	14,442	47,417	12,098

Phase Examined	Raw Intensity (counts/sec)			Composition (wt.%)		
	Al	Fe	Zn	Al	Fe	Zn
Original FeAl at center of crystal	796	30867		14.70	66.77	
	733	30856		13.139	66.52	
	747	30873		13.68	66.61	
Av.				33.67*	66.33	
I	1389	14750	1436	24.77	43.06	12.98
Phase of the continuous	1232	19734	1382	20.85	42.70	12.48
layer at the interface	1264	19624	1422	21.59	43.53	12.86
with FeAl Av.				44.11*	43.09	12.80
II	1387	19634	1512	24.51	42.79	13.75
The same phase - but at	1241	19611	1515	21.53	42.45	13.77
interface with large grain	1230	19300	1490	20.98	41.73	13.54
phase Av.				44.00*	42.32	13.68
III	1134	19610	1536	19.70	42.44	13.98
Small particles of dark	1195	19567	1558	21.44	42.03	14.21
phase within large grain	1023	19434	1511	17.11	41.01	13.75
phase	1155	19543	1543	20.65	41.91	14.05
	1030	19596	1527	17.44	42.34	13.94
Av.				44.08*	41.94	13.98
IV	Backgr.	4425	10935		8.27	87.81
Phase of large grains at	"	4189	10987		8.15	88.28
the interface with Phase	"	4270	11019		8.31	88.56
I	"	4212	10921		8.19	87.72
	"	4241	11003		8.26	88.39
Av.				3.62*	8.23	88.15

* Al content obtained by difference

Table B.1 (continued)

	Raw Intensity of Pure Elements (counts/sec)		
	Al	Fe	Zn
Initial	15865	54863	14783
Final	15402	54216	14391

Phase Examined	Raw Intensity (counts/sec)			Composition (wt.%)		
	Al	Fe	Zn	Al	Fe	Zn
FeAl at the interface with Fe_2Al_5 layer at the vicinity of the triple point (FeAl-Fe_2Al_5-δ_1)	527	37782	1641	10.21	69.72	12.43
	486	37217	1549	9.96	68.64	11.72
	469	37329	1531	9.84	68.87	11.59
	493	37043	1598	10.02	68.32	12.11
	518	37836	1629	10.13	69.83	12.36
Av.				18.89*	69.07	12.04

* Al obtained by a difference.

TABLE B.2

Microanalysis Data and Results for the FeAl-Zn(Al) Equilibrium Specimen

	Raw Intensity of Pure Elements (counts/sec)		
	Al	Fe	Zn
Initial	16989	55480	15611
Final	16076	54853	14850

Phase Examined	Raw Intensity (counts/sec)			Composition (wt.%)		
	Al	Fe	Zn	Al	Fe	Zn
Original FeAl	582	36319		9.41	66.24	
	616	36453		10.04	66.61	
	622	36419		10.14	66.57	
Av.				33.53*	66.47	
I						
Phase of continuous layer	1164	23081	1794	17.80	42.44	13.31
at FeAl	1131	22805	1853	17.26	41.85	13.71
	1129	22987	1779	17.10	42.19	13.17
	1068	23219	1948	16.64	42.52	14.40
	1107	23108	1860	17.02	42.39	13.76
Av.				44.07*	42.27	13.66
II	1319	21633	1869	21.23	40.27	13.86
Small particles of dark	1331	21752	1949	21.86	40.53	14.40
phase in zinc matrix at	1257	21676	1892	20.22	40.24	13.96
zinc interface	1332	21530	1817	21.25	40.09	13.46
	1227	22776	1851	20.19	40.30	13.69
Av.				45.85*	40.28	13.87
III	Backgr.	5116	12864		8.59	87.99
Phase of large grains at	"	5089	12891		8.51	88.04
interface with Phase I	"	5155	12923		8.64	88.16
	"	4938	13088		8.27	89.09
	"	4986	12970		8.35	88.28
Av.				3.22*	8.47	88.31
IV	1348	22577	1987	22.50	41.14	14.65
Phase II at triple point	1329	22302	1962	22.20	41.54	14.48
with zinc and Phase III	1290	22539	1951	21.03	41.09	14.42
Av.				44.24*	41.25	14.51

TABLE B.2 - continued

Phase Examined	Raw Intensity (counts/sec)			Composition (wt.%)		
	Al	Fe	Zn	Al	Fe	Zn
V	Backgr.	4815	12918		8.24	88.15
Phase II at triple point	"	4989	12871		8.36	87.01
with zinc and Phase IV	"	4999	12953		8.38	88.22
Av.				3.89*	8.32	87.79
VI Zinc at triple point	Unreliable results					

* Al content obtained by difference

TABLE B.3

Microanalysis Data and Results for the $FeAl_2$-Zn Equilibrium Specimen

	Raw Intensity of Pure Elements (counts/sec)		
	Al	Fe	Zn
Initial	15628	33086	8174
Final	15512	32910	8227

Phase Examined	Raw Intensity (counts/sec)			Composition (wt.%)		
	Al	Fe	Zn	Al	Fe	Zn
I						
Large grey grains at zinc interface	Backgr.	2947	7333		8.13	89.96
	"	3003	7375		8.29	90.51
	"	3048	7376		8.42	90.55
Av.				1.38*	8.28	90.34
II						
Small particles of dark phase in zinc matrix, at zinc interface	1190	13494	962	17.76	40.39	12.37
	1206	13668	971	18.03	40.36	12.41
	1210	13305	993	18.04	39.57	12.51
Av.				47.47*	40.10	12.43
III						
Phase II at triple point with zinc and Phase I	1230	14044	1041	18.63	41.50	13.54
	1289	14020	1050	18.63	41.37	13.65
	1254	14051	1106	18.66	41.65	14.37
Av.				44.65*	41.50	13.85
IV						
Phase I at triple point	Backgr.	3051	7286		8.45	89.37
	"	3097	7251		8.59	88.98
	"	3103	7267		8.61	89.16
Av.				2.28*	8.55	89.17
V						
Zinc at triple point	Unreliable Results					

* Al content obtained by difference

TABLE B.4

Microanalysis Data and Results for the $FeAl_2$-Zn(Al) Equilibrium Specimen

	Raw Intensity of Pure Elements (counts/sec)		
	Al	Fe	Zn
Initial	16054	35627	9557
Final	15896	35478	9494

Phase Examined	Raw Intensity (counts/sec)			Composition (wt.%)		
	Al	Fe	Zn	Al	Fe	Zn
Original $FeAl_2$	1682	17857		28.33	51.46	
	1659	17817		27.95	50.32	
	1671	18164		28.18	51.33	
Av.				48.97*	51.03	
I	1291	15236	415	20.48	43.36	4.60
Regularly shaped dark	1274	15061	451	20.17	42.83	5.05
phase at zinc interface	1318	15234	451	21.20	43.31	5.05
Av.				41.94*	43.16	4.90
II	1109	15411	1075	19.61	43.84	11.65
Irregularly shaped dark	1078	15435	1064	19.53	43.91	11.50
phase at zinc interface	1003	15409	1060	19.59	43.81	11.46
Av.				44.62*	43.85	11.53

* Al content obtained by difference

TABLE B.5

Microanalysis Data and Results for the Fe_2Al_5-Zn Equilibrium Specimen

	Raw Intensity of Pure Elements (counts/sec)		
	Al	Fe	Zn
Initial	16638	33612	9916
Final	16424	33509	9691

Phase Examined	Raw Intensity (counts/sec)			Composition (wt.%)		
	Al	Fe	Zn	Al	Fe	Zn
I	1218	13769	1233	20.31	42.08	13.23
Fe_2Al_5 at triple point with	1234	13698	1336	20.42	41.85	14.33
zinc and large grain phase	1230	13728	1333	20.40	41.94	14.30
Av.				44.10*	41.95	13.95
II	Backgr.	2667	8043		7.36	90.68
Large grain phase at	"	2792	8848		7.70	88.70
triple point	"	2672	8879		7.36	88.97
Av.				3.08*	7.47	89.45
III	Unreliable results					
Zinc at triple point						

* Al content obtained by difference

TABLE B.6

Microanalysis Data and Results for the Fe_2Al_5-Zn(Al) Equilibrium Specimen

	Raw Intensity of Pure Elements (counts/sec)		
	Al	Fe	Zn
Initial	14241	37730	10031
Final	13972	37760	1135

Phase Examined	Raw Intensity (counts/sec)			Composition (wt.%)		
	Al	Fe	Zn	Al	Fe	Zn
Dark phase at the interface with zinc	1106	15443	1203	19.31	40.11	12.31
	1129	15734	1177	19.63	40.89	12.05
	1130	15609	1181	19.63	40.56	12108
Av.				47.34*	40.52	12.14

* Al content obtained by difference

TABLE B.7

Microanalysis Data and Results for the $FeAl_3$-Zn(Al) Equilibrium Specimen

	Raw Intensity of Pure Elements (counts/sec)		
	Al	Fe	Zn
Initial	15316	34696	13565
Final	15452	34784	13398

Phase Examined	Raw Intensity (counts/sec)			Composition (wt.%)		
	Al	Fe	Zn	Al	Fe	Zn
Original $FeAl_3$	3345	14707		48.21	40.95	
	3284	15127		47.56	42.15	
	3297	14702		47.77	40.94	
Av.				58.66*	41.34	
1	1741	14721	831	24.31	40.88	6.53
Phase partially separated from $FeAl_3$ at zinc interface	1659	14312	641	23.69	39.60	5.04
	1804	14091	867	24.87	38.91	6.81
	1599	14008	1062	23.08	38.62	8.34
	1783	14194	789	24.52	39.22	6.20
Av.				53.98*	39.44	6.58

* Al content obtained by difference

APPENDIX C

RESULTS OF X-RAY DIFFRACTION ANALYSIS

TABLE C.1

The Diffraction Lines of the Powdered Compound $FeAl_2$ for $5^{\circ} < \theta < 25^{\circ}$

2θ	Spacing of d			Intensity (counts/sec)
	K_{α_1}	K_{α_2}	K_{α}	
19.07			4.670	60
19.67			4.51	20
21.15			4.20	42
22.29			3.988	18
22.44	3.958			20
22.50		3.958		17
23.23			3.828	19
24.41	3.643			40
24.48		3.642		50
24.93	3.568			61
25.00		3.567		30
25.35			3.513	40
26.82	3.321			21
26.91		3.318		26
27.00	3.299			10
27.10		3.295		19
32.62	2.742			12
32.71		2.742		10
38.90	2.313			20
39.00		2.313		15
41.46	2.176			28
41.57		2.176		11
42.81	2.110			108
42.90		2.111		110
42.99	2.102			116
43.10		2.102		68

Table C.1 (continued)

2θ	Spacing d(Å)			Intensity (counts/sec)
	K_{α_1}	K_{α_2}	K_{α}	
43.66	2.08			67
43.56		2.081		67
43.76	2.066			178
43.87		2.067		140
44.15	2.049			98
44.24		2.050		92
44.56	2.031			80
44.68		2.031		71
44.91	2.016			46
45.02		2.016		50

TABLE C.2

The Diffraction Lines of the Powdered Compound Fe_2Al_5 for $5^\circ < \theta < 25^\circ$

2θ	Spacing d(Å)			Intensity (counts/sec
	K_{α_1}	K_{α_2}	K_α	
18.09	4.899			80
18.14		4.898		80
23.33	3.809			180
23.38		3.811		140
27.90	3.195			271
28.95		3.197		266
38.02	2.364			39
38.12		2.364		35
42.70	2.115			322
42.80		2.116		218
42.98	2.102			242
43.08		2.097		142
43.93	2.059			233
44.02		2.055		299
47.00		1.936		46
47.85		1.904		21

TABLE C.3

The Diffraction Lines of the Powdered Compound $FeAl_3$ for $5^\circ < \theta < 25^\circ$

2θ	Spacing d (Å)			Intensity (counts/sec)
	K_{α_1}'	K_{α_2}	K_α	
18.08			4.906	60
21.98			4.043	25
22.44	3.958			15
22.50		3.958		21
23.26	3.820			70
23.32		3.820		57
24.14	3.683			15
24.19		3.685		20
25.10	3.533			60
25.20		3.532		45
26.75	3.329			13
26.82		3.329		11
27.32	3.261			10
27.39		3.261		12
27.80	3.206			110
27.86		3.207		123
37.97	2.367			11
38.09		2.366		10
38.31			2.349	5
39.83	2.261			9
39.94		2.260		15
41.83			2.159	12
42.60	2.120			174
42.70		2.121		172
43.17	2.093			65
43.33		2.091		31
43.80	2.065			170
43.90		2.065		99

Table C.3 (continued)

2θ	Spacing d(Å)			Intensity (counts/sec)
	K_{α_1}	K_{α_2}	K_{α}	
44.04			2.056	95
44.41			2.039	68
44.95		2.019		85
46.73	1.942			22
46.87		1.941		21
47.50	1.912			11
47.62		1.912		15

TABLE C.4

The Diffraction Lines Obtained from the Stripped Galvanized Samples Produced at Conditions Indicated

Bath 1, 10 sec.

2θ	Spacing (Å)			Intensity (counts/sec)
	K_{α_1}	K_{α_2}	K_{α}	
13.99			6.33	40
49.97	3.187			15
28.64		3.187		18
41.67			2.167	15
44.73	2.024			60
44.81		2.025		73

TABLE C.5

The Diffraction Lines Obtained from the Stripped Galvanized Samples Produced at Conditions Indicated

Bath 1, 1 min.

2θ	Spacing d(Å)			Intensity (counts/sec)
	K_{α_1}	K_{α_2}	K_{α}	
23.33			3.812	24
23.41			3.799	24
27.82	3.204			69
27.93		3.200		38
42.41	2.129			27
42.48		2.131		24
44.73	2.024			35
44.81		2.025		12

TABLE C.6

The Diffraction Lines Obtained from the Stripped Galvanized Samples Produced at Conditions Indicated

Bath 1, 3 min.

2θ	Spacing d(Å)			Intensity (counts/sec)
	K_{α_1}	K_{α_2}	K_{α}	
27.90	3.195			32
27.96		3.196		15
41.05			2.198	30
41.76	2.161			23
41.82		2.163		18
42.29	2.135			178
42.36		2.137		152
44.77			2.024	20

TABLE C.7

The Diffraction Lines Obtained from the Stripped Galvanized Samples Produced at Conditions Indicated

Bath I, 10 min.

2θ	Spacing d(A)			Intensity (counts/sec)
	K_{α_1}	K_{α_2}	K_{α}	
32.64	2.741			15
32.73		2.740		21
36.33			2.472	700
39.02	2.306			568
39.10		2.307		290
41.09			2.196	140
41.49			2.176	52
41.87	2.155			100
41.98		2.155		80
42.27			2.133	550
43.27			2.090	~700
54.35	1.685			410
54.48		1.627		198

TABLE C.8

The Diffraction Lines Obtained from the Stripped Galvanized Samples Produced at Conditions Indicated

Bath 11, 10 sec.

2θ	Spacing d(Å)			Intensity (counts/sec)
	K_{α_1}	K_{α_2}	K_{α}	
13.86			6.38	21
14.18			6.245	25
15.36			5.768	21
21.25			4.181	10
23.35			3.809	13
24.12			3.689	16
27.87			3.201	30
44.70	2.024			91
44.80		2.026		64

TABLE C.9

The Diffraction Lines Obtained from the Stripped Galvanized Samples Produced at Conditions Indicated

Bath II, 1 min.

2θ	Spacing d(Å)			Intensity (counts/sec)
	K_{α_1}	K_{α_2}	K_{α}	
13.84	6.393			33
13.88		6.390		32
22.35			3.977	30
23.33			3.812	14
27.89			3.198	20
28.10			3.175	11
42.48			2.127	24
43.82	2.064			20
44.00		2.061		11
44.68	2.026			25
44.75		2.028		30
46.70			1.945	14

TABLE C.10

The Diffraction Lines Obtained from the Stripped Galvanized Samples Produced at Conditions Indicated

Bath II, 3 min.

2θ	Spacing d(Å)			Intensity (counts/sec)
	K_{α_1}	K_{α_2}	K_{α}	
13.98			6.334	28
14.27			6.206	18
22.36	3.972			40
22.41		3.973		53
23.38	3.801			55
23.45		3.799		55
27.86	3.199			62
27.95		3.197		53
42.47	2.126			70
42.56		2.127		70
43.63			2.074	25
43.87	2.062			30
44.00		2.061		30
44.75	2.023			13
44.84		2.024		13
47.92			1.898	10

TABLE C.11

The Diffraction Lines Obtained from the Stripped Galvanized Samples Produced at Conditions Indicated

Bath II, 10 min.

2θ	Spacing d(Å)			Intensity (counts/sec)
	K_{α_1}	K_{α_2}	K_{α}	
22.37	3.970			42
22.44		3.968		26
23.35			3.809	11
48.07	1.890			12
48.14		1.893		14

TABLE C.12

The Diffraction Lines Obtained from the Stripped Galvanized Samples Produced at Conditions Indicated

Bath II, 30 min.

40.77			2.213	10

TABLE C.13

The Diffraction Lines Obtained from the Stripped Galvanized Samples Produced at Conditions Indicated

Bath III, 10 sec.

2θ	Spacing d(Å)			Intensity (counts/sec)
	K_{α_1}	K_{α_2}	K_{α}	
23.40			3.801	19
26.75	3.329			1
26.84		3.327		13
27.85			3.203	27
43.77			2.063	24
44.66	2.027			90
44.79		2.026		70

TABLE C.14

The Diffraction Lines Obtained from the Stripped Galvanized Samples Produced at Conditions Indicated

Bath III, 1 min.

16.80			5.277	10
18.01			4.922	15
23.37			3.806	23
27.85	3.200			52
27.93		3.199		19
42.40	2.130			45
42.50		2.130		29
42.72			2.116	12
43.76	2.066			22
43.91		2.065		12
44.68	2.026			14
44.78		2.027		14

TABLE C.15

The Diffraction Lines Obtained from the Stripped Galvanized Samples Produced at Conditions Indicated

Bath III, 3 min.

2θ	Spacing d(Å)			Intensity (counts/sec)
	K_{α_1}	K_{α_2}	K_{α}	
18.00			4.927	14
23.32			3.814	135
27.81			3.207	122
42.40	2.130			202
42.50		2.130		112
42.73			2.116	133
43.60			2.075	95
43.83			2.065	188
44.65	2.027			30
46.72	1.942			55
46.82		1.943		42
47.18	1.924			28
47.22		1.928		28

TABLE C.16

The Diffraction Lines Obtained from the Stripped Galvanized Samples Produced at Conditions Indicated

Bath III, 10 min.

2θ	Spacing d(Å)			Intensity (counts/sec)
	K_{α_1}	K_{α_2}	K_{α}	
14.30			6.193	10
23.37	3.819			8
23.39		3.809		10
27.85	3.200			42
27.94		3.198		20
42.47	2.126			45
42.59		2.126		10
42.84	2.109			97
42.90		2.111		65
43.92	2.059			41
44.08		2.057		9
46.82			1.940	25

TABLE C.17

The Diffraction Lines Obtained from the Stripped Galvanized Samples Produced at Conditions Indicated

Bath III, 30 min.

2θ	Spacing d(Å)			Intensity (counts/sec)
	K_{α_1}	K_{α_2}	K_{α}	
14.29			6.197	33
23.27	3.819			20
23.37		3.812		30
24.94			3.567	12
25.09			3.549	15
44.81			2.022	30
47.18	1.924			28
47.26		1.926		21

TABLE C.18

The Diffraction Lines Obtained from the Stripped Galvanized Samples Produced at Conditions Indicated

Bath IV, 10 sec.

2θ	Spacing d(Å)			Intensity (counts/sec)
	K_{α_1}	K_{α_2}	K_{α}	
22.58			3.937	20
32.70			2.738	13
34.95	2.564			18
35.00		2.567		21
40.91			2.205	20
43.20	2.092			12
43.30		2.093		15
44.75	2.023			66
44.86		2.023	47	

TABLE C.19

The Diffraction Lines Obtained from the Stripped Galvanized Samples Produced at Conditions Indicated

Bath IV, 1 min.

2θ	Spacing d(Å)			Intensity (counts/sec)
	K_{α_1}	K_{α_2}	K_{α}	
23.37			3.806	17
27.79	3.207			22
27.88		3.205		15
41.05			2.198	16
42.41	2.129			18
42.53		2.129		20
43.75	2.067			25
43.83		2.068		36
43.96			2.059	22
44.69	2.026			30
44.77		2.027		28
44.86			2.020	22
45.75	1.981			8
45.83		1.983		19
47.80			1.902	20

TABLE C.20

The Diffraction Lines Obtained from the Stripped Galvanized Samples Produced at Conditions Indicated

Bath IV, 3 min.

2θ	Spacing d(Å)			Intensity (counts/sec)
	K_{α_1}	K_{α_2}	K_{α}	
23.30			3.817	82
27.77	3.209			170
27.84		3.209		176
38.03			2.366	18
42.43	2.127			210
42.56		2.128		161
42.70	2.115			375
42.80		2.116		345
43.26			2.091	35
43.79	2.065			142
43.89		2.066		194
44.72			2.026	29
46.73	1.942			112
46.87		1.941		69
47.64			1.908	23

TABLE C.21

The Diffraction Lines Obtained from the Stripped Galvanized Samples Produced at Conditions Indicated

Bath IV, 10 min.

2θ	Spacing d(Å)			Intensity (counts/sec)
	K_{α_1}	K_{α_2}	K_{α}	
14.06			6.298	21
14.19			6.241	27
18.08	4.902			11
18.13		4.900		11
23.40			3.801	48
27.84	3.201			84
27.93		3.199		28
38.11			2.361	28
42.45			2.126	140
42.79			2.113	230
43.19	2.092			27
43.36		2.090		28
43.66	2.071			60
43.75		2.072		80
43.80	2.065			105
43.87		2.067		105
46.73	1.942			70
46.85		1.942		39
51.52	1.772			13
51.75		1.769		12

TABLE C.22

The Diffraction Lines Obtained from the Stripped Galvanized Samples Produced at Conditions Indicated

Bath IV, 30 min.

very faint iron		44.79	10

TABLE C.23

The Diffraction Lines Obtained from the Stripped Galvanized Samples Produced at Conditions Indicated

Bath V, 10 sec.

2θ	Spacing d(Å)			Intensity (counts/sec)
	K_{α_1}	K_{α_2}	K_{α}	
14.20			6.236	10
23.26			3.824	16
25.04	3.553			25
25.11		3.552		15
27.85	3.200			48
27.90		3.203		17
39.81	2.262			7
39.86		2.265		2
41.37	2.180			18
41.46		2.181		5
42.58			2.123	20
44.68	2.026			42
44.79		2.026		23
46.80	1.939			18
46.88		1.941		4
52.06	1.755			8
52.15		1.756		2
54.78			1.704	11
57.80	1.593			10
57.84		1.596		11
65.05			1.433	600

TABLE C.24

The Diffraction Lines Obtained from the Stripped Galvanized Samples Produced at Conditions Indicated

Bath V, 1 min.

2θ	Spacing d(Å)			Intensity (counts/sec)
	K_{α_1}	K_{α_2}	K_{α}	
17.98			4.933	18
23.10	3.847			25
23.14		3.849		18
23.20	3.830			25
23.26		3.830		16
27.76	3.210			102
27.80		3.214		101
42.60	2.120			236
42.70		2.121		218
43.78	2.066			119
43.89		2.066		70
44.65			2.029	6
46.61	1.946			40
46.75		1.946		17
47.77	1.902			10
47.85		1.904		8

TABLE C.25

The Diffraction Lines Obtained from the Stripped Galvanized Samples Produced at Conditions Indicated

Bath V, 3 min.

2θ	Spacing d(Å)			Intensity (counts/sec)
	K_{α_1}	K_{α_2}	K_{α}	
14.20			6.236	10
20.91			4.248	12
22.05			4.031	22
23.20			3.833	42
27.74			3.215	121
32.46	2.755			4
32.52		2.757		16
35.96	2.495			18
36.08		2.493		17
39.70			2.27	13
41.35			2.183	19
42.58	2.121			500
42.64		2.123		520
43.14	2.095			190
43.27		2.094		106
43.70	2.069			130
43.79		2.070		155
44.91			2.018	11
46.66			1.946	63

TABLE C.26

The Diffraction Lines Obtained From the Stripped Galvanized Samples Produced at Conditions Indicated

Bath V, 10 min.

2θ	Spacing d(Å)			Intensity (counts/sec)
	K_{α_1}	K_{α_2}	K_{α}	
23.20	3.830			43
23.26		3.830		23
24.10	3.689			8
24.15		3.691		10
27.74	3.213			106
27.82		3.212		22
28.28			3.155	10
41.18	2.190			10
41.27		2.191		10
42.43	2.128			175
42.63		2.124		380
43.14	2.095			18
43.21		2.097		24
43.71	2.069			162
43.80		2.070		162
44.69			2.027	5
46.60	1.947			78
46.75		1.946		58
51.48	1.773			16
51.58		1.775		16

TABLE C.27

The Diffraction Lines Obtained From the Stripped Galvanized Samples Produced at Conditions Indicated

Bath V, 30 min.

2θ	Spacing d(Å)			Intensity (counts/sec)
	K_{α_1}	K_{α_2}	K_{α}	
22.47	3.953			13
22.55		3.949		13
23.26			3.824	73
27.79			3.210	115
41.74	2.162			12
41.79		2.165		12
42.55	2.122			180
42.68		2.121		330
43.73	2.068			250
43.82		2.069		228
46.64	1.945			71
46.73		1.947		81
47.71	1.904			20
47.76		1.907		25
41.66	1.767			26
51.83		1.766		18
60.36	1.532			22
60.40		1.535		24

REFERENCES

1. M. Hansen and K. Anderko, Constitution of Binary Alloys, New York, McGraw-Hill, 1958.

   F. A. Shunk, Constitution of Binary Alloys, Second Supplement, New York, McGraw-Hill, 1969.

2. H. H. Stadelmaier and W. K. Hardy, Metall., 14, 778-9 (1960).

3. H. H. Stadelmaier, and R. K. Bridgers, Metall., 15, 761-3 (1961).

4. R. P. Elliot, Constitution of Binary Alloys, First Supplement, New York, McGraw-Hill, pp. 433-4, 1965.

5. D. Horstmann and F. K. Peters, Arch. f. Eisenhuttenu., 40, 621-6, (1969).

6. D. Horstmann, Proc. Fourth Intern. Conf. on Hot Dip Galvanizing, Milan, 1956, London, ZDA, 1957, pp. 29-51.

7. H. Warlimont, Z. Metallkde, 60, 195 (1969).

8. A. Osawa, Sci. Rep. Tohoku Imp. Univ., 22 [i], 803 (1933).

9. A. J. Bradley and A. Taylor, J. Inst. Metals, 66, 53-65 (1940).

10. E. H. Rennhack, Transactions of the Met. Soc. AIME, 221, 775-779 (1961).

11. D. I. Cameron, Proc. Sixth Intern. Conf. on Hot Dip Galvanizing, Interlaken, 1961, London, ZDA, pp. 301-314.

12. O. Caloni, A. Ferrari and F. Gatto, Ric. Sci., 36, 1269-73 (1966).

13. O. Caloni and A. Ferrari, Metal. Ital. Atti Notizie, Bol. AIM, 22 (2/3), 45-6 (1967).

14. D. Horstmann and F. K. Peters, Arch. f. Eisenhuttenw., 40, 621-6 (1969).

15. D. I. Cameron, Lysaght Research Report No. 133, (1959).

16. D. Horstmann, F. K. Peters, Proc. Ninth Intern. Conf. on Hot Dip Galvanizing, Dusseldorf, 1970, London, ZDA, pp. 75-106.

17. J. J. Sebisty, A Survey of Literature on Hot Dip Galvanizing, 1950-1955, Canada Department of Mines and Technical Surveys Mines Branch, Research Report No. PM-202 (1956).

18. R. W. Thorley, Factors Affecting the Production and Properties of Hot Dipped Galvanized Coatings, Report RRA 868, British Non-Ferrous Metals Research Association (1950).

19. D. Horstmann, The Influence of Impurities in Iron on Attack by Molten Zinc, Proc. Fourth Intern. Galv. Conf., ZDA, London (1956).

20. J. J. Sebisty, R. H. Palmer, Hot Dip Galvanizing with Less Common Bath Additions, Proc. Seventh Intern. Galvan. Conf., ZDA, London (1964).

21. J. J. Sebisty, R. H. Palmer, Galvanizing of Low-Alloy High-Strength Steels, Canada Department of Energy, Mines and Resources, Mines Branch, Physical Metallurgy Division, Internal Report PM-M-66-18 (1966).

22. H. Bablik, Galvanizing (Hot Dip), London, E., and F. N. Spon, 3rd Edition, 1950.

23. H. Bablik, F. Gotzl, R. Kukaczka, The Causes of the Retarding Effect of Aluminum in Galvanizing Bath, Werkstoffe Korrosion, 2, (1951).

24. M. L. Hughes, The Influence of Aluminum in Hot Dip Galvanizing, JISI, 166, 77-84 (1950).

25. M. L. Hughes, Proc. of the Intern. Conf. on Hot Dip Galvanizing, held at Copenhagen, 17-21 July, 1950, ZDA, Oxford (1951), 31-49.

26. M. A. Haughton, Proc. of the Second Intern. Conf. on Hot Dip Galvanizing Dusseldorf, 1952, ZDA, Oxford (1953), 1-25).

27. D. Horstmann, Arch. Eisenhuttenw., 297-302 (1956).

28. D. Horstmann, Proc. of the Seventh Intern. Conf. on Hot Dip Galv., Paris, 1964, ZDA, London (1967), 146.

29. D. I. Cameron and M. K. Ormay, Proc. of the Sixth Intern. Conf. on Hot Dip Galv., Interlaken, 1961, ZDA, London (1962), 276-316.

30. A. R. Borzillo and W. C. Hahn Jr., Trans. ASM 62, 729-739 (1969).

31. J. S. Kirkaldy, Can. J. Phys., 36, 917-925 (1958).

32. W. Jost, Diffusion in Solids, Liquids and Gases, Academic Press Inc., New York, 69-78 (1952).

33. J. B. Clark, F. N. Rhines, Trans. ASM, 51, 199 (1959).

34. J. S. Kirkaldy, D. G. Fedak, Trans. TMS-AIME, 224, 290 (1962).

35. J. S. Kirkaldy, L. C. Brown, Can. Met. Quart., 2, 89 (1965).

36. C. W. Taylor, M. A. Dayanada and R. E. Grace, Met. Trans., 1, 127 (1970).

37. C. Wagner, J. Electrochem. Soc., 103, 571 (1956).

38. D. E. Coates, J. S. Kirkaldy, Trans. ASM, 62, 427 (1969).

39. D. E. Coates, Ph.D. Thesis, McMaster University, (1970).

40. J. S. Kirkaldy, Ternary Diffusion and its Relationship to Oxidation and Sulfidation, in Oxidation of Metals and Alloys, Ed. D. L. Douglass, ASM, 1971.

41. J. S. Kirkaldy, Can. Met. Quart., 8, 35 (1969).

42. W. Köster, Metallurgia, December, 1969, 219.

43. J. S. Kirkaldy, Progress Report No. 18 to AISI, September, 1970.

44. E. Gebhoard, Deitschrift fur Metallkund, 206-211 (1953).

45. ASTM X-Ray Data File, No. 1-1228.

46. G. Edmunds, Trans. AIME, 263-277 (1944).

47. B. D. Cullity, Elements of X-Ray Diffraction, Addison-Wesley, Reading, Mass., 1956, p. 269.

48. F. J. Welcher, ed., Standard Methods of Chemical Analysis, IIIA, Chapter 11, (1966).

49. A. J. C. Wilson, Proc. Phys. Soc., (London), 78, 249 (1961).

50. E. F. Kaelble, Handbook of X-rays, McGraw-Hill, 1967, 9-1 to 9-40.

51. R. Castaing, Ph.D. Thesis, Univ. of Paris, 1951.

52. L. S. Birks, Electron Probe Microanalysis, Wiley-Interscience, New York, 1963.

53. H. H. Pattee, V. E. Cosslett and A. Engstrom (eds.), X-Ray Optics and X-Ray Microanalysis, Academic Press, New York (1963).

54. T. O. Ziebold, R. E. Ogilvie, Anal. Chem., 36, 323 (1964).

55. P. Duncumb, P. K. Shields, The Electron Microprobe, J. Wiley, 1966.

56. D. R. Beaman, Anal. Chem., 39, 418 (1967).

57. K. F. J. Heinrich, Advan. X-Ray Anal., 11, 40 (1968).

58. O. Caloni, A. Ferrari, Atti Notiziel, Associazione, Italiana di Metallurgia, 22, 45-46 (1967).

59. R. H. Palmer, H. R. Thresh, Electron-Probe Microanalysis of Alloyed Galvanized Coatings, Dept. of Energy, Mines and Resources, Mines Branch, Ottawa, Phys. Metall. Div., Internal Report PM-R-69-12 (1969).

60. Reference 53, p. 391.

61. A. Dalvi, The Electron Probe Microanalyser, Dept. Metal. and Mat. Sci., McMaster University, 1969.

62. W. Köster and T. Gödecke, Z. Metallkunde, Bd. 61 (1970), H.9, 649-658.

63. J. Burke, The Kinetics of Phase Transformation in Metals, New York, Pergamon Press, Chapter 5.

64. V. Z. Bugakov, Diffusion in Metals and Alloys, Available from U.S. Department of Commerce.

65. V. R. Ryabov, Vasil'Yeu Lozovskaya, Fiz. Metal. Metalloved., No. 4, 98-103 (1969).

66. J. S. Kirkaldy, L. C. Brown, Can. Met. Quart., 2, 89-117 (1963).

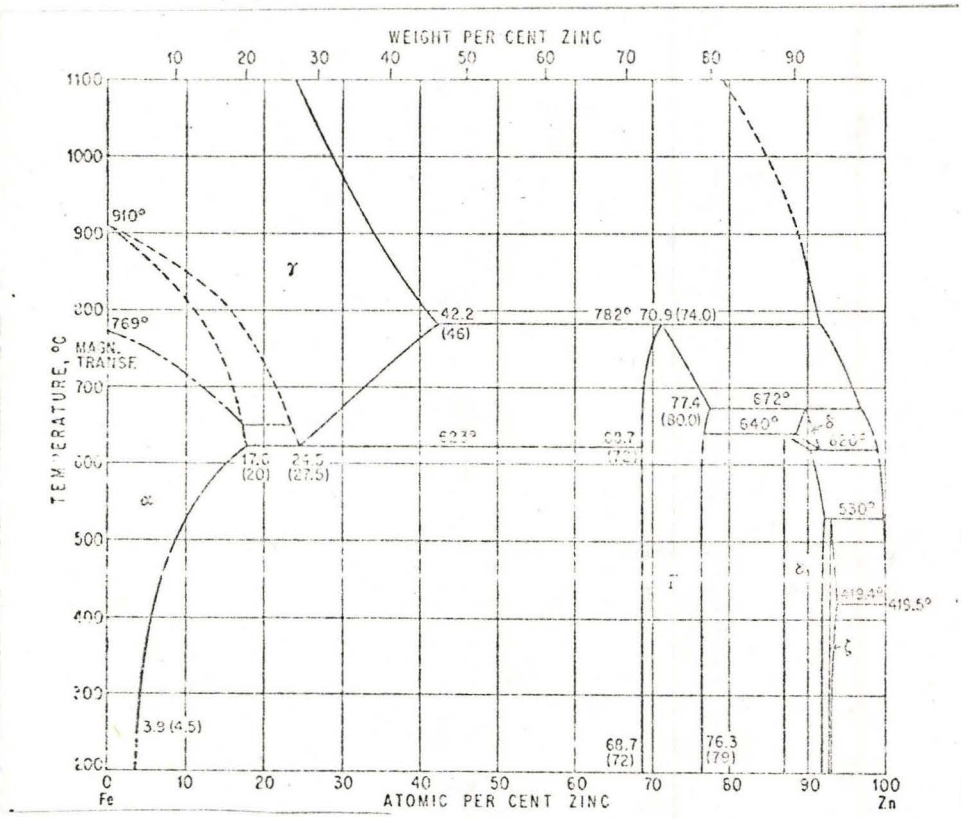

Figure 1. The iron-zinc binary system, after Hansen[1].

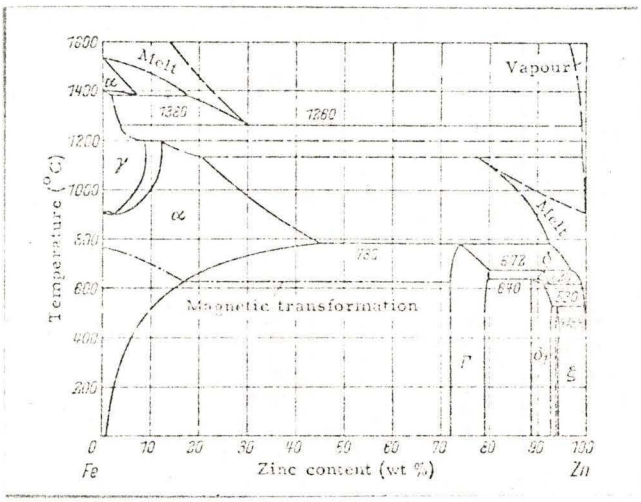

Figure 2. The iron-zinc binary system after Horstmann and Peters[5].

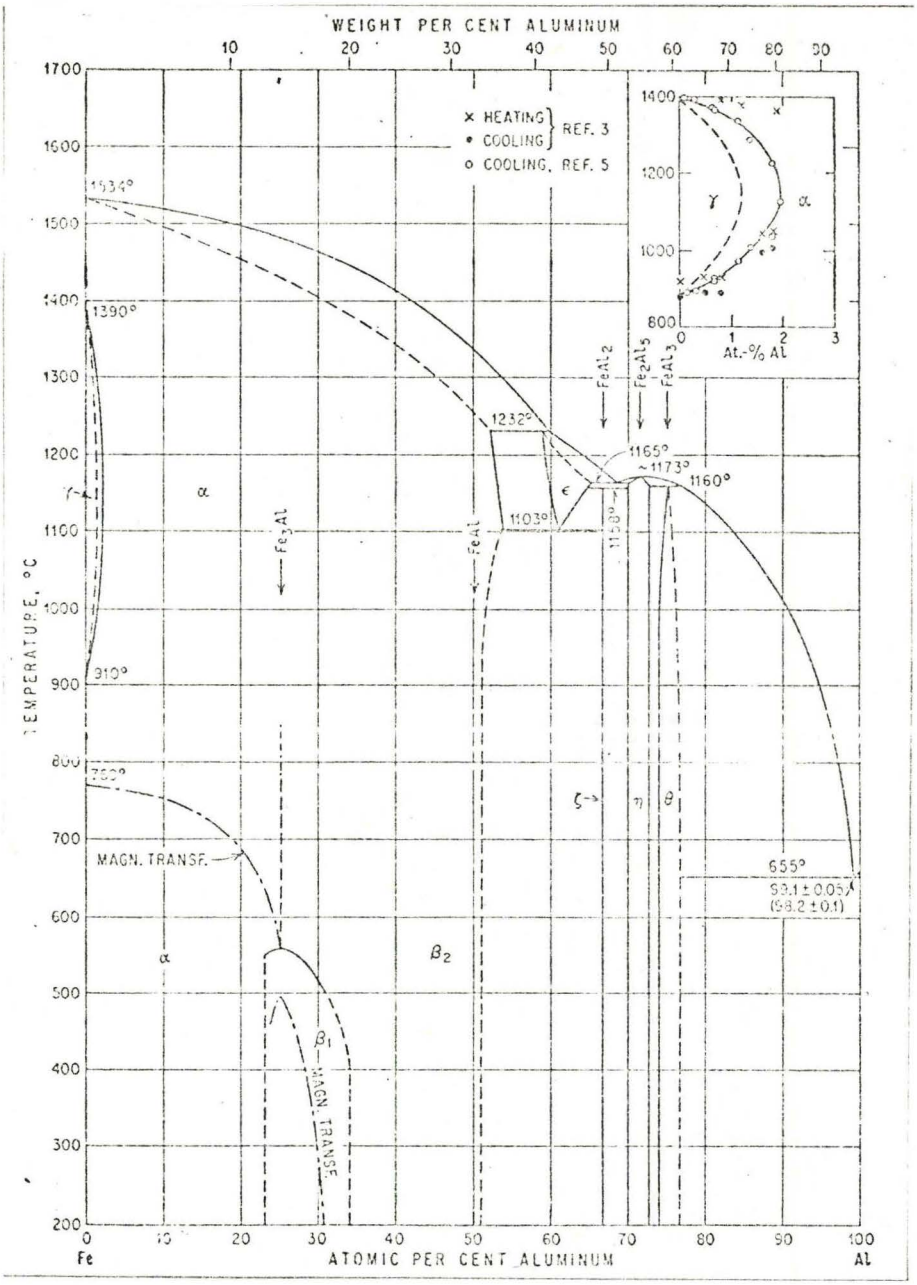

Figure 3. The iron-aluminum binary system after Hansen[1].

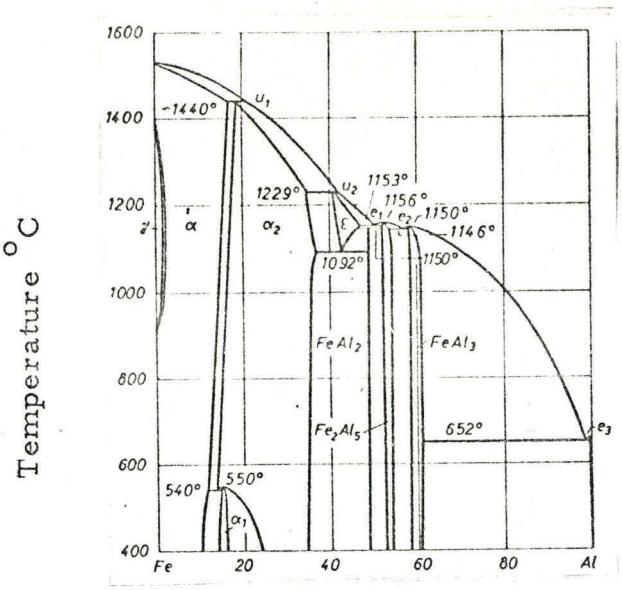

Figure 4. The iron-aluminum binary system after Shunk[49].

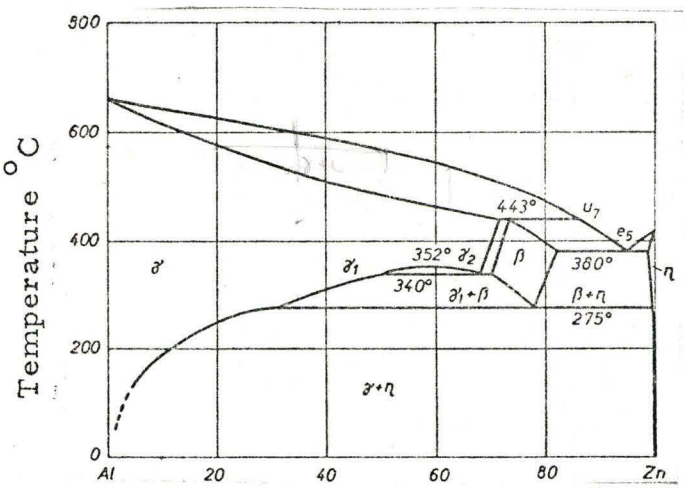

Figure 5. The aluminum-zinc binary system after Shunk[49].

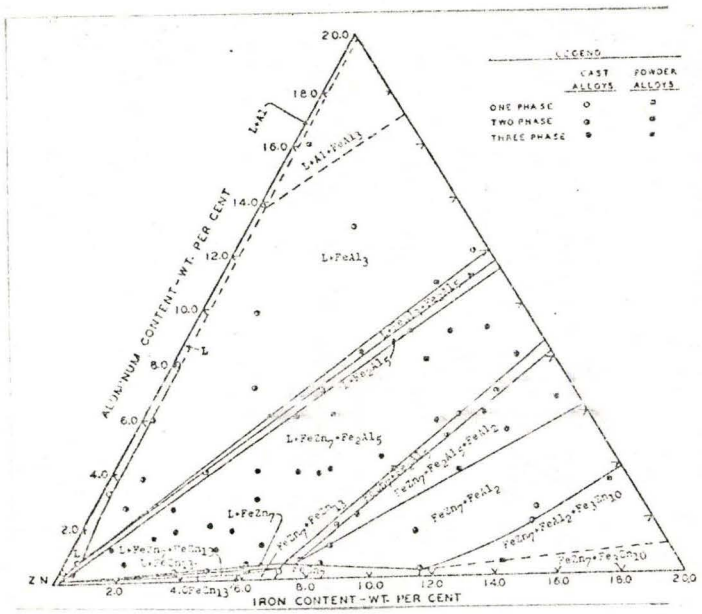

Figure 6. Partial isothermal section at 450°C for the Zn-Fe-Al system after Rennhack(10).

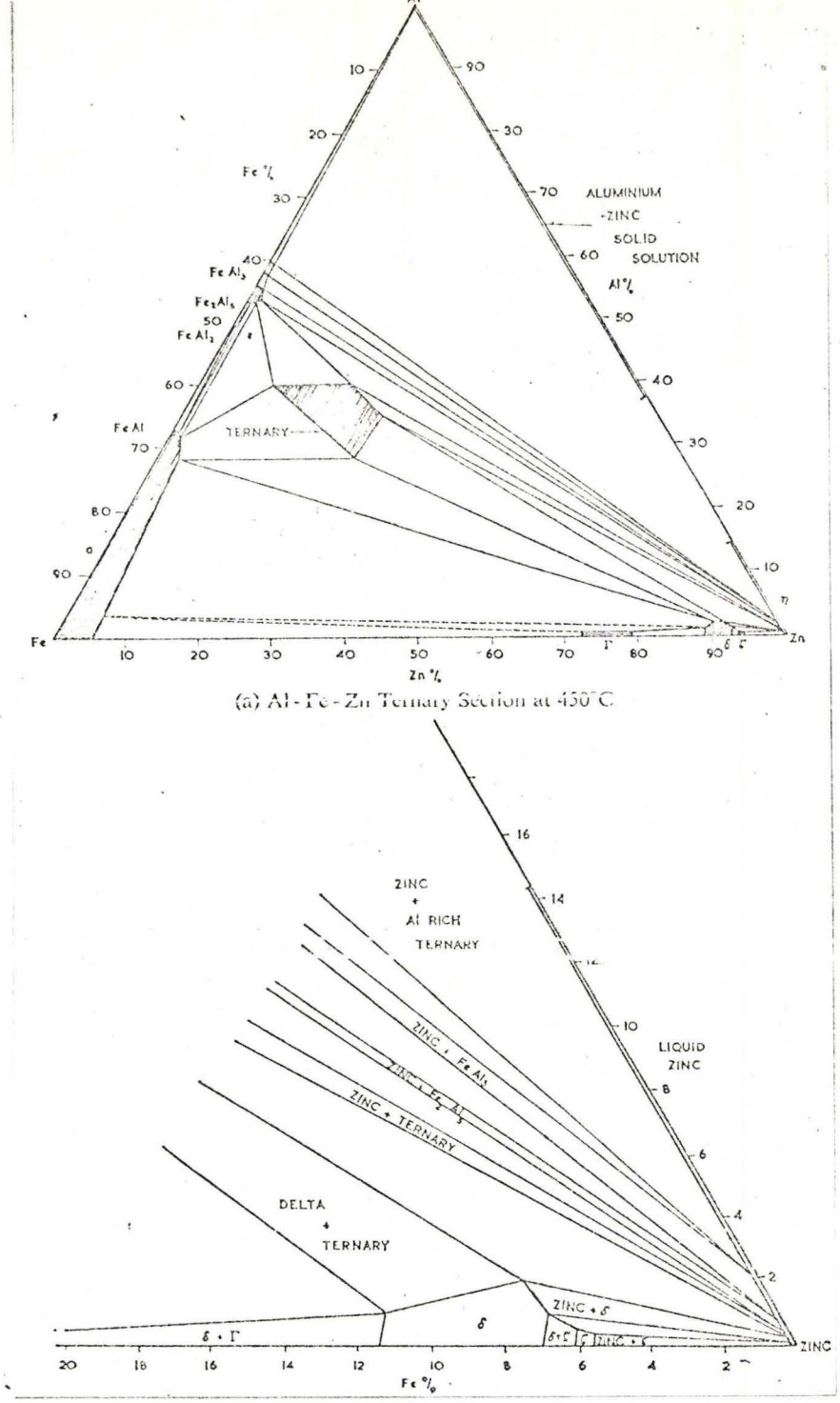

(a) Al-Fe-Zn Ternary Section at 450°C

Figure 7. The tentative Fe-Zn-Al ternary isotherm at 450°C, after Cameron and Ormay[29].

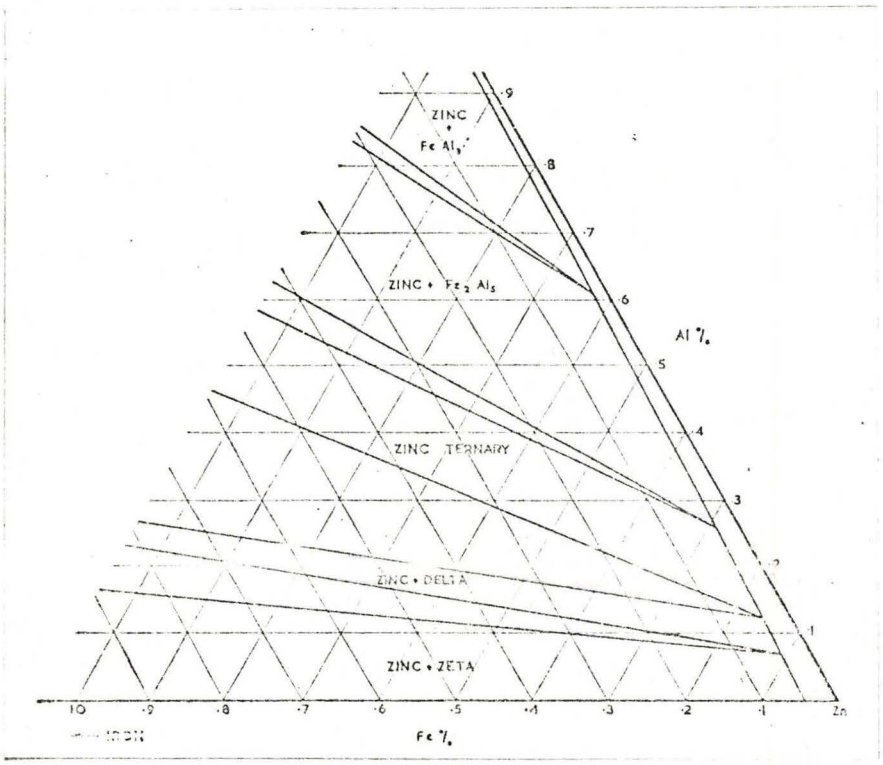

Figure 8. Magnified zinc corner of the tentative Fe-Zn-Al ternary isotherm at 450°C after Cameron and Ormay[29].

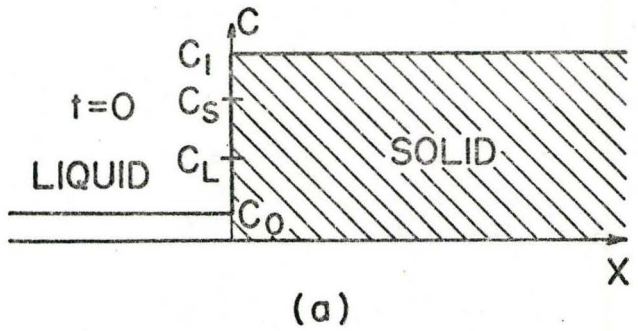

(a)

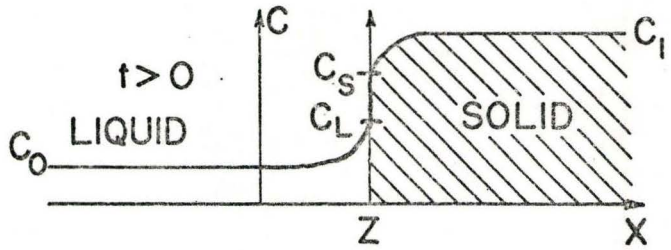

(b)

Figure 9. Boundary conditions for diffusion in a liquid with moving boundaries. (a) initial conditions, (b) diffusion in a static liquid.

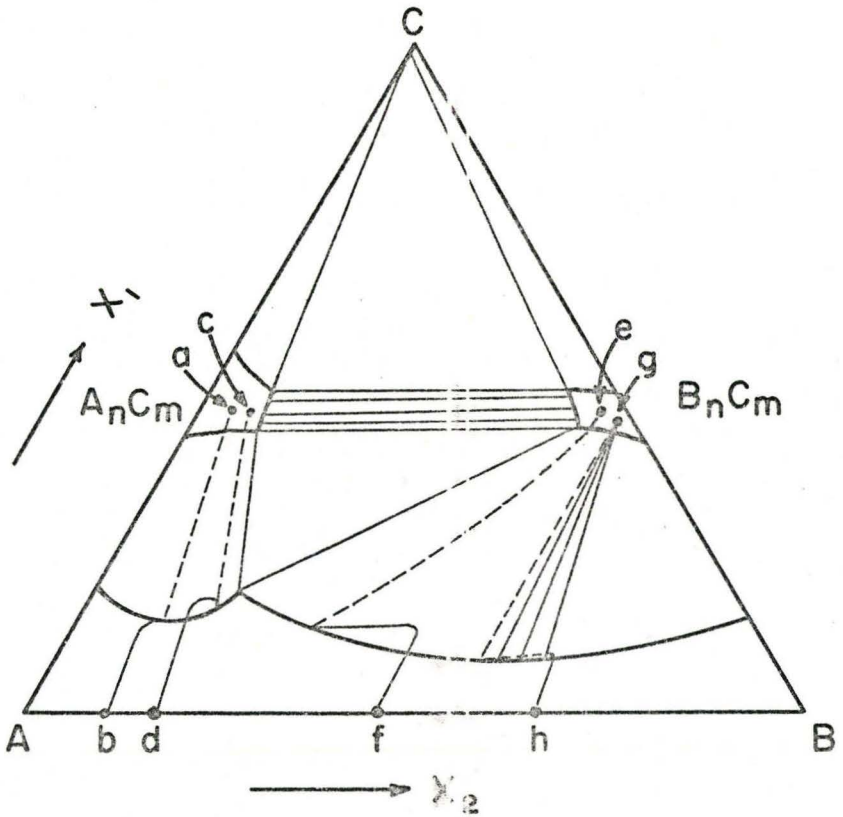

Figure 10. Schematic diffusion paths on the isotherm.

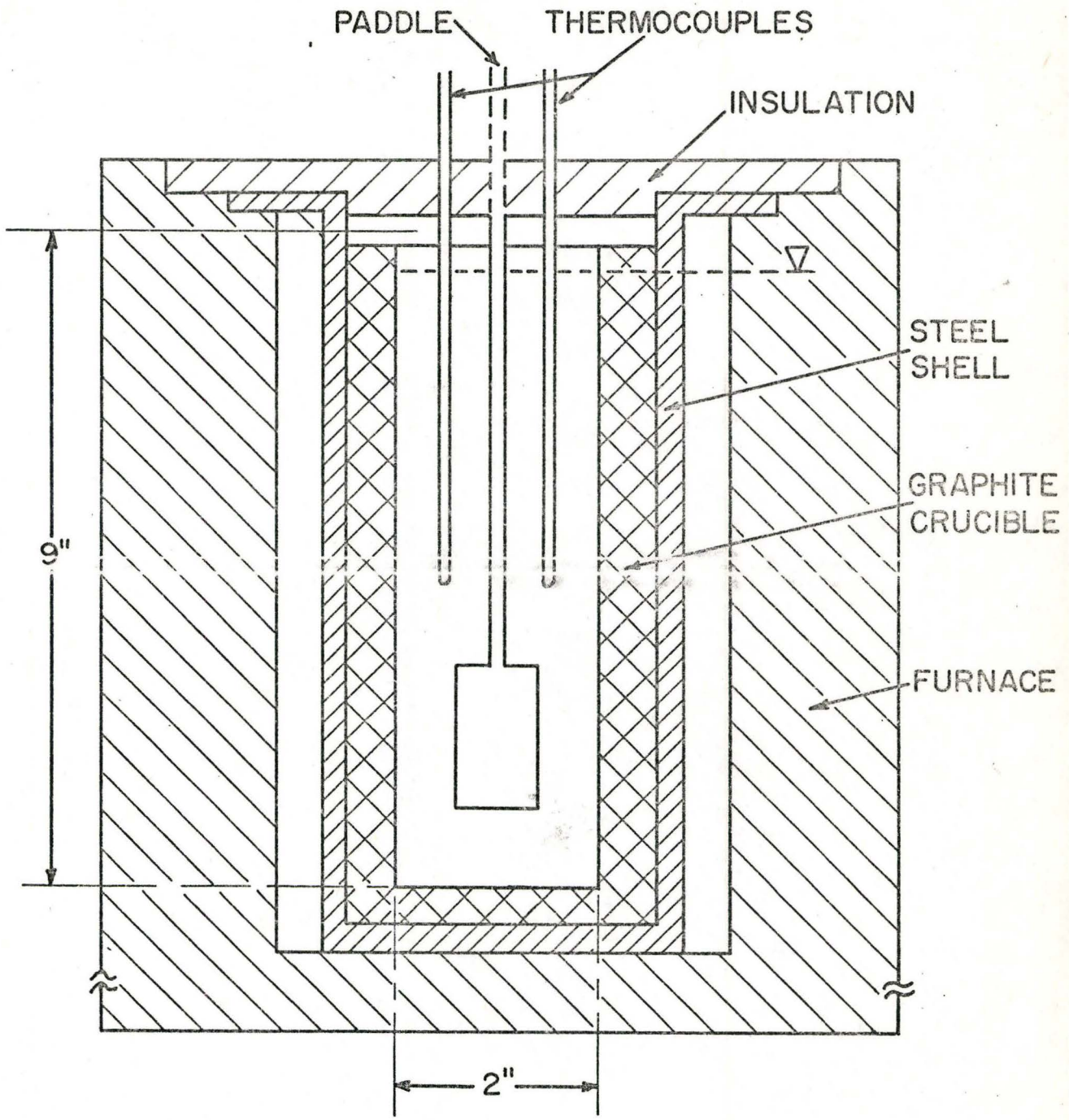

Figure 11. Cross-section of the apparatus used for liquidus determinations.

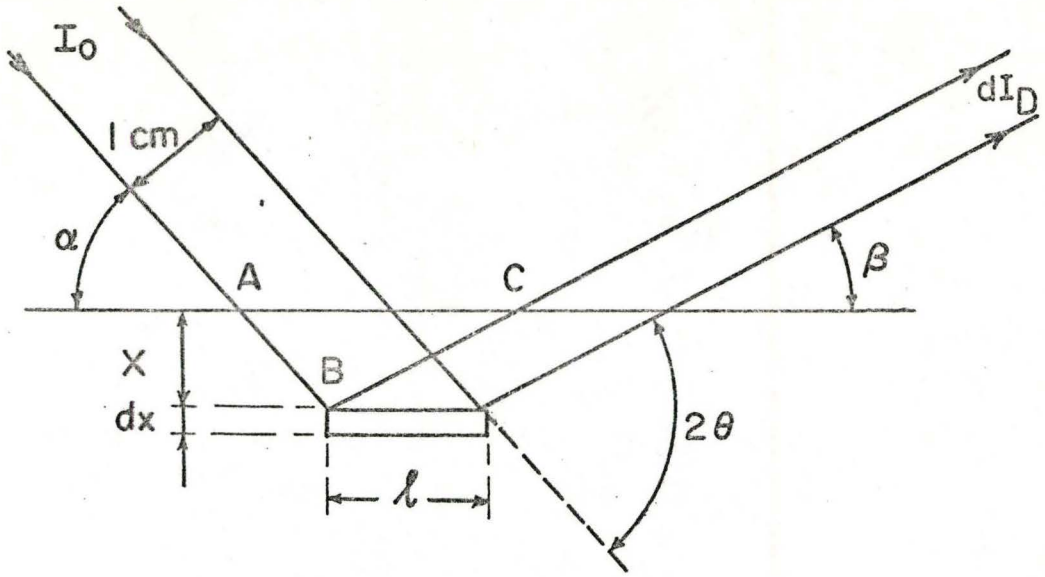

Figure 12. X-ray diffraction by a flat specimen.

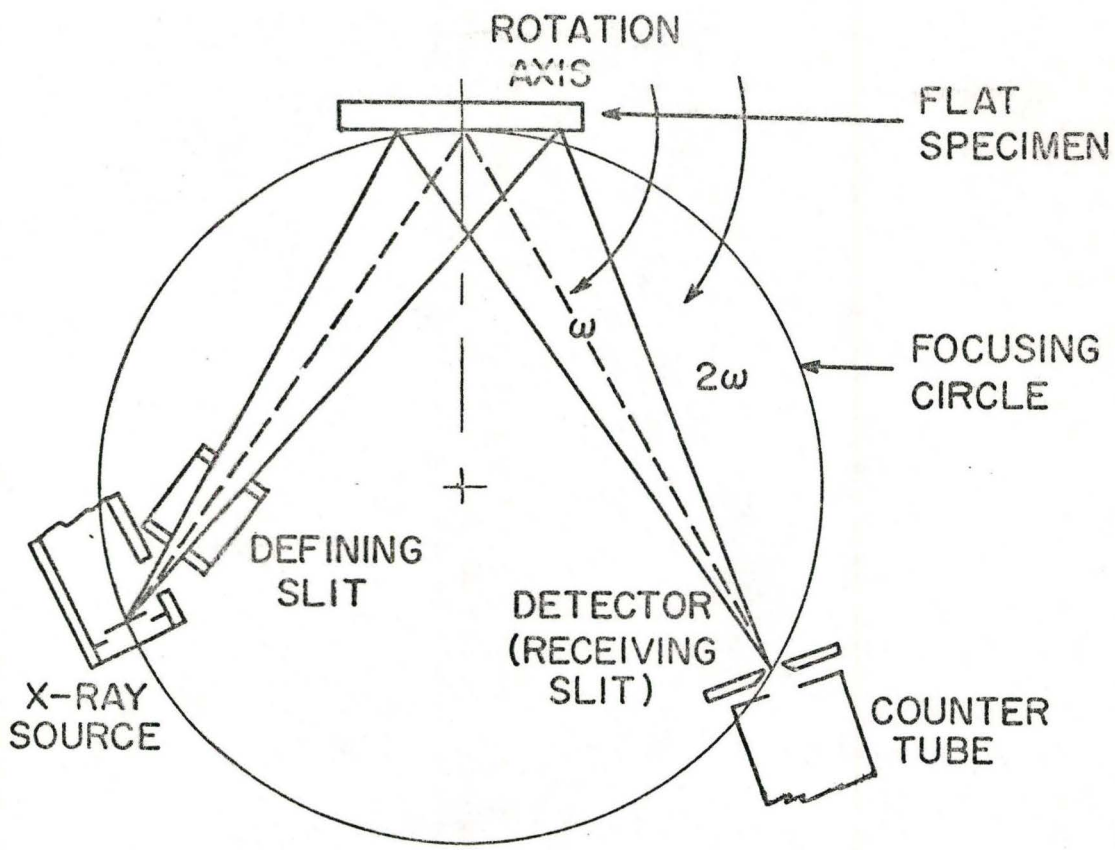

Figure 13. Diffractometer using a flat specimen with the Bragg-Brentano para-focusing geometry.

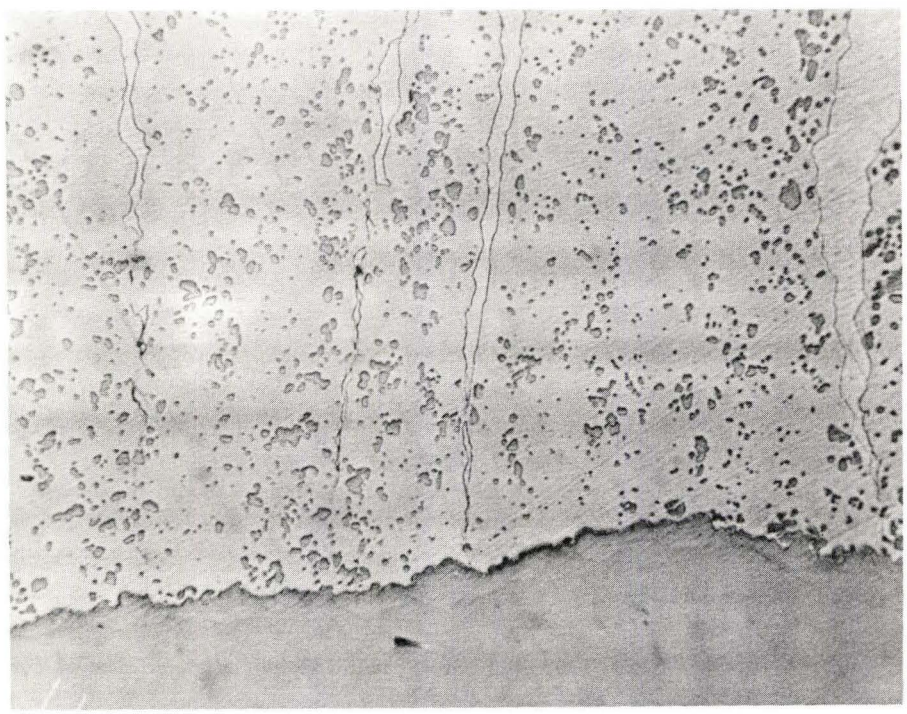

Figure 14. The microstructure of FeAl-Zn equilibrium specimen (230X).

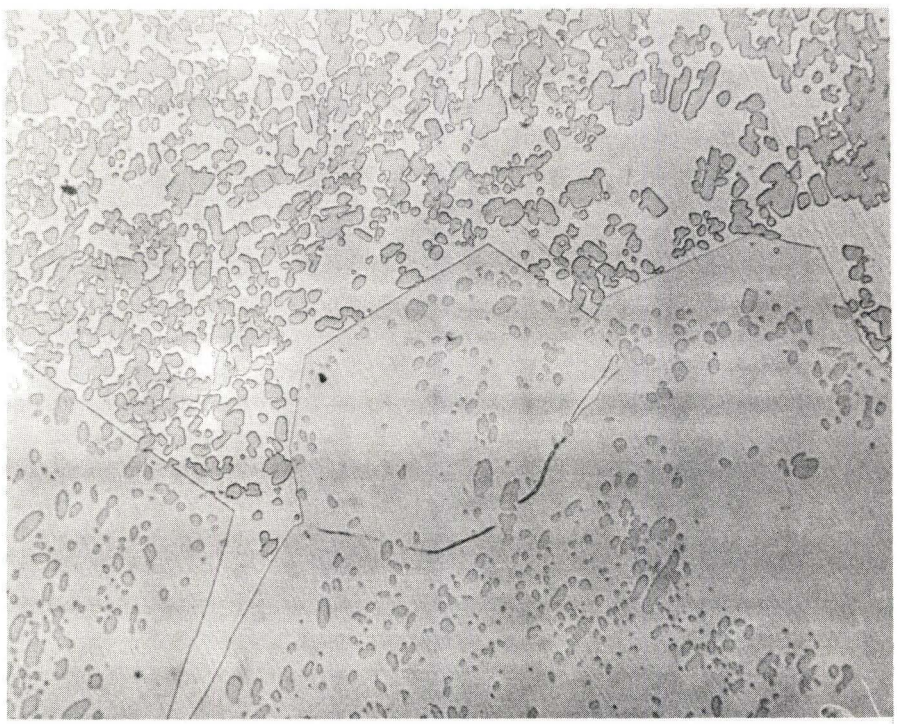

Figure 15. The microstructure of FeAl-Zn(Al) equilibrium specimen (230X).

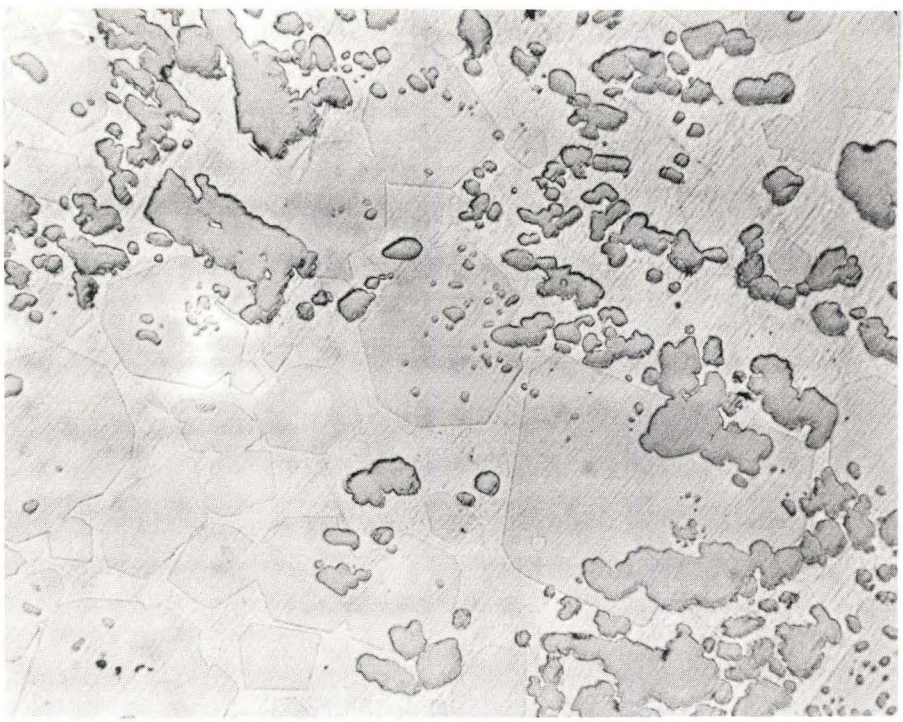

Figure 16. The microstructure of $FeAl_2$-Zn equilibrium specimen (230X).

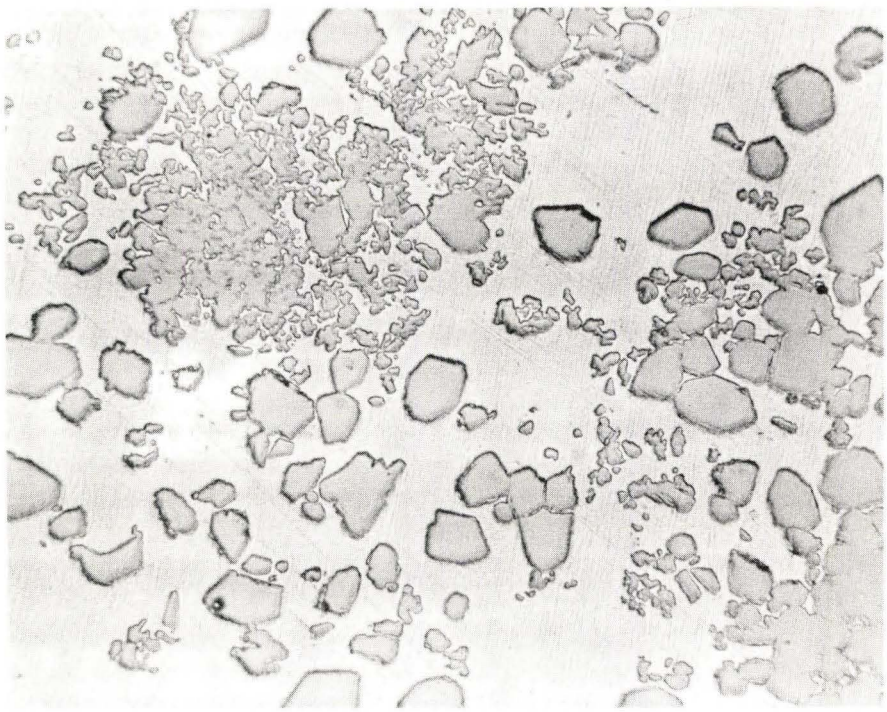

Figure 17. The microstructure of $FeAl_2$-Zn(Al) equilibrium specimen (230X).

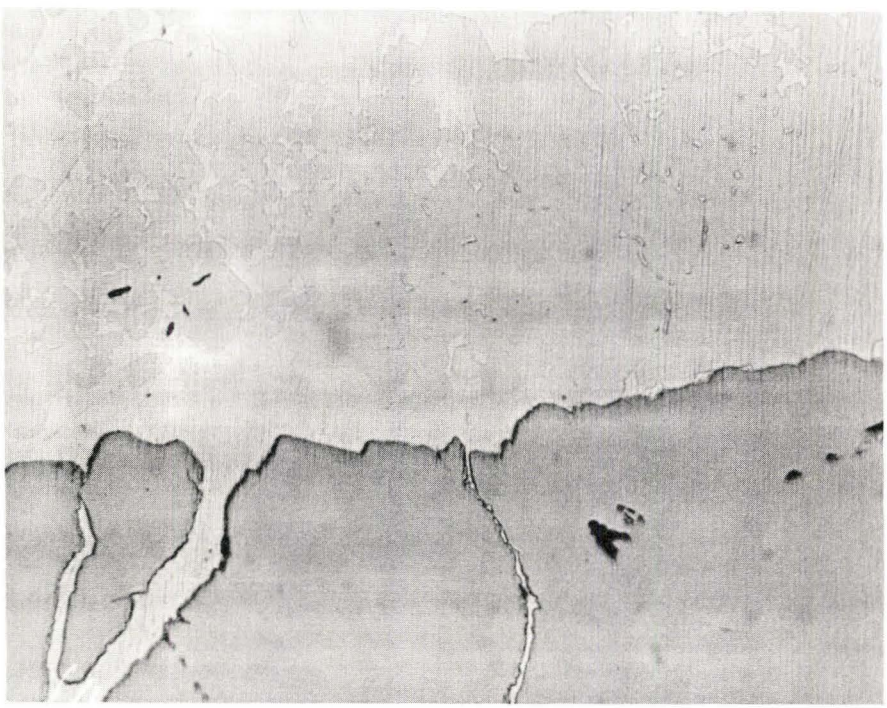

Figure 18. The microstructure of Fe_2Al_5-Zn equilibrium specimen (230X).

Figure 19. The microstructure of Fe_2Al_5-Zn(Al) equilibrium specimen (230X).

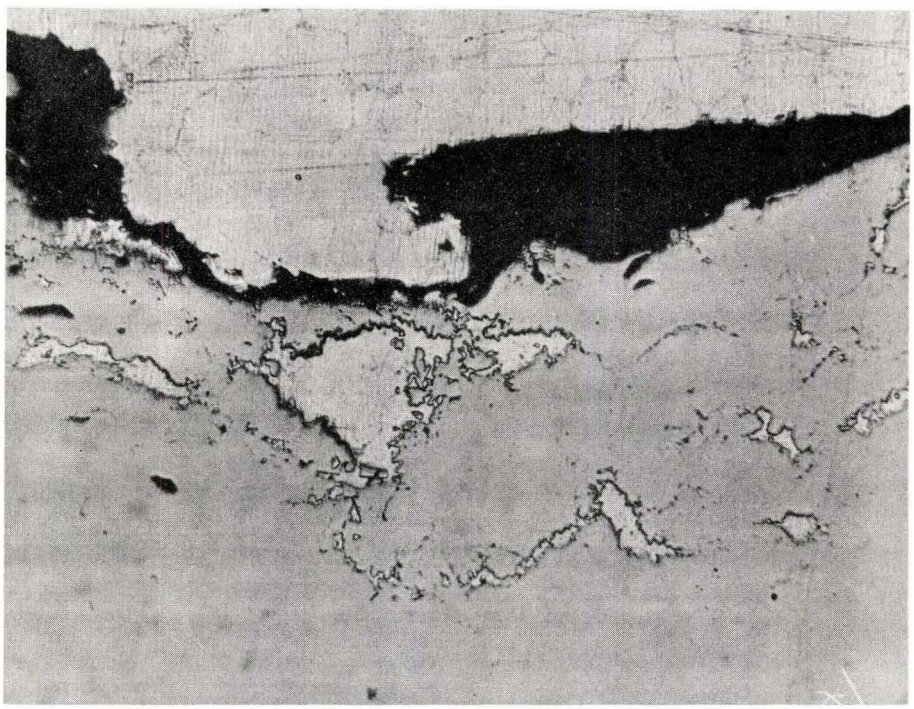

Figure 20. The microstructure of $FeAl_3$-Zn(Al) equilibrium specimen (230X).

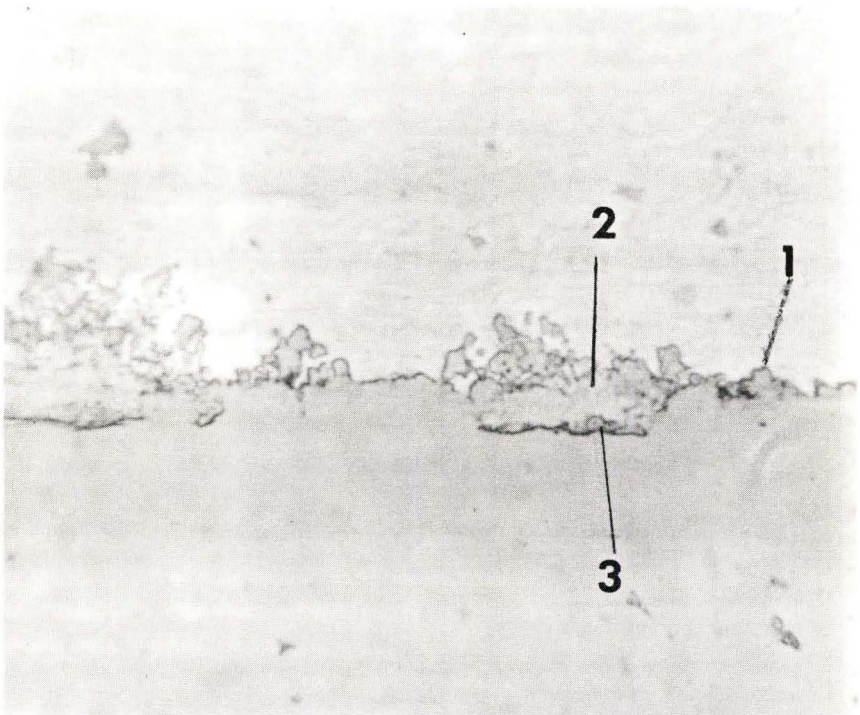

Figure 21. Microstructure developed on iron galvanized zinc bath containing 0.15 wt.% Al; immersion time 1 min; agitated (1140X).

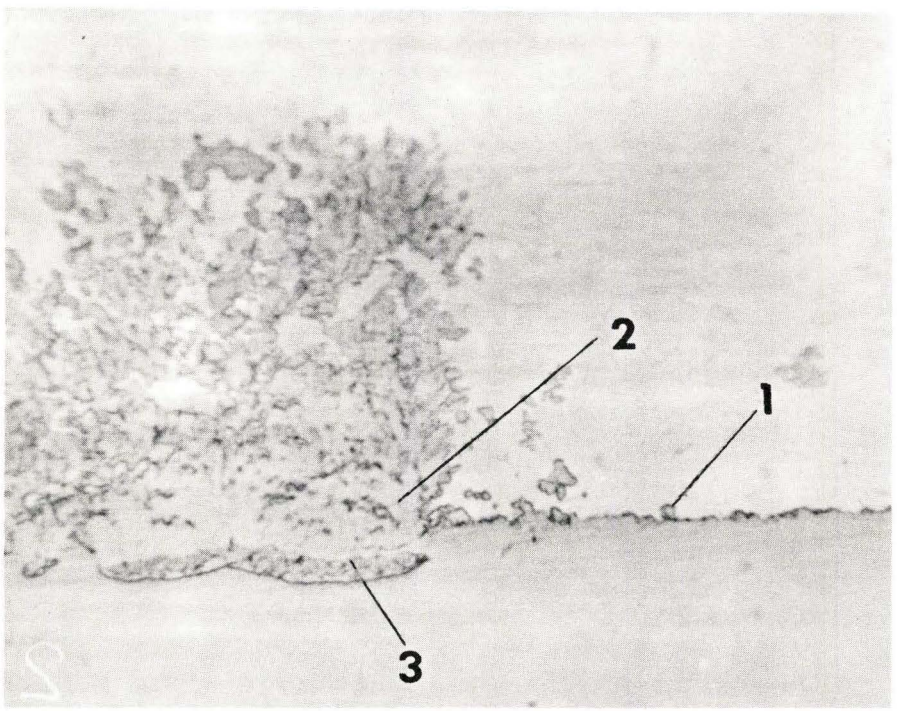

Figure 22. Microstructure developed on iron galvanized in zinc bath containing 0.15 wt.% Al; immersion time 3 min; agitated (1140X).

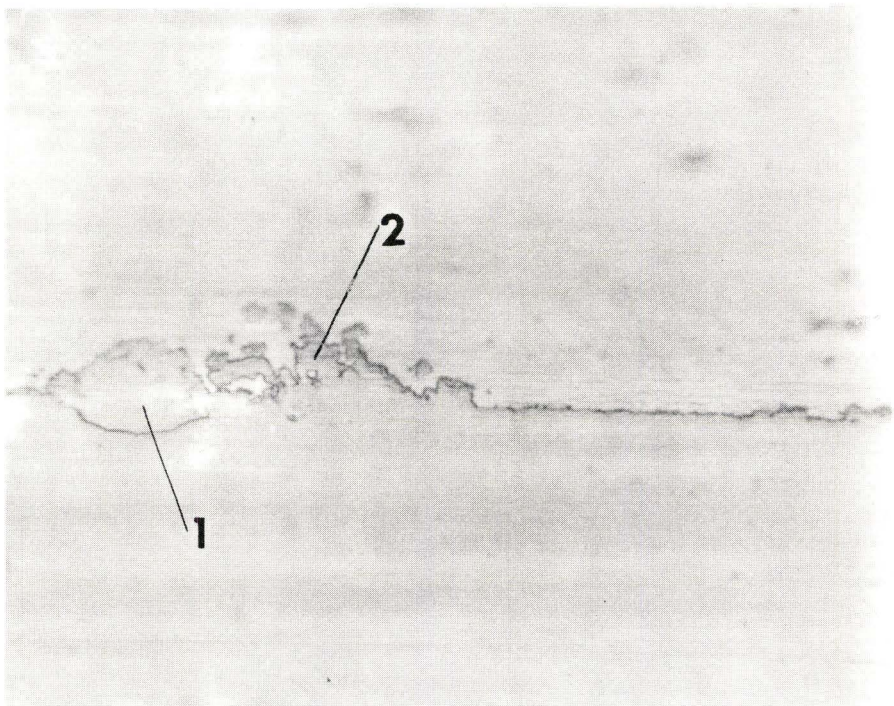

Figure 23. Microstructure developed on iron galvanized in zinc bath containing 0.22 wt.% Al; immersion time 3 min; no agitation (1140X).

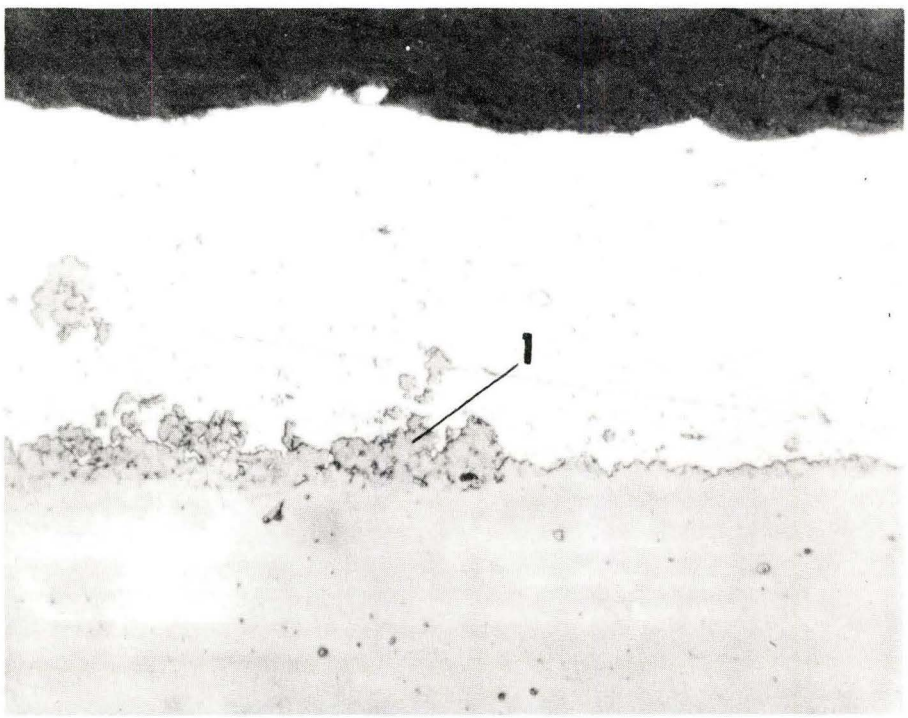

Figure 24. Appearence of the iron-zinc interface unattacked and with growing blue-grey phase. Bath containing 0.32% Al; immersion time 3 min; agitated (1140X).

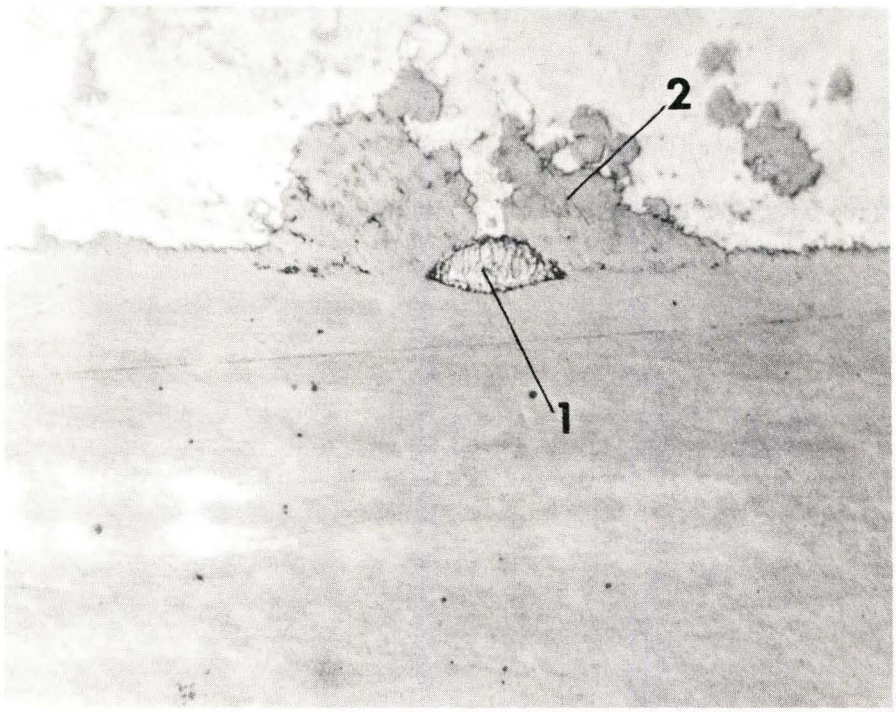

Figure 25. Microstructure developed on iron in zinc bath containing 0.22 wt.% Al; immersion time 10 min; agitated (1140X).

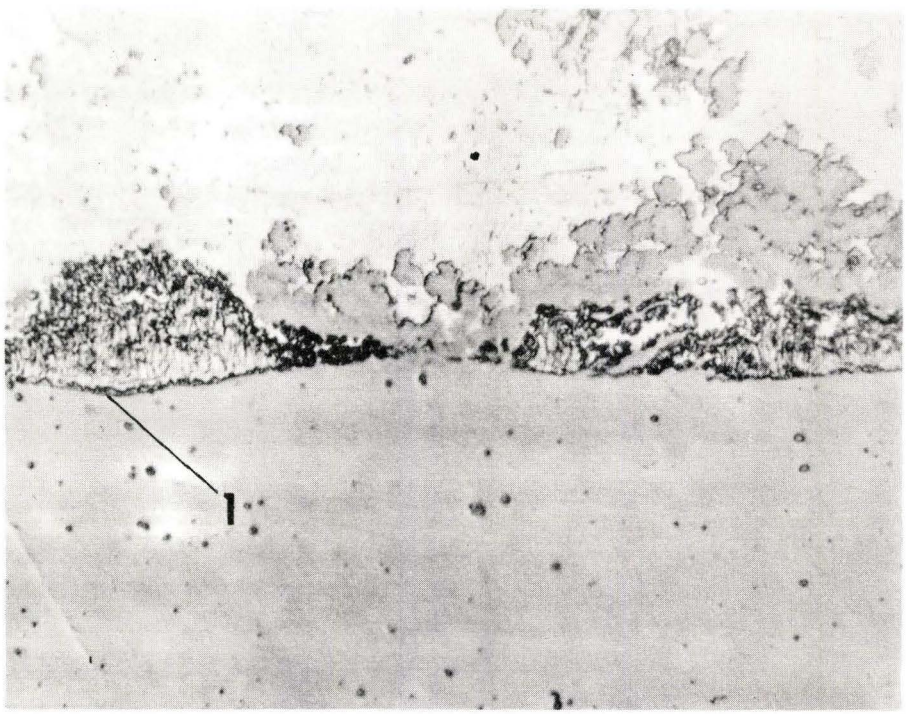

Figure 26. Microstructure developed on iron galvanized in zinc bath containing 0.22 wt.% Al; immersion time 15 minutes; agitated (1140X).

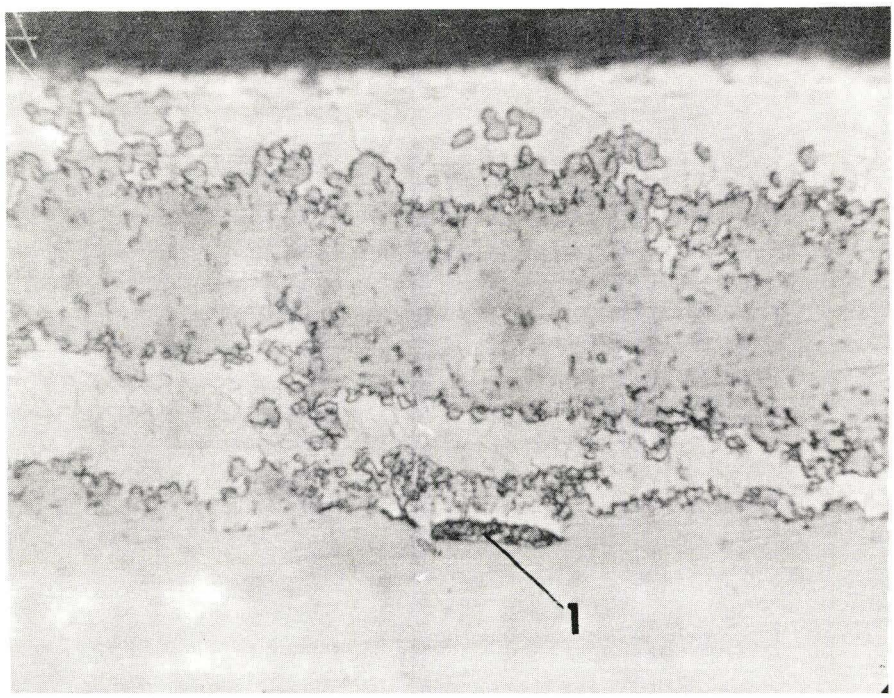

Figure 27. Microstructure developed on iron galvanized in zinc bath containing 0.32 wt.% Al; immersion time 10 min; no agitation (1140X).

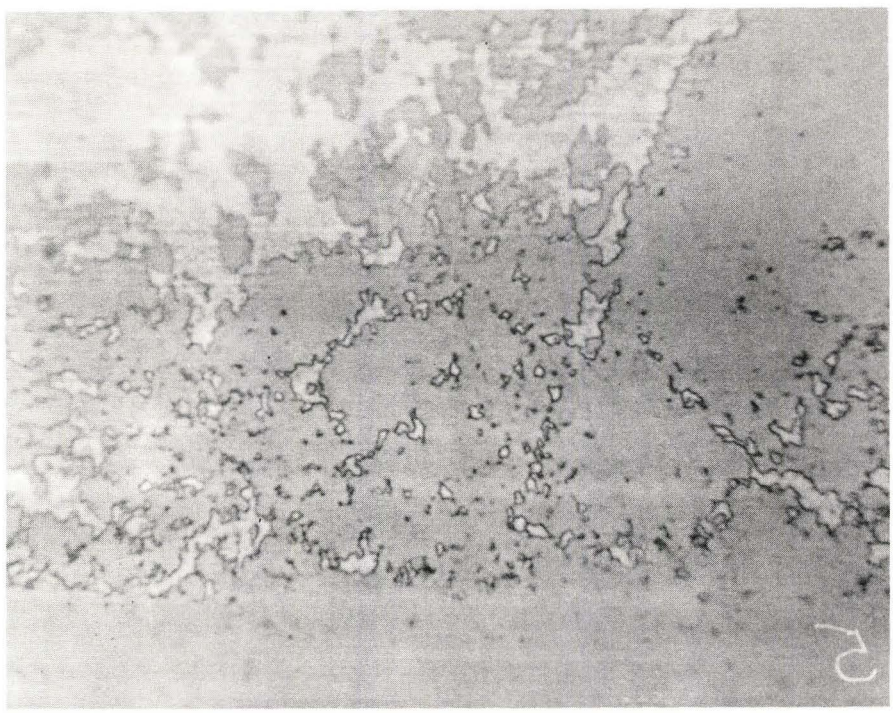

Figure 28. Microstructure developed on iron in zinc bath containing 1.10 wt.% Al; immersion time 10 min; no agitation (1140X).

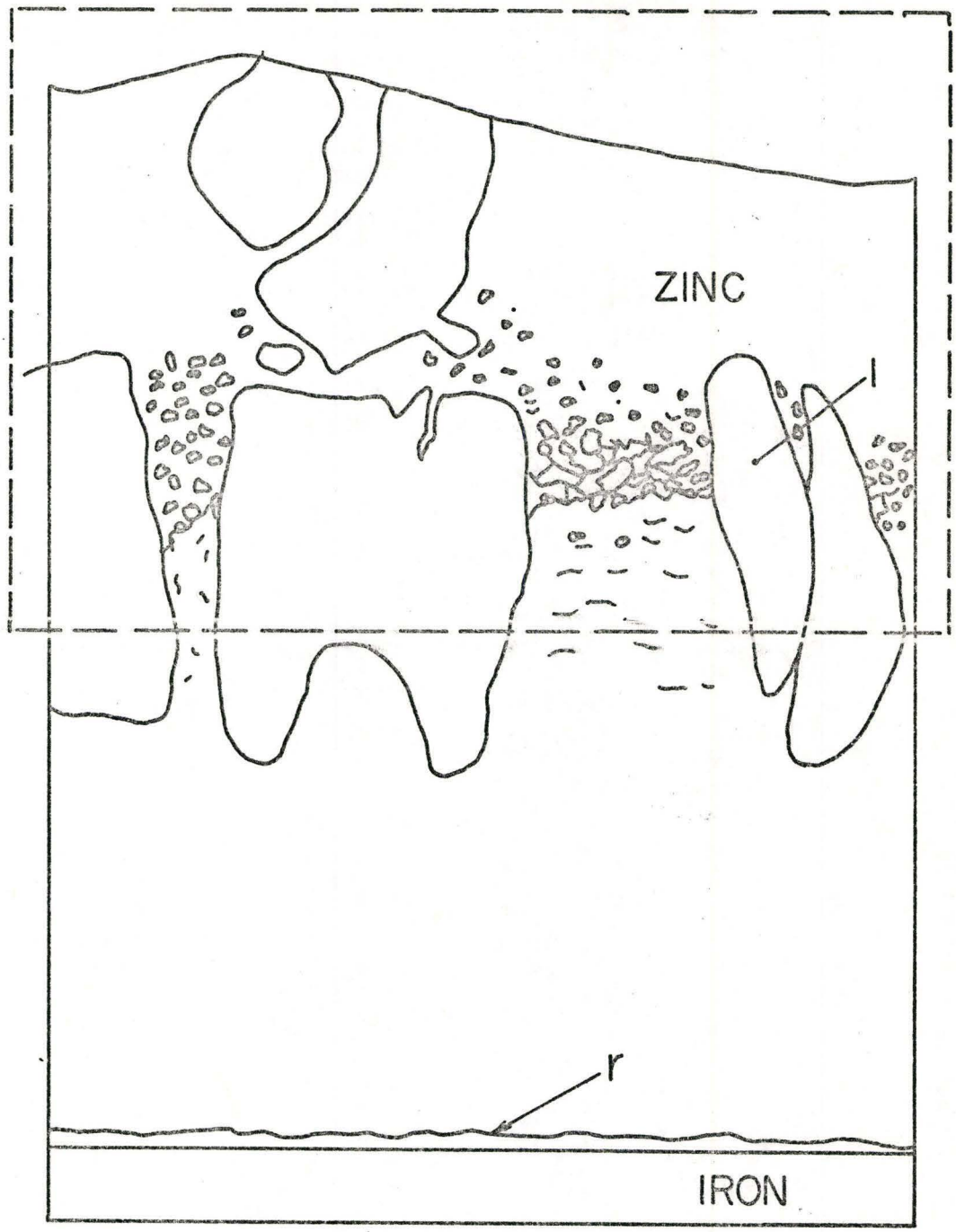

Figure 29. Schematic microstructure developed on iron galvanized in zinc bath containing 0.22 wt.% Al; immersion time 30 min; agitated (230X).

Figure 30. Microstructure developed on iron galvanized in zinc bath containing 0.22 wt.% Al; immersion time 30 min; agitated (230X).

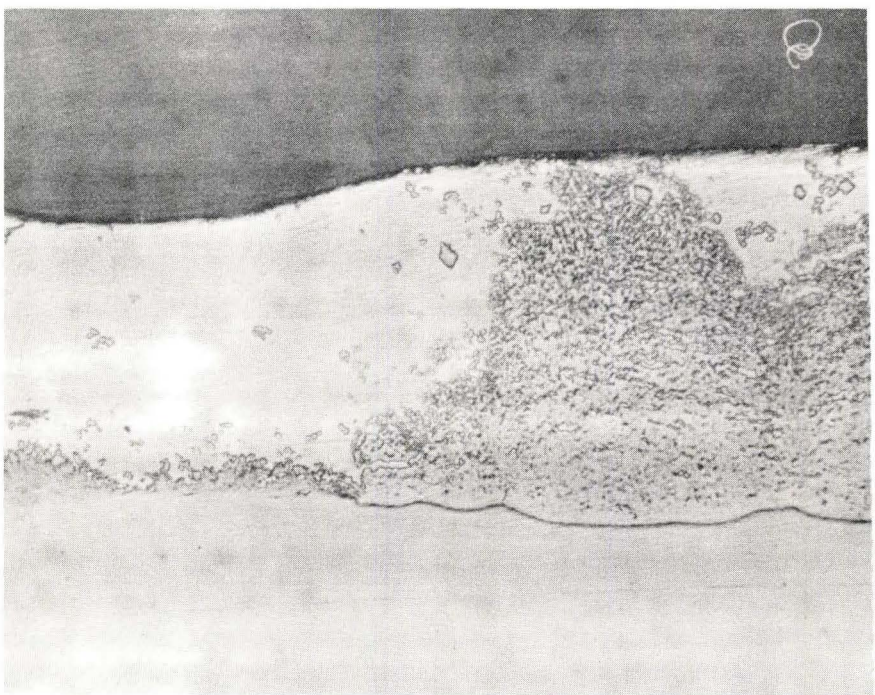

Figure 31. Microstructure developed on iron galvanized in zinc bath containing 0.32 wt.% Al; immersion time 30 min; agitated (230X).

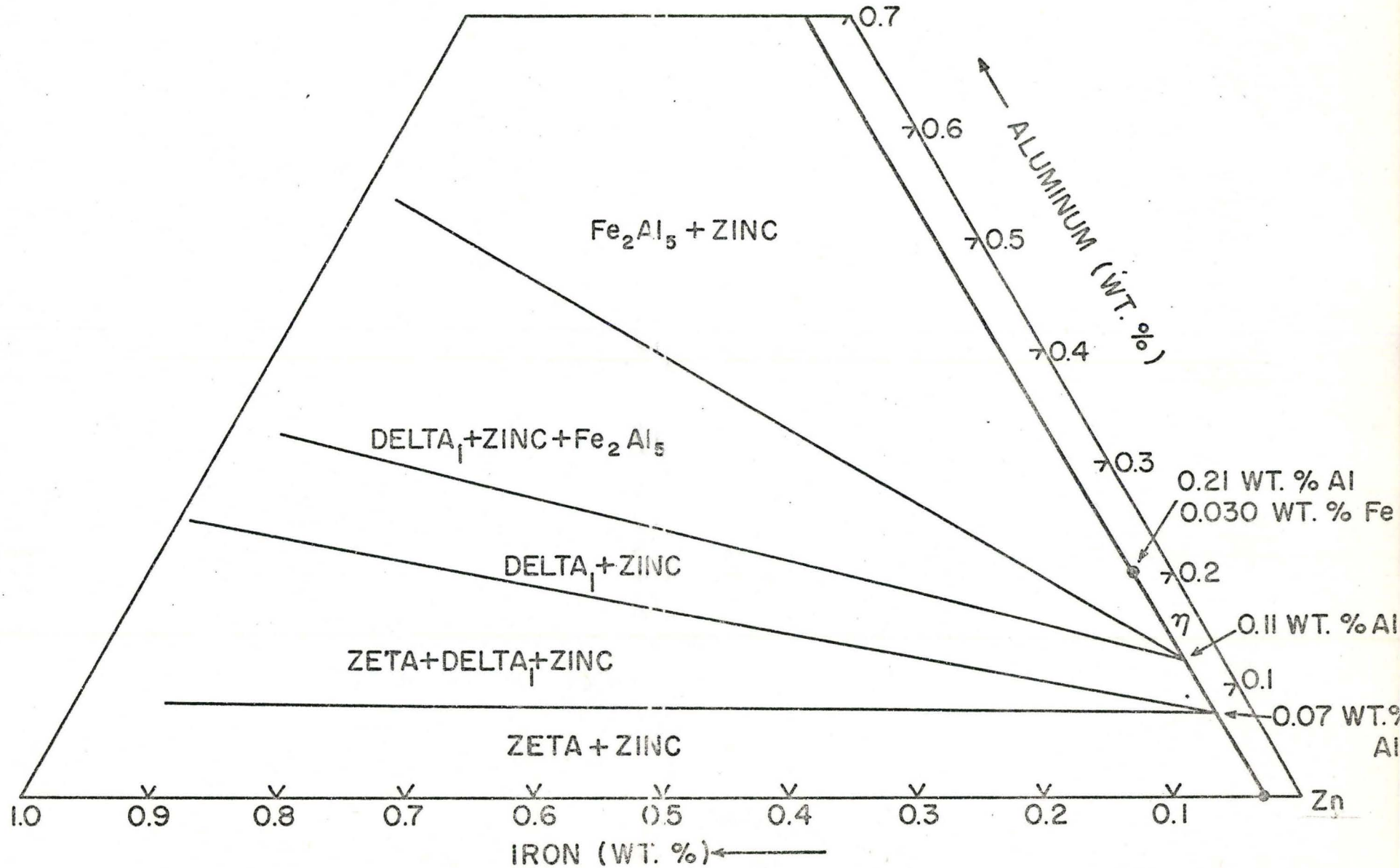

Figure 32. Modified zinc corner of the tentative Fe-Zn-Al isotherm at 450°C.

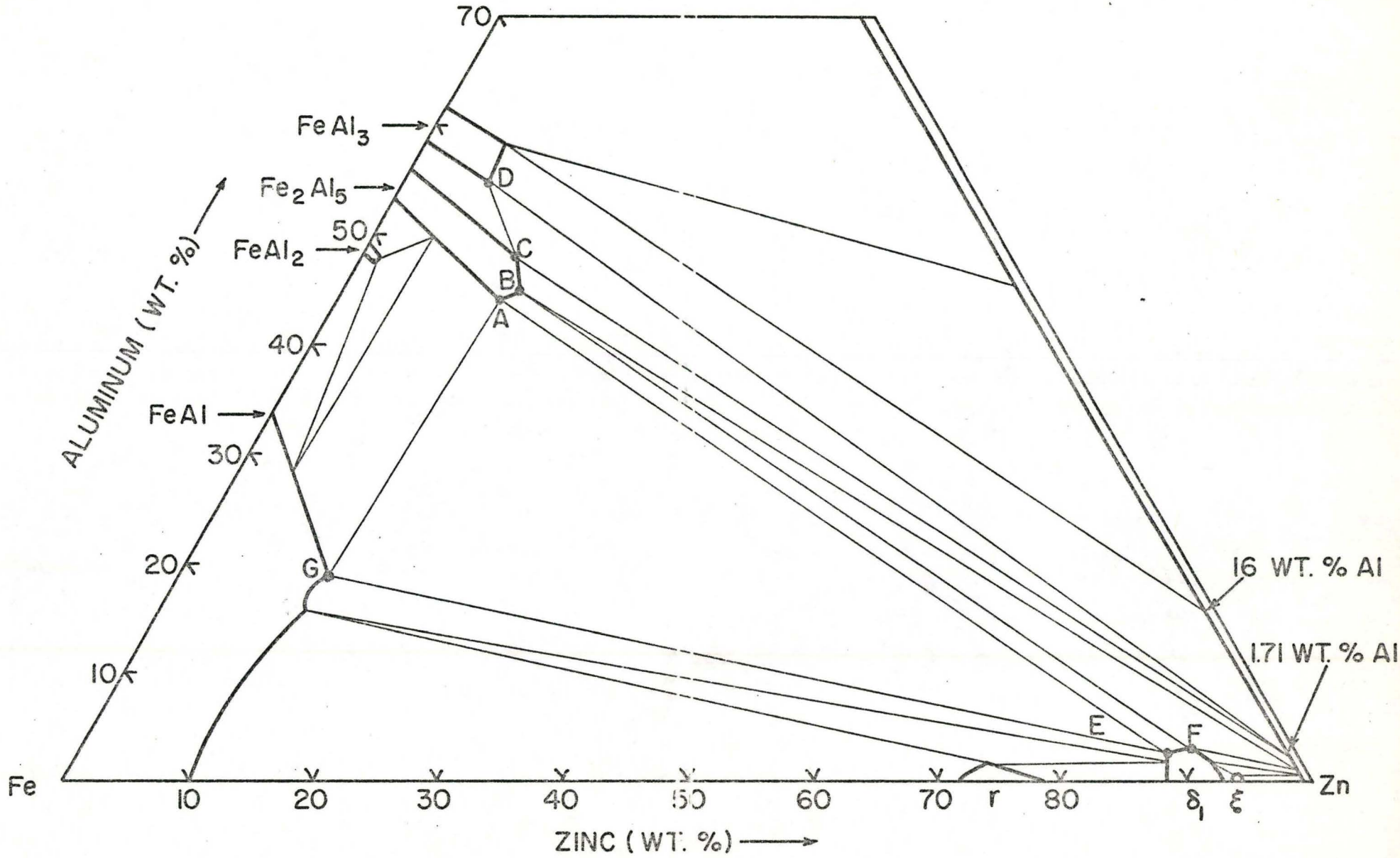

Figure 33. Summary of the constitution diagram of the Fe-Zn-Al system at 450°C.

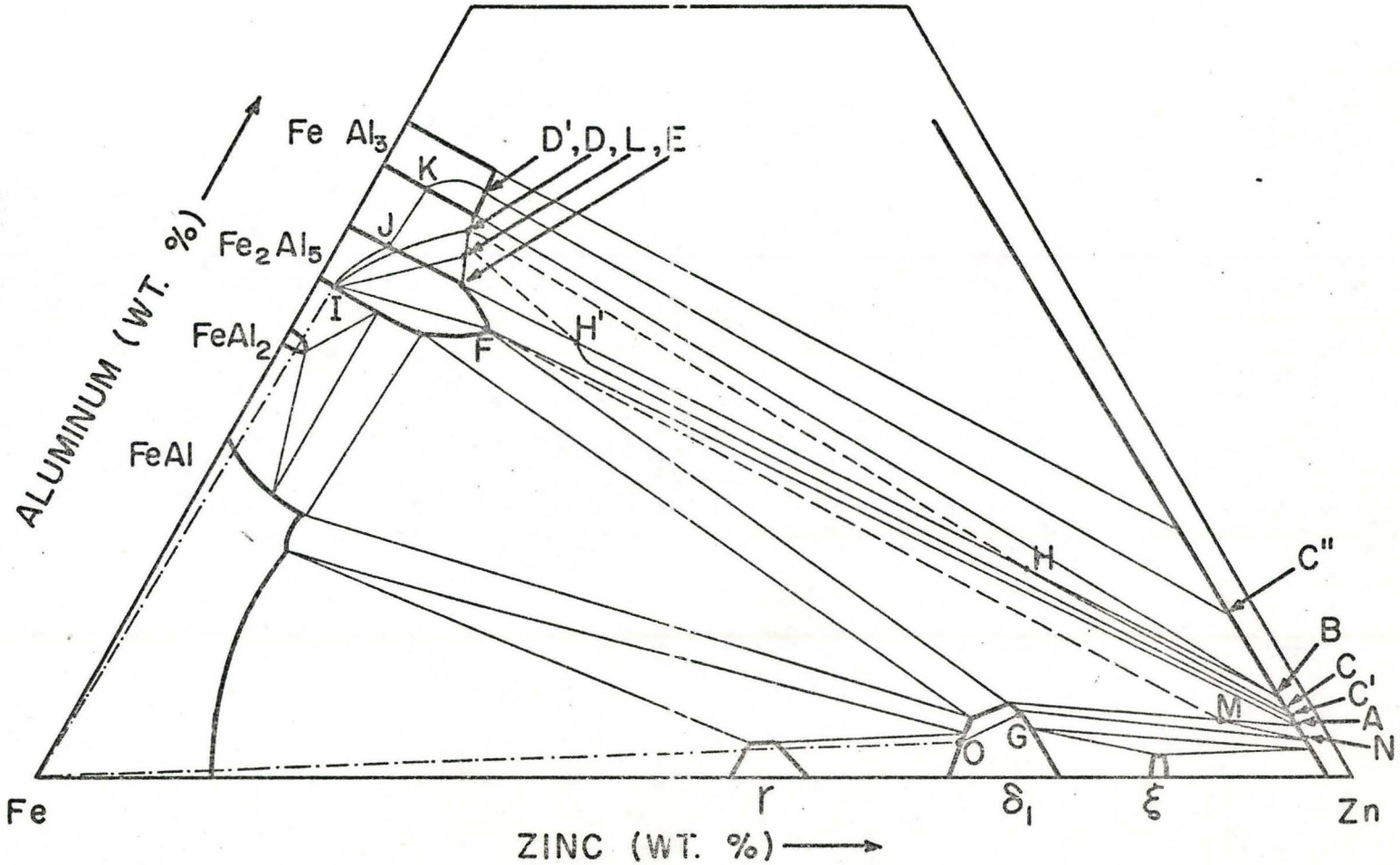

Figure 34. Schematic 450°C isotherm of the Fe-Zn-Al system with proposed diffusion paths.